UNIVERSITY OF CANTERBURY

DOCTORAL THESIS

Interactions Between Changing Weather Patterns and the Antarctic Cryosphere in the Ross Sea Region

---

Author:
Ethan R. DALE

Supervisors:
Adrian J. MCDONALD
Wolfgang RACK
Marwan KATURJI

A thesis submitted in partial fulfilment of the requirements for the degree of Doctor of Philosophy in Physics

in the

Environmental Research Group
Department of Physical and Chemical Sciences

2020

"We're about to have a bad spell of wether."

Anonymous

UNIVERSITY OF CANTERBURY

Abstract

College of Science

Department of Physical and Chemical Sciences

Doctor of Philosophy in Physics

Interactions Between Changing Weather Patterns and the Antarctic Cryosphere in the Ross Sea Region

by Ethan R. DALE

In this thesis the sensitivity of the cryosphere to changing weather patterns in the Ross Sea is investigated. The focus is on the production and persistence of sea ice and precipitation events over the Ross Ice Shelf (RIS). Changes are expected as a result of climate variability, and the change in the occurrence of storms and other severe weather patterns in Antarctica and in the Ross Sea.

The influence of strong wind events on the sea ice concentration within the Ross Sea Polynya (RSP) is studied. Sea ice concentration within the RSP was observed to show a rapid decrease in response to strong wind events. Following a strong wind event, the RSP was found to remain open for an extended period of time, persisting beyond the end of the strong wind event. Sea ice drift within the Ross Sea was observed to be influenced by strong wind events with cyclonic drift anomalies being observed during periods of strong winds. A comparison of ERA-Interim reanalysis wind speeds and observed Automatic Weather Station (AWS) wind speeds east of Ross Island revealed that, despite strong correlations between the two data sets, ERA-Interim considerably underestimates wind speeds.

Data from a Controlled Meteorological balloon flight within the atmospheric boundary layer over the Ross Sea in November 2017 is presented. The flight lasted 70 hours and passed over both the Terra Nova Bay and Ross Sea polynyas whilst making 31 vertical soundings. Balloon observations of temperature, humidity, and wind velocity were compared to co-located predictions made by the

Antarctic Mesoscale Prediction System (AMPS); the two data sets were generally found to agree. The wind direction predictions made by AMPS were found to be least accurate in the vicinity of complex topography and during periods of low wind speed. The upward heat and moisture fluxes from the RSP were investigated. Lagrangian and Eulerian derivatives of potential temperature and water mixing ratios were calculated using Lagrangian back trajectories within the AMPS field. This allow sources and sinks of both heat and moisture to be identified. While diabatic heating was observed over the RSP during this period, the same area was not observed to provide a net flux of moisture.

The various circulation patterns that influence the rate of precipitation over the RIS are studied. The moisture origins for a site over the RIS were investigated using Lagrangian back trajectories. An ensemble of over 50 000 back trajectories were calculated using ERA-Interim wind field from 1979 until 2016. The spatial distributions of back trajectory origin points were compared for periods of precipitation and for periods without precipitation. During periods of precipitation, higher origin point densities were observed in the Ross and Amundsen Seas, and lower densities were observed in the Bellingshausen and Weddell Seas. The pathways taken by trajectories with similar origin locations to reach the RIS often show large variations. This was shown to have a dramatic effect on the humidity of the air parcel at arrival; trajectories that travel over mountainous regions were often very dry once they arrived over the RIS.

This thesis, therefore, has a strong focus on processes associated with the RSP. It is shown that strong winds over this region result in the advection of sea ice exposing the warm ocean below. This causes freezing of the ocean surface resulting in sea ice production in this region. The influence of this polynya on the local atmosphere was investigated. AMPS potential temperature fields indicate this region of open water provided a heat flux to the atmosphere over a 20 000 km^2 area during the period of balloon observations. A moisture flux was not observed from AMPS water mixing ratio field for the same period. Sea ice isolates the atmosphere from the ocean preventing evaporation of moisture. Moisture transport to the RIS was found to be limited by sea ice, as moist air was generally found to originate from north of the ice pack.

Deputy Vice-Chancellor's Office
Postgraduate Research Office

UNIVERSITY OF CANTERBURY
Te Whare Wānanga o Waitaha
CHRISTCHURCH NEW ZEALAND

Co-Authorship Form

This form is to accompany the submission of any thesis that contains research reported in co-authored work that has been published, accepted for publication, or submitted for publication. A copy of this form should be included for each co-authored work that is included in the thesis. Completed forms should be included at the front (after the thesis abstract) of each copy of the thesis submitted for examination and library deposit.

Please indicate the chapter/section/pages of this thesis that are extracted from co-authored work and provide details of the publication or submission from the extract comes:

Chapter 4: ***Atmospheric Forcing of Sea Ice Anomalies in the Ross Sea Polynya Region****, Published in The Cryosphere, 2017 (Dale et al., 2017).*

Please detail the nature and extent (%) of contribution by the candidate:

Ethan Dale was the lead author of this paper; contribution 80%.

Certification by Co-authors:

If there is more than one co-author then a single co-author can sign on behalf of all

The undersigned certifies that:

- The above statement correctly reflects the nature and extent of the PhD candidate's contribution to this co-authored work
- In cases where the candidate was the lead author of the co-authored work he or she wrote the text

Name:	Signature:	Date:
Adrian McDonald		1/5/2019

Deputy Vice-Chancellor's Office
Postgraduate Research Office

UNIVERSITY OF CANTERBURY
Te Whare Wānanga o Waitaha
CHRISTCHURCH NEW ZEALAND

Co-Authorship Form

This form is to accompany the submission of any thesis that contains research reported in co-authored work that has been published, accepted for publication, or submitted for publication. A copy of this form should be included for each co-authored work that is included in the thesis. Completed forms should be included at the front (after the thesis abstract) of each copy of the thesis submitted for examination and library deposit.

Please indicate the chapter/section/pages of this thesis that are extracted from co-authored work and provide details of the publication or submission from the extract comes:

Chapter 5: ***Evaluating Antarctic Mesoscale Prediction System (AMPS) Representation of the Ross Sea Polynya Using Controlled Metrological (CMET) Balloon Observations****, Submitted to: The Journal of Geophysical Review - Atmospheres, 2019 (In Review).*

Please detail the nature and extent (%) of contribution by the candidate:

Ethan Dale was the lead author of this paper; contribution 70%.

Certification by Co-authors:

If there is more than one co-author then a single co-author can sign on behalf of all

The undersigned certifies that:

- The above statement correctly reflects the nature and extent of the PhD candidate's contribution to this co-authored work
- In cases where the candidate was the lead author of the co-authored work he or she wrote the text

Name:	Signature:	Date:
Adrian McDonald		11/5/2019

Acknowledgements

Firstly, I would like to thank the fantastic supervisory team I have had to support and inspire me throughout the last four years: Adrian McDonald and Wolfgang Rack. Without your seemingly infinite supply of patience and wisdom, this document would never have been possible. I would also like to thank Marwan Katurji for providing guidance and insight for chapter 5 as well as offering me the fantastic opportunity to take part in the CMET field campaign.

During this thesis I have had the pleasure of spending time in Antarctica with many great people including: Daisuke Seto, Michelle Ryan, Graeme Plank, Orlon Petterson, Marcus Arnold, and Raki Ryan. The memories we shared together will last me a lifetime. I would like to thank the helpful staff of both Antarctica New Zealand and PNRA, particularly those at Scott Base and Mario Zucchelli Station, both of which hosted me during the field work required for this thesis.

I would like to thank the many people who have been part of the atmospheric physics group and I have had the pleasure of sharing a work space with throughout my PhD: Alex Schuddeboom, Ben Jolly, Peter Kuma, Sean Hartery, Helena Sodergren, Laura Revell, Simon Parsons, Jack Coggins, Madeline Smith, Fraser Dennison, Ryan Ridden-Harper, Leon Fredrich, Mathew Jones, Andy Ichohja, Dominic Jones, Dongqi Lin, Cameron McErlich, and Luke Cairns. In particular I would like to acknowledge Alex Schuddeboom, with whom I shared a flat and many insightful conversations (and some not so insightful) as well as for downloading the ERA-Interim data set used throughout this thesis. I further thank the many people within the physics department that I have had the pleasure of sharing time with over the last 4 years, in particular: Amber Malpas, Dylan Paterson, Brendan Coleman, and Christoph Bergmann.

I am appreciative of the support provided by my many friends outside of the university. While there are too many to name, I would like to acknowledge the support provided by: Wills Dobson, Conor Beaton, and Ben Allan, who have always given me a reason to get out of Christchurch.

I would like to thank my family for the financial, logistical, and emotional support they have provided me throughout my academic career. I wish to thank my mother for always lending an ear during the stressful times and to my father for taking me on adventures during the less stressful times.

This thesis was funded by a Departmental Scholarship awarded by the Department of Physical and Chemical Sciences and a postgraduate scholarship awarded

by Antarctica New Zealand and funded by New Zealand Post. Without this funding I would not have been able to write this thesis and I am therefore very grateful to these organisations.

Finally I would like to thank my fantastic girlfriend Rebecca, for providing me with encouragement, smiles, and laughs over these last few months, and for putting up with my many late nights and other absences. I honestly don't know how I would have finished this thesis without you. Further I would like to thank you for taking the time to read the majority of this document; the feedback you provided greatly improved the quality of this thesis.

Contents

List of Figures

List of Tables

List of Abbreviations

AABW Antarctic bottom Water

AMPS Antarctic Mesoscale Prediction System

ASL Amundsen Sea Low

ASMR-E Advanced Microwave Scanning Radiometer - Earth Observing System

AWS Automatic Weather Station

CCF Cross Correlation Function

CMET Controlled Meteorological

CMIP5 Coupled Model Intercomparison Project phase 5

IOD Indian Ocean Dipole

MSLP Mean Sea Level Pressure

NASA National Aeronautics and Space Administration

NSIDC National Snow and Ice Data Centre

RAS Ross Air Stream

RIS Ross Ice Shelf

RS Ross Sea

RSP Ross Sea Polynya

SAM Southern Annular Mode

SIA sea ice area

SIE sea ice extent

SIC sea ice concentration

SMB surface mass balance

SSM/I Special Sensor Microwave/Imager

SSM/IS Special Sensor Microwave/Imager Sounder

SMMR Scanning Multichannel Microwave Radiometer

SST Sea Surface Temperature

TAM Trans-Antarctic Mountains

TIR Thermal Infrared

WRF Weather Research and Forecasting

Chapter 1

Introduction

1.1 Motivation

Antarctica is Earth's most inhospitable continent. High elevations, extended periods of darkness, and a high albedo surface causes Antarctica to be the coldest place on Earth. Cold temperatures reduce the moisture-holding capacity of air, contributing to make Antarctica also the driest continent on the planet. During winter, surface cooling over the high altitude plateau leads to persistent katabatic flows that cause coastal regions of Antarctica to be amongst the windiest places on Earth, resulting in the formation of open water polynyas with high production rates of sea ice. Although the many extremes that occur in the Southern Continent are of scientific interest, Antarctica is one of the least understood and least observed regions on Earth (Jones et al. 2016). After the first coordinated efforts in the late 19th and early 20th centuries for Antarctic exploration, renewed interest in systematic measurements started in 1957 with the international geophysical year. During this year many permanent research bases were erected and many continuous observational records began (Liggett et al. 2015). More recently satellite-based observations have provided a wealth of continuous data sets, the majority of which began in 1979 (Jones et al. 2016).

Since the industrial revolution atmospheric carbon dioxide and other greenhouse gas levels have dramatically increased. The forcing on global temperatures due to these greenhouse gases has long been understood (Arrhenius 1896). However, it has not been until recent decades that anthropogenic global warming has been a public concern. To gain further understanding of future climate change, many researchers have focused their attention on Earth's polar regions. The transient warming response to increase of greenhouse gas concentrations is readily understood. However, the impact various large-timescale feedback effects, quantified

FIGURE 1.1: A map of Antarctica with locations of selected research stations indicated. Image and caption retrieved from Turner et al. (2005).

by climate sensitivity, the increase of temperature due to a unit change in radiative forcing, has proven difficult to predict in a warming climate. A further result of the many feedback mechanisms around the globe is polar amplification; paleoclimate records show Earth's poles have a much greater warming response to the increased radiative forcing than the rest of the world (Lee 2014). Over recent decades this has been observed in the Arctic, however, little evidence of polar amplification occurring in the Antarctic during recent decades exists. This result highlights the importance of understanding the Earth's polar regions.

This thesis is concerned with interactions between the lower atmosphere and the cryosphere, particularly in the Ross Sea region of Antarctica. The cryosphere is the layer of frozen water that blankets the coolest region of the world. This is

made up of several different types of ice: ice sheets, comprised of a thick layer of ice covering in the underlying topography, that originally fell as snow; ice shelves, the floating counterparts of ice sheets, filling in embayments with a thick, uniform layer of permanent ice; glaciers, gravity-driven rivers of ice that flow down mountain valleys and are generally fed from a large catchment area above; sea ice, frozen seawater that forms when the surface layer of the ocean freezes, which is generally relatively thin and much more dynamic than other types of ice, often only persisting for a single season. The Antarctic cryosphere contains the majority of Earth's fresh water supply. Change in the volume of ice contained within Antarctica's ice sheets is a major contributing factor to global sea level rise (Church et al. 2013). While warming temperatures increase the rate of melt at the continental margins, Frieler et al. (2015) report that snow accumulation over Antarctica may increase as much as $5\,\%\,K^{-1}$ due to the increased saturation pressure of the warmed air. This effect has been shown to counteract one-third of the Antarctic ice shelf mass loss (Medley and Thomas 2019), thus highlighting the need for a complete understanding of all components of Antarctic mass balance. Chapter 6 investigates precipitation events over the Ross Ice Shelf, and how atmospheric circulation patterns relate to these events.

Despite warming global temperatures, throughout the period of satellite observations, a small but significant positive trend in Antarctic sea ice extent (SIE) has been observed (Turner et al. 2015). This contrasts with the more intuitive negative trend observed in the Arctic (Comiso and Nishio 2008). Sea ice lies at the boundary of two complex and dynamic systems, the ocean and the atmosphere (Holland and Kwok 2012). Our ability to model sea ice processes, therefore, reflects upon our understanding of both systems (Hobbs et al. 2016; Holmes et al. 2019).

While the diminishing Arctic SIE has closely mirrored model predictions, increasing Antarctic sea ice trends are not reproduced by the majority of climate models (Comiso 2017; Holmes et al. 2019). This highlights a critical deficiency in our understanding of sea ice dynamics within the Southern Hemisphere. The net increase in Antarctic SIE is largely driven by changes within the Ross Sea (Drucker et al. 2011). A major source of sea ice production within the Ross Sea is polynyas, areas of open water within the ice pack that often form throughout the year. Chapter 4 of this thesis, therefore, discusses the effect of strong wind events on sea ice within the Ross Sea Polynya (RSP). In particular, the polynya opening and sea ice production mechanisms are investigated.

Sea ice also provides many feedback effects back onto the atmosphere. For example, a positive feedback on surface temperature occurs as sea ice has a much higher albedo than the underlying ocean, and therefore reflects insolation back into space. A decrease in SIE causes an increase in the amount of solar radiation that is absorbed at Earth's surface (Curry et al. 1995). Furthermore, sea ice forms a barrier between the ocean and the atmosphere preventing heat and moisture fluxes, as well as preventing the absorption of carbon dioxide. This isolates the continent from moisture sources and contributes to the low rate of snow accumulation over the Antarctic ice sheets during the austral winter (Bracegirdle et al. 2015). Polynyas offer a break in this isolating barrier, acting as a point source of both moisture and heat to the cool, dry atmosphere above. Chapter 5 analyses balloon observations in the vicinity of the RSP and investigates how the heat and moisture fluxes over the RSP are represented within the AMPS operational forecast model.

1.2 Thesis Structure

This thesis is comprised of seven chapters. Chapter 2 discusses the climate of the Ross Sea and its surrounding regions. It also describes the background physics relevant to this thesis (Section 2.1). Several data sets that were used throughout this thesis are also discussed (Section 2.2)

Chapter 3 discusses relevant aspects of Antarctic Sea ice. Several observational methods are discussed (Section 3.1) and sea ice trends over recent decades are described (Section 3.2), with particular focus on the minimum sea ice extent observed in 2016 (Section 3.2.1). The various factors that these trends are attributed to are then explored (Section 3.3).

Chapter 4 studies the effect of strong wind events on the RSP. Automatic Weather Station (AWS) data are compared to sea ice concentration (SIC) observations and sea ice drift vectors within the RSP to investigate the influence of strong wind events on the polynya. The polynya 'opening' process is investigated, and the persistence of the polynya is quantified. These processes lead to sea ice production and export within the RSP (Nakata et al. 2015).

Chapter 5 presents observations made using long-duration controlled balloons over the Ross Sea. Observations are compared to forecasts made by the Antarctic Mesoscale Prediction System (AMPS) during the same period. This comparison

provides some validation of the AMPS model. Lagrangian and Eulerian derivatives of potential temperature and total water mixing ratio are compared to analyse the heat and moisture fluxes that occur within the RSP, based on the AMPS forecast. The spatial footprint of these fluxes are also quantified.

Chapter 6 investigates the origins of moisture over the Ross Ice Shelf (RIS). Lagrangian back trajectories are used to identify the moisture sources for precipitation events over the RIS. The 'residence time' for moisture within the atmosphere is studied using trajectories of varying lengths.

Chapter 7 provides concluding remarks and discusses potential avenues for future research.

Chapter 2

Climate of the Ross Sea and Relevant Data Sets

2.1 Climate of the Ross Sea and Surrounding Regions

The Ross Ice Shelf (RIS) has an area of $487,000\,km^2$ - roughly 1.4 times the area of Germany (Jolly et al. 2016). This freely floating triangular-shaped ice shelf is almost completely devoid of orographic features beyond scales larger than 10 m. The northern edge of the RIS lies at approximately 78° S and is the southern-most coastline in the world.

The RIS is flanked to the west by the Trans-Antarctic Mountains, a large mountain range that rises abruptly to 2500 m with several peaks exceeding 4000 m. These mountains form a barrier constraining the East Antarctic Ice Sheet which feeds the RIS through several large outlet glaciers within valleys within the Trans-Antarctic Mountains. The north-eastern edge of the RIS is bordered by the more moderate slopes of the Siple Coast that lead up to Western Antarctic ice sheet (Figure 2.1).

The northern edge of the RIS borders the Ross Sea, this body of water is also flanked to the west by the Trans-Antarctic Mountains. The northern and eastern edges of the Ross Sea border the Southern Ocean and the Amundsen Sea respectively. For the majority of the year, the Ross Sea is covered by a layer of sea ice, with the sea ice retreating to a minimum in late February and advancing to a maximum in September (Figure 3.1). At the Southern extreme of the Ross Sea total sea ice cover persists from early March to late December (Figure 4.2), with the notable exception to the total sea ice cover being the few polynyas which open regularly throughout the winter (See Section 3.4 and Figure 3.10).

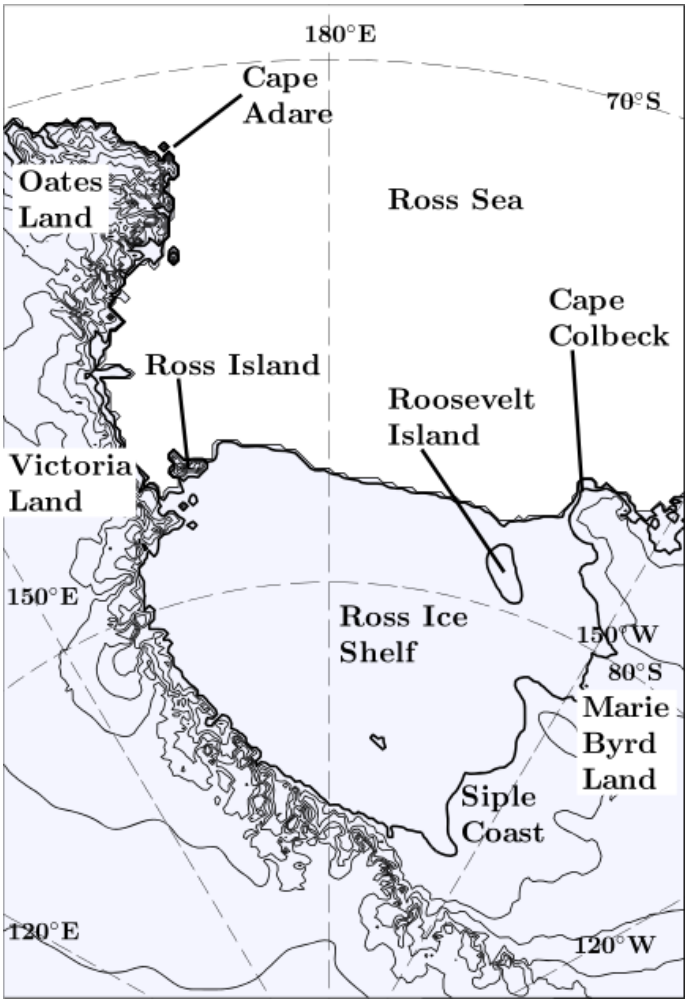

FIGURE 2.1: Map of greater Ross Ice Shelf and Ross Sea region. Topographic contours shown are at 10 m, 100 m, and every 500 m from 500 m to 3000 m. Topographic data are sourced from the Radarsat Antarctic Mapping Project Liu et al. (2001). Image and caption retrieved from Coggins and McDonald (2015)

2.1.1 Temperature inversions and static stability

The high latitude location of the RIS and the Ross Sea results in several months of continuous darkness during the austral winter. During summer months insolation is weak due to a combination of low solar zenith angle and the high albedo of the uninterrupted ice surface (Wendler et al. 2004). This often results in a temperature inversion forming; cool, negatively buoyant air settles near the ice surface with warmer positively buoyant air above. Temperature inversions are atypical within the troposphere which is generally characterised by positive lapse rates.

The atmospheric lapse rate ($\Gamma = -\partial T/\partial z$) is defined as the partial derivative of temperature (T) with respect to altitude (z). Lapse rates are often described in terms of potential temperature:

$$\theta = T(\frac{p_0}{p})^{R/c_p} \tag{2.1}$$

this is defined as the temperature that a parcel of air, with pressure (p) and initial temperature (T), would have if it were to be compressed or expanded adiabatically to a reference pressure (p_0), generally 1000 hPa (Marshall and Plumb 2007). R is the gas constant for air and c_p is the specific heat capacity at constant pressure for air. Using potential temperature in place of temperature removes the overlying temperature gradient due to the hydrostatic pressure gradient and reveals the remaining diabatic temperature changes.

Due to various diabatic processes that occur within the atmosphere, the environmental lapse rate (Γ_e) generally differs from the adiabatic lapse rate. The difference between the dry adiabatic lapse rate (Γ_d) and the environmental lapse rate is described by the vertical derivative in potential temperature:

$$\frac{\partial\theta}{\partial z}\frac{T}{\theta} = \Gamma_d - \Gamma_e \tag{2.2}$$

In conditions where $\Gamma_d < \Gamma_e$ (i.e. $\frac{\partial\theta}{\partial z} < 0$) if an air parcel were adiabatically perturbed upwards it would cool at a rate slower than its surroundings. This will result in the perturbed air parcel being at a final temperature warmer than its surroundings and therefore positively buoyant. In these conditions a small vertical perturbation will result in a positive feedback resulting in a large eventual displacement of the air parcel, these conditions are therefore unstable. Conversely, if the dry adiabatic lapse rate were to exceed the environmental lapse rate ($\frac{\partial\theta}{\partial z} > 0$) a restoring force would occur and the air would remain stable (Marshall and Plumb 2007).

As a rising air parcel cools it will eventually reach its dew point temperature. At this point, it will no longer cool at the dry adiabatic lapse rate as energy is being released as the water within the air parcel condenses. The parcel will, therefore, cool at the moist adiabatic lapse rate. This lapse rate is always less than the dry adiabatic lapse rate as the condensing water warms the air parcel. This makes an air parcel at saturation humidity less stable than one following the dry adiabatic lapse rate (Marshall and Plumb 2007).

In Antarctica, net radiative heat loss often occurs at the surface resulting in temperature inversions. This causes the lower troposphere to be particularly stable. This has several effects on Antarctic weather and climate. Vertically stable

air is often unable to move vertically over orographic features and instead must flow horizontally around these obstacles. This is described mathematically by the Froude number:

$$F_r = \frac{v}{\sqrt{gH\Delta\theta/\theta}} \tag{2.3}$$

Where v is the component of the wind velocity perpendicular to the slope and H is the height of the barrier. $\Delta\theta$ is the inversion strength defined as the difference in potential temperature between the surface and the top of the barrier and θ is the potential temperature at the surface (Lynch and Cassano 2006). If the Froude number is greater than unity, the air parcel will be able to traverse the barrier, otherwise, the air parcel will not possess the kinetic energy required to pass vertically over the barrier due to the static stability of the air. This can result in strong winds in regions where a large flow is forced through a small constriction by orographic features. For example, in the northwestern corner of the RIS winds often lack the required energy in pass over Minna Bluff, White Island, and Black Island, this causes increased wind speed in the narrow corridor between these islands (Chenoli et al. 2015; Seefeldt et al. 2003).

2.1.2 Katabatic flows

Katabatic flows are down-slope wind flows that occur frequently over many regions of Antarctica. When temperature inversions form on the high Antarctic plateau, cool dense air near the surface is negatively buoyant and drives flow approximately across topographic contours, towards the Antarctic coastline. The flow of cold air down a slope produced by katabatic forcing is analogous to water flowing down a hillside. These flows occur frequently throughout the Antarctic continent with increased frequency during winter when the absence of insolation strengthens the negative lapse rate near the surface, as heat is radiated upwards from the ice surface. Parish and Cassano (2003) demonstrated that katabatic forcing is much weaker during summer months when solar radiation provides heating at the surface. Zhou et al. (2009) further display that the diurnal solar cycle during summer months causes a diurnal variation in the strength of katabatic winds that is not present during winter months.

Ball (1956) present a simple two-layer model for katabatic flows. In an idealised system with two layers of uniform potential temperature with inversion strength $\Delta\theta$ and mean potential temperature $\bar{\theta}$, the katabatic force which points down the slope is:

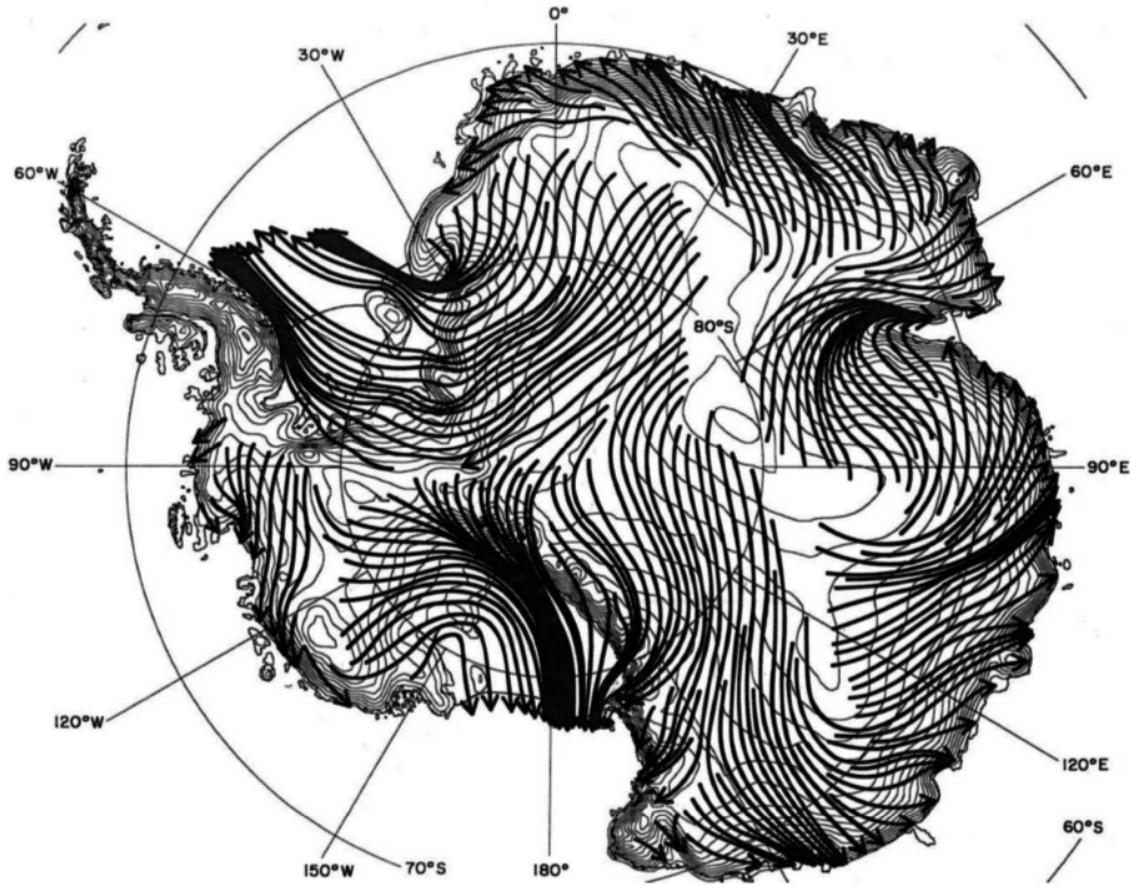

FIGURE 2.2: Mean streamlines at $\sigma = 0.9983$ over Antarctica from the June 2003-May 2004 AMPS archive. Image and caption retrieved from Parish and Bromwich (2007).

$$F_K = -g\frac{\Delta\theta}{\bar{\theta}}\frac{\partial z}{\partial x} \tag{2.4}$$

where $\frac{\partial z}{\partial x}$ is the slope of the surface. This force will balance with a pressure gradient force, a Coriolis force and a frictional force to give the net acceleration upon the air parcel (Lynch and Cassano 2006). The frictional term will always oppose the flow direction and the Coriolis force will always point to the left (Right in Northern Hemisphere) of the flow. The direction if the pressure gradient force will be variable, dependant on local and synoptic variability. In the absence of a pressure gradient force, the resultant flow will always be to the left of directly down-slope, due to the Coriolis force.

This simple katabatic model first described by Ball (1956) was used by Parish (1982) to model surface winds over East Antarctica and again by Parish and Bromwich (1987) over the entire Antarctic Continent. Later studies by Parish and

Waight (1987) and Parish and Bromwich (1991, 2007) have used increasingly complex models to simulate surface winds over the Antarctic Continent. These have all revealed similar results, with airflow generally following topographic gradients towards the coast. These flows calculated by Parish and Bromwich (2007) are demonstrated in figure 2.2 which shows streamlines at the $\sigma = 0.9983$ level - approximately 7-13 m above the surface.

Surface wind speeds are shown to be dictated by the local topographic slope (Parish and Bromwich 1987). Notable exceptions occurred in areas such as the Ross and Filchner-Ronne ice shelves. These are completely flat so air over these ice shelves is not subject to any katabatic force. However, large quantities of air flow into these regions off of the East and West Antarctic Ice Shelves. This causes katabatic drainage flows as airflow continues across these ice shelves allowing further export of cold air from the high plateau.

Although katabatic flows are driven by cool surface temperatures they are paradoxically associated with warmer surface temperatures at the Antarctic coast. Kurtz and Bromwich (1983) and Bromwich (1989) show apparent warming within katabatic outflows from several glacier valleys leading to the RIS (Figure 2.3). As the cold air descends from the Antarctic Plateau it warms adiabatically resulting in warmer temperatures at the coast. Surface friction within these strong jets also produces turbulent eddies that cause vertical mixing of air within the katabatic jet. This causes warm air to descend despite the inherent stability of the inversion structure (Bromwich 1989). This allows katabatic drainage flows to be easily identified through Thermal Infrared (TIR) satellite images (Figure 2.3) (Bromwich 1989; Bromwich et al. 1993, 1992, 1994). Cassano et al. (2016) also find that inversion strength over the RIS weakens rapidly due to turbulent mixing when wind speeds exceed $4\,\mathrm{ms}^{-2}$. This results in surface temperatures over the RIS increasing as katabatic winds, driven by cool surface temperature on the plateau, strengthen.

2.1.3 Amundsen Sea Low

The long-term average of pressure in the Southern Ocean reveals a region of climatological low pressure over the Amundsen and Bellingshausen seas, referred to as the Amundsen Sea Low (ASL) (Kreutz et al. 2000; Raphael et al. 2016; Turner et al. 2013b). A similar feature was first identified by Baines and Fraedrich (1989) using a scale model of Antarctica inside a rotating tank of water to simulate the atmosphere. In this physical simulation, cyclonic eddies were observed in the Ross and Weddell Seas as well as north of Prydz Bay. In model studies by Parish

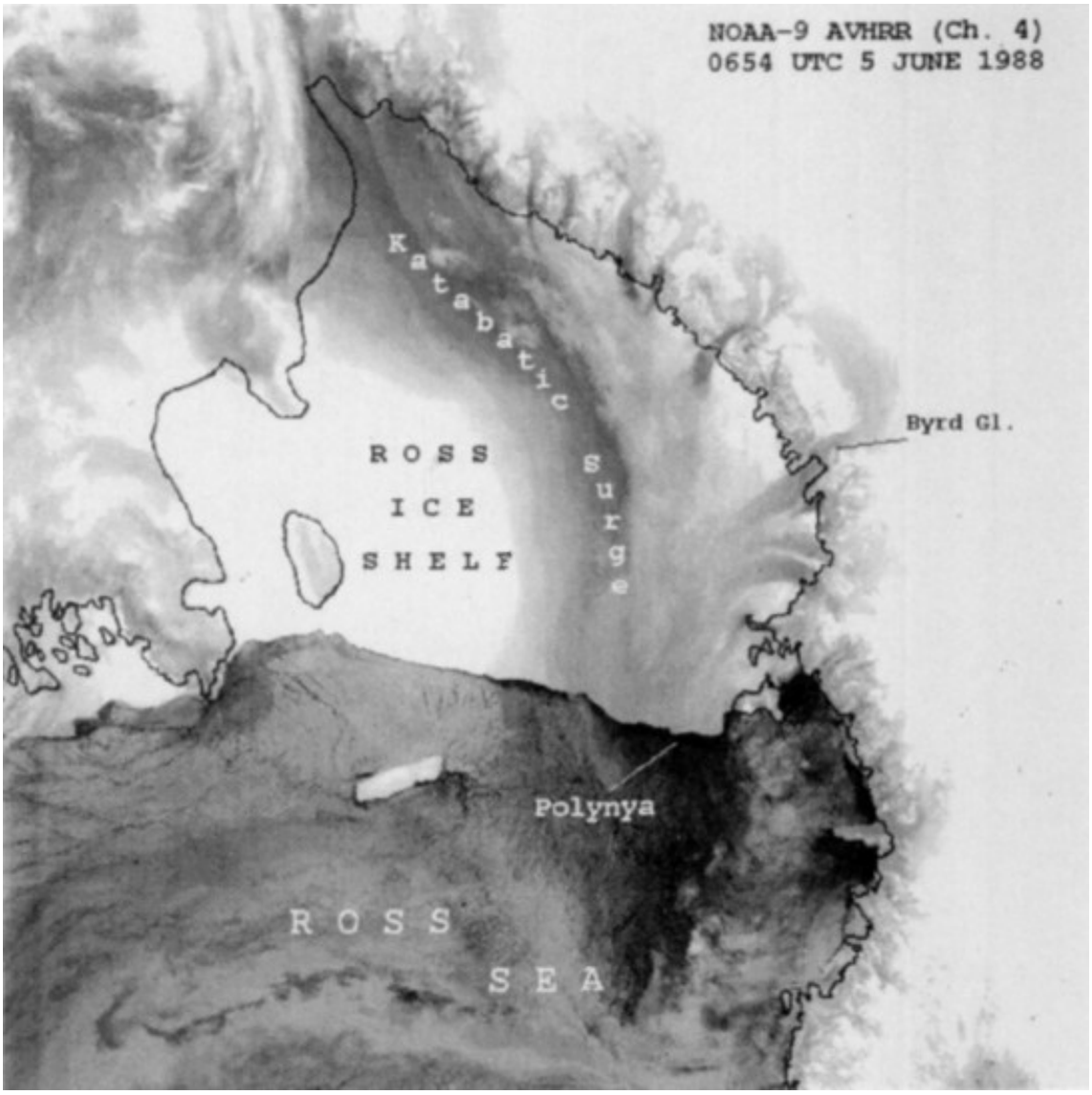

FIGURE 2.3: Thermal infrared satellite image of the Ross Ice Shelf at 1654 UTC 5 June 1988 showing katabatic surge across the shelf of West Antarctica. Image and caption retrieved from Bromwich et al. (1994).

et al. (1994) and Walsh et al. (2000) these cyclonic eddies were only able to be reproduced when Antarctic topography was modelled. Fogt et al. (2012) demonstrated a strong link between the frequency and intensity of synoptic cyclones within the Amundsen and Bellingshausen Seas and the depth of the ASL.

The location of the ASL varies with time, with variations in the zonal positions exceeding that of meridional variations (Coggins and McDonald 2015; Raphael et al. 2016). The location of the ASL, defined by the location of maximum pressure (Raphael et al. 2016), varies at such a magnitude that it is often centred over the Bellingshausen Sea and occasionally over the eastern Ross Sea. Because of this

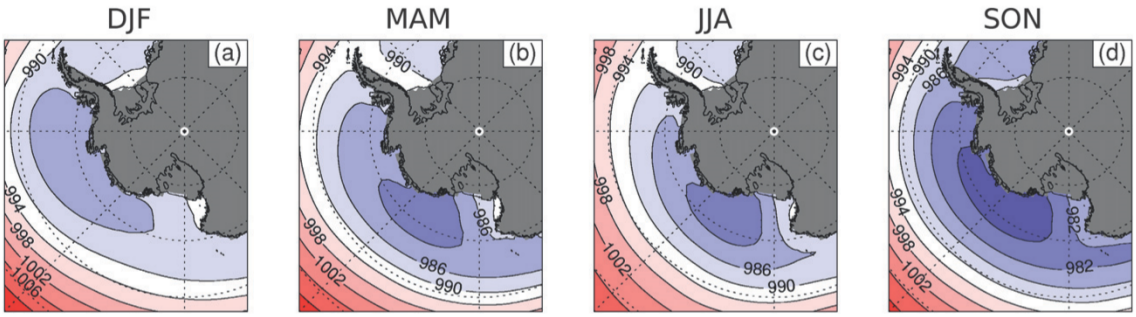

FIGURE 2.4: Seasonal mean MSLP (hPa) over the South Pacific sector of the Southern Ocean for (a) summer [December-February (DJF)], (b) autumn [March-May (MAM)], (c) winter [June-August (JJA)], and (d) spring [September-November (SON)] for ERA-Interim for the period 1979-2011. Image and caption retrieved from Hosking et al. (2013).

the ASL is often instead referred to as the Amundsen-Bellingshausen Sea Low (Fogt et al. 2012). The longitude of the ASL (referred to here as ASLx) varies seasonally, during winter the mean longitude is 220° E and during Summer the low migrates eastward to a mean longitude of 260° E (Figure 2.4) (Hosking et al. 2013; Turner et al. 2013b).

The central pressure of the ASL is strongly and significantly correlated to the phase of the Southern Annular Mode (SAM) (Clem and Fogt 2013; Hosking et al. 2013). The SAM, which describes the pressure difference between zonal regions at 40° S and 65° S, has shown a clear positive trend over recent decades (Gong and Wang 1999; Marshall 2003). Increasing SAM results in lower pressures at the Antarctic Coast relative to the northern Southern Ocean, thus resulting in deeper pressures at the latitudes of the ASL. Hosking et al. (2013) propose a relative ASL depth index that subtracts the mean pressure over the Amundsen Sea area. This removes large-scale pressure variations such as that of the SAM. The depth of the ASL varies annually with deeper lows observed during Winter compared to summer (Hosking et al. 2013).

The ASL induces a cyclonic airflow centred over the Amundsen Sea This has a large impact on the climate of The Antarctic Peninsula (Clem and Fogt 2013; Marshall and King 1998), West Antarctica (Hosking et al. 2013; Raphael et al. 2016), and the Ross Sea (Coggins and McDonald 2015; Cohen et al. 2013). A deepening ASL forces onshore flow over the Bellingshausen and Weddell Seas, opposing the prevalent offshore katabatic flows. This draws warm, moist, marine air onto the West Antarctic Ice Sheet (Nicolas and Bromwich 2011a). This causes warmer temperatures and an increased rate of precipitation over West Antarctica

and the Ross Ice Shelf.

Temperature variability related to the ASL over West Antarctica is coherent with the meridional flow induced by the ASL (Raphael et al. 2016). This suggests that the influence of the ASL within this region is caused by changes in atmospheric circulation related to a geostrophic flow around the climatological low-pressure region.

2.1.4 Ross Ice Shelf Air Stream

A key weather pattern that frequently occurs over the RIS called the Ross Air Stream (RAS) (Coggins et al. 2014; Parish et al. 2006; Schwerdtfeger 1984). This is characterised by strong, low-level, southeasterly winds flowing parallel to the Trans-Antarctic mountains. Initially, these flows were described as katabatic surges (Bromwich et al. 1993, 1992, 1994), this name is misleading as no katabatic force is possible on the flat ice shelf. Similar barrier winds have also been observed over the Antarctic Peninsula (Schwerdtfeger 1984).

These flows are initiated by synoptic-scale and mesoscale cyclones that frequently occur in the vicinity of Marie Byrd Land (Parish et al. 2006; Seefeldt and Cassano 2012). These cyclones force an easterly flow towards the Trans-Antarctic Mountains. Due to the high static stability that frequently occurs over the RIS, the flow regularly has insufficient kinetic energy to overcome the barrier of the Trans-Antarctic Mountains (Steinhoff et al. 2009). A region of high pressure, therefore, forms near the Trans-Antarctic mountains and the flow is redirected into a barrier flow following parallel to the mountain range (Lynch and Cassano 2006; Nigro and Cassano 2014a). This flow is reinforced by frequently occurring katabatic drainage flows from the Siple Coast and through glacier valleys in the Trans-Antarctic Mountains (Parish et al. 2006).

RAS events are renowned for extreme wind speeds, Steinhoff et al. (2008) report a particular event where wind speeds were so strong that the wind anemometer at McMurdo Station was blown away. Winds during RAS events are also directionally consistent (Jolly et al. 2016). Strongest wind speeds occur near prominences on the Trans-Antarctic Mountains, such as the Dufek Coast (Nigro et al. 2012b), Minna Bluff and just south of Cape Adare (Buzzi et al. 1997). The RAS is however characterised by strong winds across the entire western RIS (Nigro and Cassano 2014a; Parish et al. 2006).

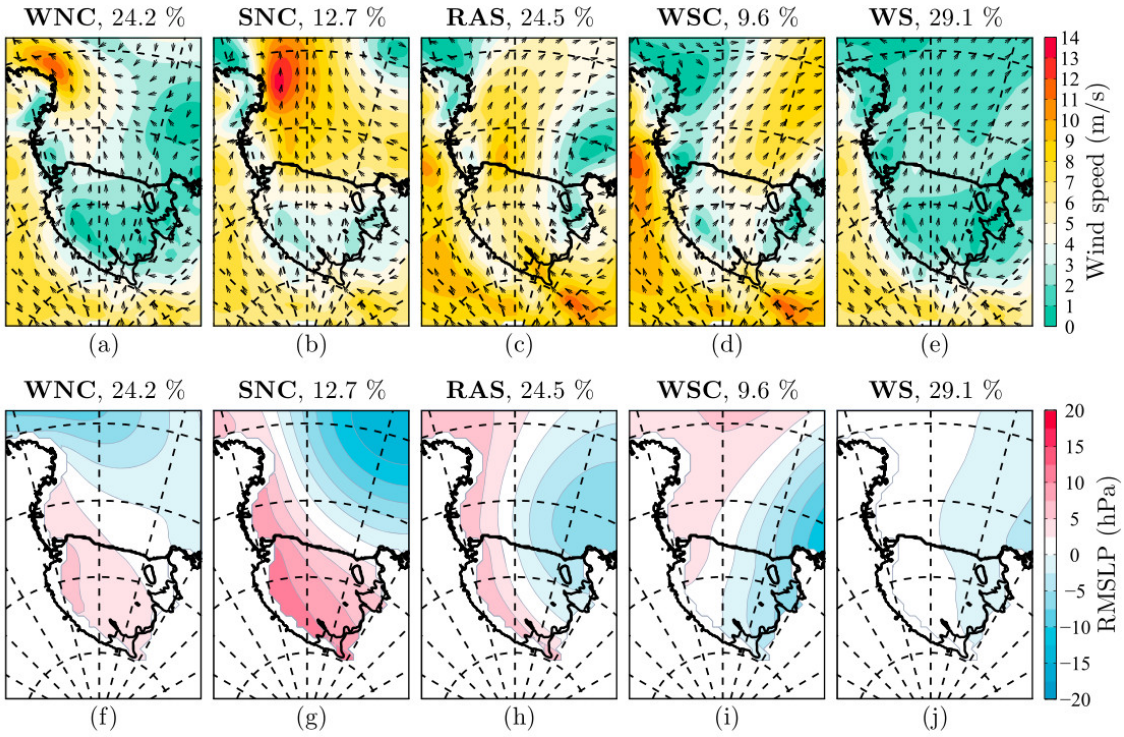

FIGURE 2.5: (a–e) Surface (10 m) winds of synoptic Coggins regimes. Arrows indicate direction in which wind is flowing and are plotted relative to grid north. Background colour represents the mean wind speed. Percentages above each diagram display the total frequency of the particular regime, computed annually. (f-j) As in Figures 2.5a-2.5e but for relative MSLP. Regime names are the following: WNC = Weak Northern Cyclonic, SNC = Strong Northern Cyclonic, RAS = Ross Ice Shelf airstream, WSC = Weak Southern Cyclonic, and WS = Weak Synoptic. Image and caption retrieved from Coggins and McDonald (2015).

A synoptic climatology was produced by Coggins et al. (2014), surface wind patterns from ERA-Interim reanalysis were clustered using a k-means clustering method resulting in 20 characteristic weather patterns. These were further grouped into 5 synoptic regimes (Figure 2.5). One of these regimes is the RAS that is identified to occur 24.5% of the time. Periods of RAS events have been observed, through both TIR images and direct Automatic Weather Station (AWS) observations, to have anomalously high temperatures (Bromwich et al. 1993; Cassano et al. 2016). This warming signature is constrained to areas of high surface wind speed, highlighting the influence of surface warming through turbulent vertical mixing (Coggins et al. 2014; Costanza et al. 2016).

RAS events are observed to occur at a higher frequency during winter months (Coggins et al. 2014; Seefeldt and Cassano 2012). During this period the three

forcing mechanisms that lead to a RAS event are also elevated (Nigro and Cassano 2014a). The deeper ASL during winter months and increased rate of cyclogenesis in the Ross Sea lead to an increased frequency of cyclones occurring in the vicinity of Marie Byrd Land (Hosking et al. 2013). Dramatically reduced insolation during winter months leads to surface cooling and increased stability of the air column, this strengthens the katabatic forcing and exaggerates the barrier effect of the Trans-Antarctic Mountains (Parish and Cassano 2003).

A case study of a single RAS event is presented by Steinhoff et al. (2009). During this event a synoptic-scale cyclone was observed offshore of Marie Byrd Land, moist air was drawn inland from the Amundsen and Bellingshausen Seas and continued across the Marie Byrd Land towards the RIS. Cloud formation was observed over the southern RIS. The TIR signatures of these clouds resembled that of surface warming due to katabatic flow breaking up surface inversions identified by Bromwich et al. (1993, 1992, 1994). This casts doubt on the previous assumption that warm TIR signatures indicate surface warming. However, warming can still be observed by in situ observations (Cassano et al. 2016).

RAS events have a significant influence on the climate of the RIS and surrounding areas. Moisture advection from the West Antarctic Ice Sheet delivers moisture to the RIS, this is particularly critical in the southern RIS which is distant from the Antarctic coastline (Nicolas and Bromwich 2011a). The strong winds and increased surface temperatures during a RAS event also facilitate the opening of the Ross Sea Polynya (RSP), this effect is a key focus of this thesis and is discussed in greater detail in both chapters 3.4 and 4.

2.1.5 Antarctic Precipitation

Although Antarctica is a continent characterised by an abundance of snow and ice, observations show that snowfall rates over Antarctica are very low. Snow accumulation through precipitation is the primary positive component in Antarctica's surface mass balance (SMB). Understanding of poleward moisture transport is therefore important as it has a direct influence on global sea level rise. As temperature rise, the moisture carrying capacity of air also rises, causing increased snow accumulation over the Antarctic ice sheets. Increased accumulation counteract one third of the ice sheet mass losses in Antarctica (Medley and Thomas 2019). Furthermore, understanding of the origins of Antarctic precipitation is required to allow correct interpretation of ice cores. Measurements made of Antarctic ice cores are one of the most important sources of information of paleoclimate state (Schlosser et al. 2010b).

The prevailing katabatic flows over the Antarctic surface warm adiabatically as they descend the slopes of the Southern Continent. Because of this adiabatic heating, a large diabatic cooling would need to occur if this air were to reach its dew point temperature and cause precipitation (Lynch and Cassano 2006). Furthermore, the northward advection near the surface must be opposed by southward flow at a higher altitude to maintain mass continuity causing a polar circulation cell (James 1989; Parish 1992; Parish and Bromwich 1998). This cold, high altitude air contains very little moisture due to its low temperature and physical distance from the nearest source of liquid water. This results in the Antarctic Continent being exceptionally dry, especially during the austral winter where katabatic winds are strengthened and sea ice prevents evaporation from a large swathe of the Southern Ocean.

Moisture transport to coastal regions of Antarctica occurs primarily through low-level southward intrusions of moist marine air driven by cyclones over the Ross Sea (Nicolas and Bromwich 2011a). The Southern Ocean is an area with a high number of cyclones occurring (Simmonds et al. 2003). Cold air is transported north by prevailing katabatic flows, this meets warmer, subtropical air over the Southern Ocean and causes an area of baroclinic instability. This instability leads to the frequent formation of cyclones, at Subantarctic latitudes, which facilitate Southward heat transport (Marshall and Plumb 2007).

Snowfall events in the Antarctic interior occur less frequently, with a small number of short events making up the majority of the annual precipitation. This leads to a large inter-annual variability in the accumulation rate (Gorodetskaya et al. 2013; Schlosser et al. 2010a, 2016). Precipitation events in the Antarctic interior often occur as a result of intensified Rossby waves in the circumpolar westerlies causing meridional moisture transport allowing moisture to travel poleward (Schlosser et al. 2010a,b, 2016).

2.2 Atmospheric Data Sets and Analysis Methods

2.2.1 Trajectory methods

Precipitation events are strongly tied to atmospheric circulation. Many authors use a Lagrangian back trajectory method to gain insight into the circulation patterns that result in precipitation (Dittmann et al. 2016; Markle et al. 2012; Scarchilli et al. 2011; Sodemann and Stohl 2009; Stohl and Sodemann 2010). Lagrangian trajectories describe the path that a free air parcel follows. Using wind vector data

from a numerical weather model, a Lagrangian trajectory can be approximated using numerical integration methods. Back trajectories specifically refer to trajectories that are propagated backwards through time, these are frequently used to investigate the origins of an air parcel.

An isentropic model is often used to approximate the vertical component of motion. This assumes that no diabatic heating occurs within the air parcel that is modelled. This assumption is particularly valid in the stratosphere where cloud rarely occurs (Friedrich et al. 2017; McDonald and Smith 2013; Smith and McDonald 2014). In the lower troposphere where cloud formation often results in diabatic heating, this assumption is less valid.

Back trajectories are of particular interest for investigating stable isotope ratios of ice samples recovered from ice cores. Paleoclimate temperatures are able to be recovered from these stable isotope ratios (Jouzel 2003). However temperature-dependant Rayleigh fractionation can cause uncertainties in these measurements. Back trajectories are frequently used to understand the temperature variations experienced by an air parcel between the moisture origin and precipitation site (Dittmann et al. 2016; Markle et al. 2012; Scarchilli et al. 2011). Lagrangian back trajectories are also frequently used in the analysis of particulate matter suspended within the air (Neff and Bertler 2015).

Sodemann and Stohl (2009) and Stohl and Sodemann (2010) use Lagrangian back trajectories to investigate circulation patterns over Antarctica. Moisture origins were found to vary seasonally with more northerly origins occurring during winter, due to seasonal sea ice preventing evaporation near the Antarctic Coast. Moisture origins were found to have strong asymmetry related to the topography of the Antarctic Continent.

2.2.2 Automatic Weather Stations

AWS networks can provide direct observations of surface weather conditions in remote regions of Antarctica (Lazzara et al. 2012). AWSs commonly measure wind speed and direction, temperature, pressure, and relative humidity. Other measurements that are less commonly made are snow depth, radiative balance, and winds and temperatures at multiple heights (Cassano et al. 2016). The remote locations of many AWSs are unreachable outside of the summer season, AWSs must, therefore, be designed such that maintenance is rarely required.

Powering an AWS is a large challenge, during winter, months of continuous darkness render solar panels useless and extreme wind speeds that frequently occur

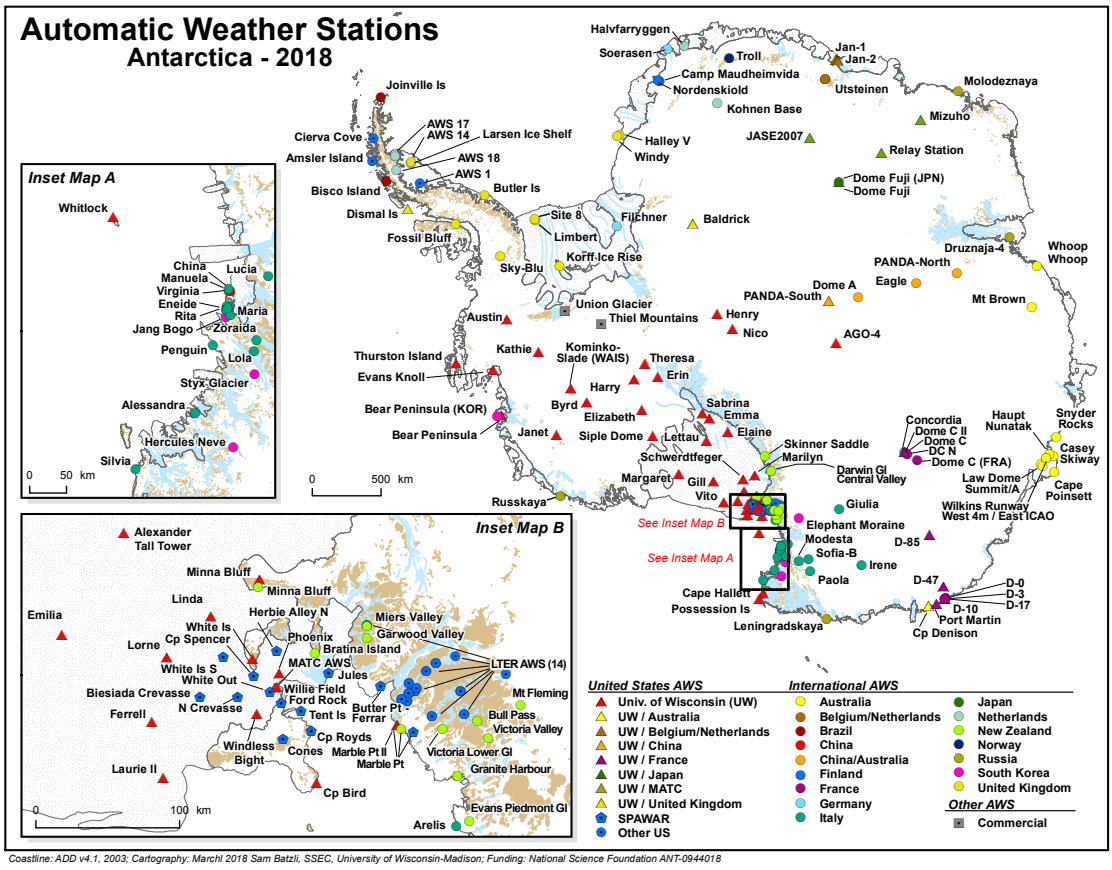

FIGURE 2.6: Map of Antarctica showing the locations of various AWS sites. Image retrieved from http://amrc.ssec.wisc.edu/aws/.

have been known to destroy wind generators. A proven method of powering an AWS during the winter is to minimise the power draw from the AWS and to have a large bank of batteries that are buried deep within the firn, this allows the batteries to maintain at the consistent firn temperature and eliminates the potentially damaging temperature extremes. This bank of batteries is then recharged gradually over the summer by a solar panel.

Data retrieval provides another logistical challenge. It is preferable to have data transmitted back in real time via satellite connection. This allows data to be used for weather prediction and removes the requirement for regular trips to retrieve data. This, however, increases the power usage and expense of each AWS. Data is generally transmitted via satellite link. The SNOWWEB wireless sensor network presented by Jolly et al. (2013) transmits data through an interconnected network of weather stations to a central base station to minimise the expense of real-time data transmission.

AWS only provide observations at very low heights, generally less than 10 m. Atmospheric conditions, particularly wind speeds, can have large variations due to surface interactions such as surface friction. Because of this wind speeds are often extrapolated to a reference height (usually 10 m) from the height of the AWS. This is done with an empirically fit log power law (Cassano et al. 2016). Snow accumulation and ablation will gradually bury or expose an AWS changing its height. Many AWSs must be regularly raised as accumulating snow raises around them.

The AWS data used within this thesis came from stations that were assembled and maintained by the University of Wisconsin-Madison (Lazzara et al. 2012). Data are for download available from http://amrc.ssec.wisc.edu/aws/. This AWS network covers most of Antarctica with an increased station density on the RIS especially near Ross Island (Figure 2.6). The data rate of the stations in this thesis used was 10 minutes.

2.2.3 ERA-Interim

A constant challenge of atmospheric science is comparing data sets from various sources. All data sets are observed on spatial and temporal domains dictated by their source. This often leaves large voids in our observational records. To remedy this issue meteorological reanalyses have been created. These assimilate data from many sources and use an atmospheric model to hindcast the atmospheric state on a consistent spatial and temporal grid. Antarctica is particularly troublesome for the accuracy of reanalyses due to the scarcity of suitable observations made in this region. The number of AWSs in Antarctica is by far the lowest of any continent on Earth (Lazzara et al. 2012), many satellites are also unable to observe over Antarctica due to the high orbital inclination required.

Chapters 4 and 6 make use of the ERA-Interim reanalysis (Dee et al. 2011). ERA-Interim is widely used throughout the atmospheric science community, and is noted for its accuracy in Antarctica and is generally considered the "standard" reanalysis in this region. ERA-Interim covers the globe with a $0.75^\circ \times 0.75^\circ$grid[1] and 60 vertical levels spanning from the surface to 0.1 hPa. As with other data sets relying on satellite observations, ERA-Interim covers a period starting in late 1979 continues until present. Data from various sources are assimilated into ERA-Interim including AWS observations, ship-based measurements, aircraft-based measurements, weather buoy observations, radiosonde observations, and remote sensing observations from various satellite sounders.

[1] approximately 80 km, although zonal grid spacing becomes increasingly small at high latitudes

ERA-Interim superseded the previous ERA-40 reanalysis the upgrade provided higher model resolution, improved model physics and improved assimilation techniques. Recently the successor to ERA-Interim, ERA5, has begun to be phased in. ERA5 boasts a 30 km resolution, 137 vertical levels, a one hour time step, and will eventually cover 1950-present. This increased resolution will present difficulties to researchers as one month of ERA5 output has a data volume of 11 TB. Although ERA5 is expected to represent an improvement from ERA-Interim, at the time of writing, there have yet to be any studies known to the author that confirm this.

Studies by Bracegirdle and Marshall (2012) and Bracegirdle (2013) have sought to test the validity of the ERA-Interim reanalysis within the troposphere above Antarctica and the Southern Ocean. Bracegirdle and Marshall (2012) compare the output from five different reanalyses with observations made at several manned Antarctic stations over a 30 year period. ERA-Interim was found to out-perform the other reanalyses when modelling all variables considered except surface temperature, model resolution was found to be the limiting factor. Bracegirdle (2013) found that out of the six reanalyses compared, ERA-Interim was the most capable when reproducing sea level pressure observations from floating buoys in the Bellingshausen Sea. A comparison of AWS and ERA-Interim wind speeds presented by Coggins et al. (2014) demonstrated good correlations between the two data sets, but ERA-Interim tended to underestimate wind speeds during strong wind events.

Bromwich et al. (2011) compare precipitation trends over the Southern Ocean within five reanalysis products over the 1989-2009 period. The various reanalysis products studied reveal conflicting precipitation trends over this period.

Analysis by Friedrich et al. (2017) compared observations from long-duration balloon flights in the stratosphere over the Southern Ocean with hindcasts from several reanalyses. The MERRA-2 reanalysis was found to slightly outperform ERA-Interim. Recent work by A. McDonald (personal communication, April, 2019) provides an intercomparison of the surface wind speeds by several reanalyses over the Ross Sea and Ross Ice Shelf and finds that, based on their mutual consistencies, MERRA-2 and ERA-Interim are the superior reanalyses in this region.

2.2.4 AMPS

The Antarctic Mesoscale Prediction System (AMPS) is a weather forecast that is generated twice a day with the primary purpose of informing logistical operators

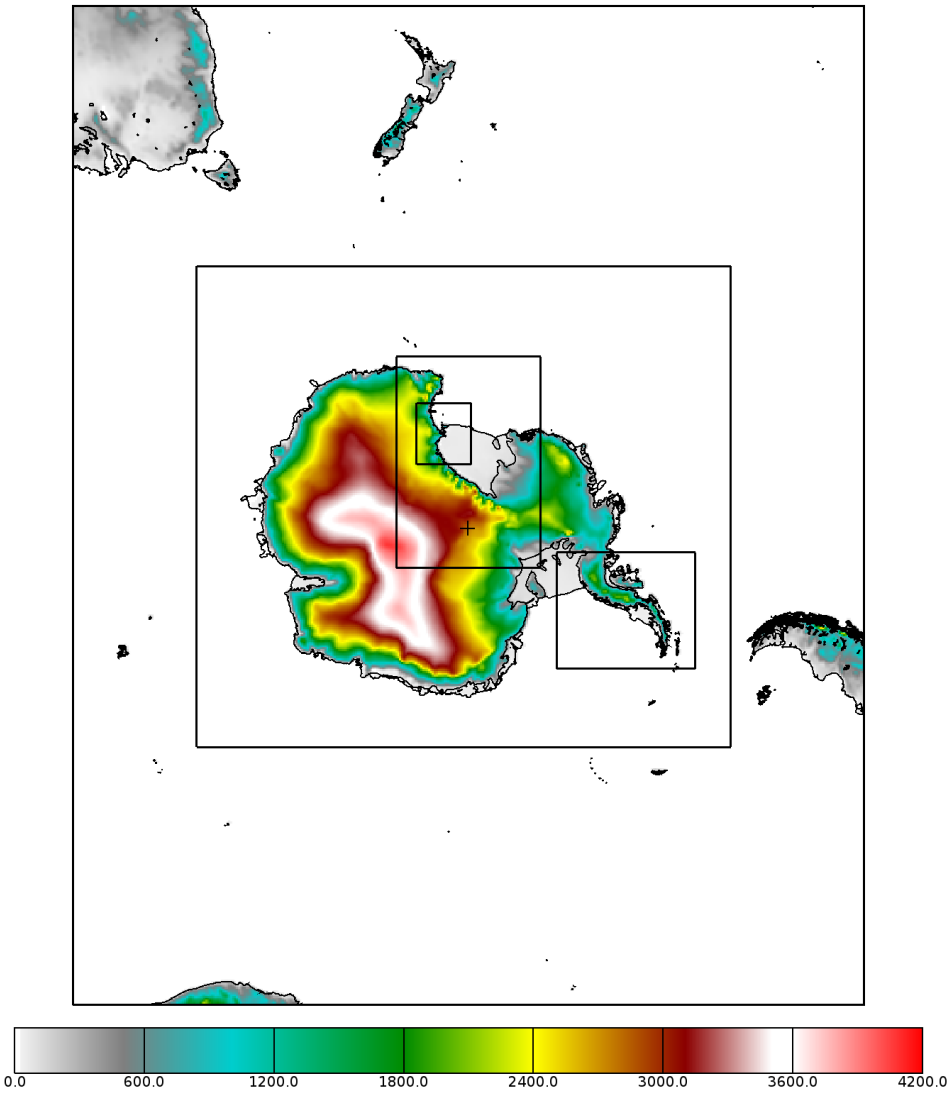

FIGURE 2.7: Map of the AMPS Domain 1 region with boxes indicating nested AMPS Domains. Shading indicates topography. Image retrieved from http://www2.mmm.ucar.edu/rt/amps/information/configuration/maps_2017101012/d1_colorfill_nests.png.

in Antarctica and the Southern Ocean (Powers et al. 2012). Because of the high spatial and temporal scale of AMPS the model also proves useful for meteorology studies of Antarctica (Nigro and Cassano 2014a; Nigro et al. 2012b; Schlosser et al. 2016). AMPS utilises a set of nested domains of varying scale and spatiotemporal model resolution. This focuses the computationally-expensive high-resolution domains over the areas with the highest density of ground and air operations. Particular focus is on Ross Island, home to McMurdo Station, the largest research station in Antarctica and two high frequently used airstrips.

Because AMPS aims to provide the most accurate forecast possible the model is

	Domain	Dimensions	Pixel Size	Time Step	Period
1	Southern Ocean	412 × 544	24 km	3 hr	121 hr
2	Antarctic Continent	834 × 786	8 km	3 hr	121 hr
3	Ross Sea and the South Pole	675 × 1035	2.67 km	1 hr	40 hr
5	Ross Island	768 × 900	0.89 km	1 hr	40 hr
6	Antarctic Peninsula	651 × 570	2.67 km	1 hr	40 hr

TABLE 2.1: Spatial and temporal scale and resolution of the current AMPS domains (10 October 2017 - Present). Note the previously used domain 4 was replaced in 2017 by the enlarged domain 3.

updated frequently. This makes the model unsuitable for long term studies such as trend analysis as discontinuities are likely to exist during the model updates.

AMPS uses a version of the widely used Weather Research and Forecasting (WRF) model with modifications made to make the model more suited for a polar climate (Powers et al. 2012). Several studies have tested the accuracy of this model (Bromwich et al. 2013; Jolly et al. 2016; Nigro and Cassano 2014b; Nigro et al. 2012a, 2011; Powers 2007). While AMPS is found to generally represent the atmospheric state well particularly during katabatic events where the winds are often directionally consistent. AMPS is shown to perform well in areas where the terrain is uniform such as the interior of ice shelves and ice sheets (Jolly et al. 2016). In regions of complex topography AMPS is limited by resolution, Nigro and Cassano (2014b) demonstrate a greater agreement between AMPS predictions and AWS observations within the 15 km grid compared to the 30 km grid. Prior to 2006 AMPS used a MM5 model, this was also shown to agree well with observations (Bromwich et al. 2005, 2003; Guo et al. 2003).

Chapter 3

Antarctic Sea Ice Trends and Drivers of Change

Every winter, as the Antarctic continent is enveloped in continual darkness, over 15 million square km of the Southern Ocean is covered in a layer of frozen seawater known as sea ice[1]. This area exceeds the landmass of the Antarctic continent itself (Parkinson and Cavalieri 2012). Antarctic sea ice reaches its maximum extent during September. Once the austral winter ends and temperatures rise, sea ice begins to melt and the sea ice extent decreases. Minimum sea ice extent occurs at the end of the summer season as the sun sets around February/March.

Sea ice lies on the boundary between the ocean and the atmosphere and is therefore sensitive to change in either system. Understanding of sea ice in the Southern Ocean is fundamental in making predictions of Antarctica's entire climate system (Agosta et al. 2015; Hobbs et al. 2016). The ocean and the atmosphere are isolated by an insulating barrier of sea ice, thus limiting heat and moisture fluxes from the ocean to the atmosphere. This reduced moisture flux decreases the rate of precipitation, and hence the surface mass balance (SMB) over the Antarctic continent (Bracegirdle et al. 2015). The reduced heat flux between the ocean and the atmosphere allows the ocean to remain relatively warm[2] throughout winter whilst surface air temperatures rarely reach above -20° C. The physical barrier sea ice provides also has ecological influences (Massom and Stammerjohn 2010).

Sea ice and the snow cover that falls upon it causes a large change in the local albedo compared to that of seawater in which would otherwise occupy the area (Curry et al. 1995). This causes a large change in the amount of energy absorbed from solar radiation, drastically influencing the local climate.

[1] Sea ice should not be confused with icebergs. Sea ice is frozen seawater while icebergs are freshwater ice calved off of land-borne glaciers and floating ice shelves.

[2] A mixture of sea ice and sea water will always remain at ~-1.8° C with small variations in temperature depending on salinity.

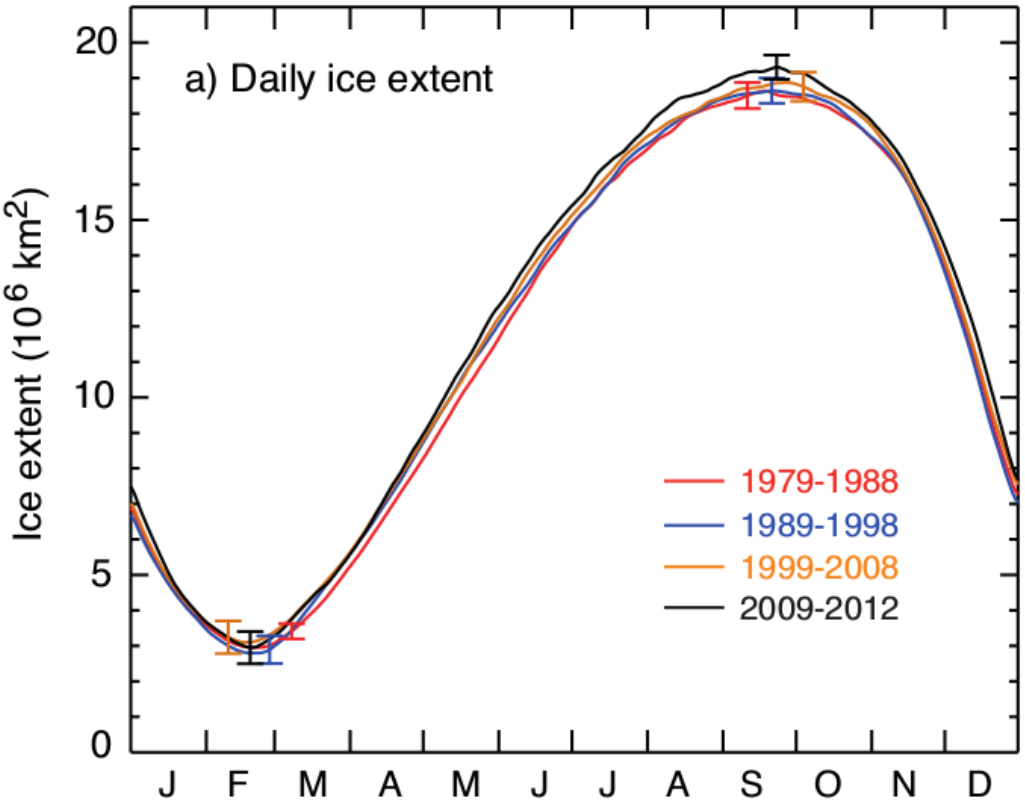

FIGURE 3.1: Decadal averages of daily Southern Hemisphere SIE. Note the 2009-2012 period only contains a four year mean. Image sourced from Vaughan et al. (2013).

As sea ice forms, a large amount of salty brine is ejected into the surrounding seawater. Brine sinks rapidly due to having a greater density than the surrounding seawater. The descending fluid leads to the formation of Antarctic bottom Water (AABW), driving large circulating currents within the Southern Ocean (Budillon et al. 2011; Dinniman et al. 2018). These currents dominate the global climate as they carry heat flux and nutrients around the world's oceans (Marshall and Speer 2012).

3.1 Sea Ice Observations and Metrics

Due to the large size and the remote, inhospitable nature of Earth's polar regions, the amount of sea ice that exists on Earth at a given time is a difficult value to measure directly. For much of the year, constant darkness and the thick layer of sea ice itself prevent the safe passage of ships to the polar regions. As a result, direct observations of sea ice are rarely made during winter beyond a short distance from

the few permanent coastal stations. Most sea ice measurements are made from orbiting satellites using remote sensing techniques. Passive microwave brightness temperature measurements such as those taken from the Scanning Multichannel Microwave Radiometer (SMMR), the Special Sensor Microwave/Imager (SSM/I), the Special Sensor Microwave/Imager Sounder (SSM/IS), and the Advanced Microwave Scanning Radiometer - Earth Observing System (ASMR-E) instruments are of the greatest interest to sea ice researchers. By analysing these data it is possible to distinguish between sea ice and liquid water based on their differing emissivities at varying frequencies and polarisations (Zwally et al. 1983). Microwave radiation is able to penetrate clouds; measurements made with these instruments allow for uninterrupted sea ice records to be produced. These data are archived at, and available from, the National Snow and Ice Data Centre (NSIDC) in Boulder, Colorado (Armstrong et al. 1994). From these daily measurements, sea ice concentration (SIC) is derived using various algorithms. Sea ice records based on these data begin in the late 1970s and provide a continuous record until the present day.

3.1.1 SIC algorithms

SIC is defined as the percentage of each pixel that is covered with sea ice. From this, sea ice area (SIA) and sea ice extent (SIE) can be calculated. These are often used as they provide a one dimensional metric for how much sea ice exists at any given time. This is convenient for uses such as trend analysis. SIA and SIE can be calculated for an entire hemisphere or for several sub-regions, allowing geographical differences in trends to be analysed.

Two widely used SIC products have been developed by separate teams within the NASA Goddard Spaceflight Center. These are the Bootstrap algorithm (Comiso 1986, 2000; Comiso et al. 2017; Comiso and Nishio 2008), and the National Aeronautics and Space Administration (NASA) Team algorithm (Cavalieri et al. 1984, 1996, 1999). Both of these algorithms utilise SMMR, SSM/I, and SSM/IS passive microwave brightness temperatures (TB). While these algorithms are physically motivated they both utilise an empirical implementation. The Bootstrap and NASA Team retrievals have also been combined to form the Goddard-Merged (GM) estimate (Meier et al. 2013a; Peng et al. 2013). Ivanova et al. (2014) and Ivanova et al. (2015) compare various SIC algorithms and conclude that insufficient ground truthing measurements prevent a optimal SIC algorithm from being discerned.

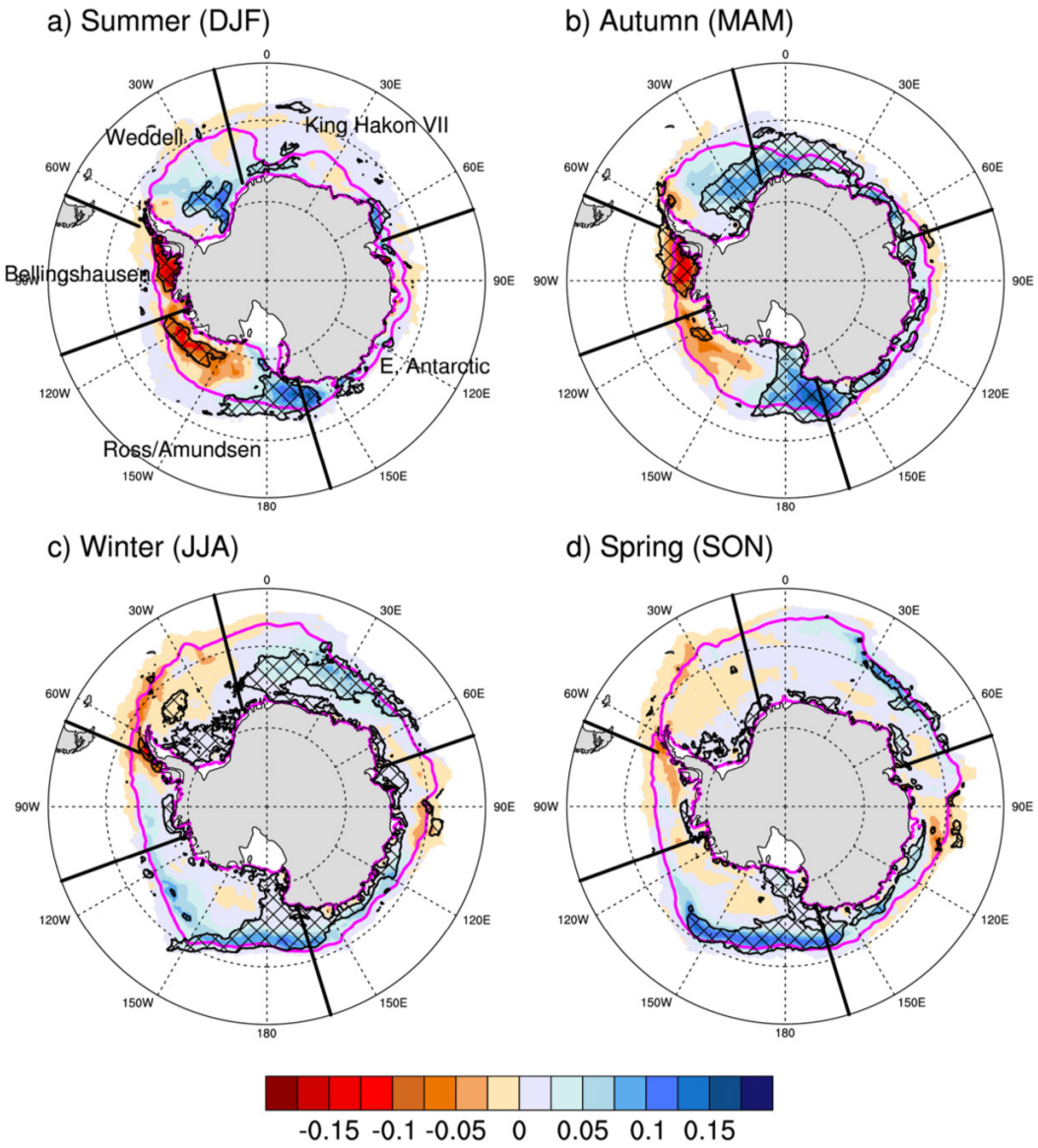

FIGURE 3.2: 1979-2014 seasonal SIC trends (fraction/decade). The magenta line indicates the climatological 15% SIC isoline. Hatched areas indicate trends greater than a 95% significance level. Image sourced from Hobbs et al. (2016)

Brightness temperature preprocessing

Both the Bootstrap and NASA team algorithms utilise similar quality control prepossessing methods on the microwave brightness temperature prior to the calculation of SIC. As these retrievals span the lifetime of multiple sensors (See Figure 3.3), the algorithms must be calibrated to avoid discontinuities within the data set (Cavalieri and Parkinson 2012; Meier et al. 2011).

Although the passive microwave data does penetrate clouds, some artefacts due to atmospheric moisture are still found. A weather filter based on TB ratios is

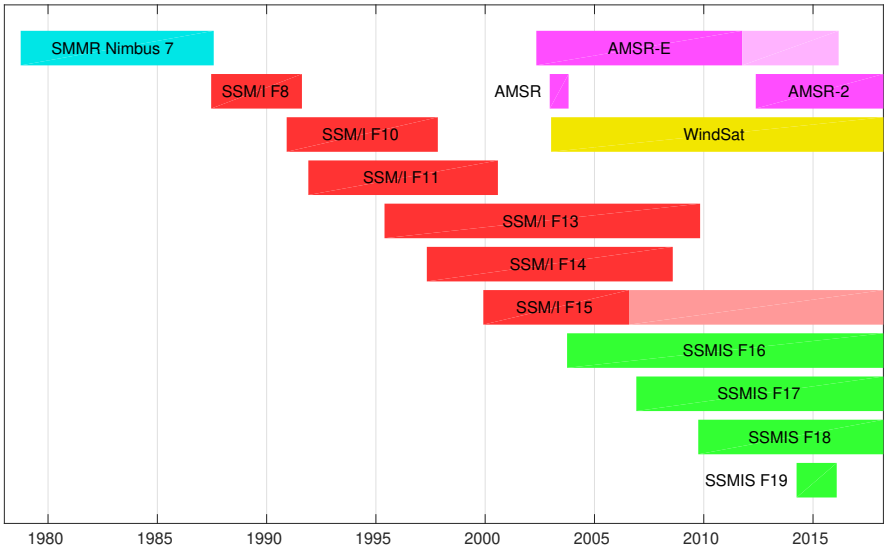

FIGURE 3.3: Lifetimes for various satellite based passive microwave radiometers used in sea ice retrievals. The faded areas in the AMSR-E and SSMIS F15 bars indicate periods where, due to technical issues, these instruments recorded data of limited use.

used; this also removes inappropriately low SIC values due to wind-driven ocean roughness (Comiso and Nishio 2008).

Snow upon land will also be identified as sea ice by both retrieval methods. To prevent this, pixels that contain only land and permanent ice, such as shelf ice, are masked. Pixels that contain both ocean and land are corrected to prevent erroneously high SIC values.

Where an isolated missing data point exists within the TB fields, the values are filled using a spatial bilinear interpolation. For large areas of missing data, such as missing swaths, values are instead filled using a temporal interpolation of the final SIC field (Meier et al. 2014).

Passive microwave measurements are used as these allow continuous observations during cloudy periods. However, these observations are of relatively low resolution. The temporal and spatial resolution of the TB grid is limited by the observations. While it is possible to make higher resolution observations at higher frequencies, these frequencies are unable to penetrate cloud layers and cannot provide continuous observations.

Bootstrap SIC

Bootstrap SIC is available on a $25\,km \times 25\,km$ polar stereographic grid and spans 1979 to present. The Bootstrap algorithm was updated in 2007 to version 2 and again in 2017 to version 3, these and the previous version 1 are available on the NSIDC website (Comiso 2000, 2017; Comiso et al. 2017; Comiso and Nishio 2008). Compared to other algorithms the Bootstrap version 1 data tend to underestimate SIE, particularly in East Antarctica (Hobbs et al. 2016). Eisenman et al. (2014) report a spurious increase in SIE trends between these two versions related to the transition between sensors in January 1992, this issue has since been corrected and the data reprocessed (Comiso 2017; Comiso and Nishio 2008). The Bootstrap version 2 algorithm has been shown to often underestimate concentrations at very low temperatures (Meier et al. 2014).

NASA Team SIC

The NASA team SIC product (Cavalieri et al. 1996) uses the same $25\,km \times 25\,km$ polar stereographic grid as the Bootstrap retrievals. The NASA team SIC retrievals utilise the vertical polarisations of 18 GHZ and 37 GHz channels and the horizontal polarisations of 18 GHz channel from the SMMR instrument prior to 1987. After 1987 19.3 GHz channel from the SSM/I and SSM/IS instruments replaced the previously used 18 GHz channel. The NASA team algorithm has been found to underestimate the SIC when there are strong surface emissivity variations such as near the ice edge and in melt pools (Cavalieri 1994; Meier et al. 2014).

Goddard-Merged SIC

The Goddard-Merged (GM) SIC data set (Meier et al. 2017) was created with the intention to limit the unique errors in the Bootstrap and NASA Team retrievals as both algorithms have been found to underestimate the SIC (Kwok 2002; Meier 2005). The GM algorithm exploits this by taking and using the greater SIC value from either NASA Team or Bootstrap retrievals. This produces a data set that minimises SIC underestimations in comparison to both NASA team and Bootstrap retrievals. The GM retrievals are gridded on the same NSIDC $25\,km \times 25\,km$ polar stereographic grid as the NASA team and Bootstrap products and also contain a standard deviation field describing the spatial and inter-model variance of the NASA team and Bootstrap retrievals; this can be used to indicate areas where the SIC retrievals are less likely to be reliable (Peng et al. 2013).

3.1.2 Sea ice area and extent

Sea ice area is defined as the total area of sea that is covered by ice and can be calculated by multiplying the area of each pixel by the SIC within the respective pixel (Comiso and Nishio 2008).

Sea ice extent is the summed area of all pixels with a SIC exceeding 15% (Comiso and Nishio 2008)[3]. When calculating SIE, some authors choose to ignore holes within the ice pack, such as polynyas, essentially calculating the sea area polewards of the ice edge (Hobbs et al. 2016). SIC retrievals are often unreliable at concentrations less than 10%, such as in the marginal ice zone where emissivities are variable (Zwally et al. 1983). SIE is often used preferentially over SIA as it reduces these potential errors associated with SIC calculations.

3.1.3 Sea ice thickness and volume

While SIC measurements are a valuable asset to sea ice research, they can only provide a limited viewpoint. A complete understanding of sea ice dynamics and trends require measurements relating to sea ice thickness and volume (Maksym et al. 2012). Heat flux and brine rejection are both proportional to the regional sea ice volume flux. These dictate the net northward freshwater flux, AABW production and high salinity shelf water production (Dinniman et al. 2018). Unfortunately, reliable sea ice thickness measurements can currently only be made via in situ observations, mostly near dedicated research stations or during ice breaker campaigns (Haas et al. 2008).

An effort has been made to find a remote sensing solution for measuring sea ice thickness, by inferring sea ice freeboard from satellite laser altimeter measurements and incorporating this into simple buoyancy calculations (Fons and Kurtz 2018; Giles et al. 2008; Kwok 2010; Price et al. 2019). However, this method requires an estimate for the density of the sea ice, but a snow layer of unknown thickness accumulates upon the ice surface. As snow is less dense than ice, the estimated bulk density is unreliable, thus preventing accurate sea ice thickness calculations. Currently, snow depth upon Antarctic sea ice is unable to be measured remotely (Pope et al. 2017).

Sea ice thickness represents a large gap in our observational record. Without a consistent record for sea ice volume, sea ice production is difficult to measure.

[3]While 15% is the most frequently used some authors choose to use other thresholds when calculating SIE.

Kurtz and Markus (2012) find that Antarctic sea ice thickness trends oppose those of SIE resulting in a minimal net change in sea ice volume over recent decades.

3.1.4 Sea ice drift

Sea ice motion can be calculated using a maximum-cross-correlation algorithm. This takes a small section of a brightness temperature image and calculates a correlation of this sub-image with every other sub-image from the next time-step within a given search radius. The search radius represents a maximum plausible drift speed (Heil et al. 2006). From the location of the sub-image that resulted in the highest correlation, a displacement for the sea ice can be inferred (Holland and Kwok 2012).

This method assumes that features within the brightness temperature image do not change significantly between two consecutive time-steps. Detection of sea ice motion is hindered if rotation or deformation of the sea ice occur at a rate faster than the temporal resolution of the data set (Emery et al. 1997).

3.1.5 Historical records

Prior to 1979, observations of Antarctic sea ice were scarce. Studies of long term trends and changes to the variability of sea ice are therefore limited by the short satellite period.

Gallaher et al. (2014) and Meier et al. (2013b) used visible and infrared images from the NIMBUS 1, 2, and 3 satellites to deduce SIE over several periods spanning between 1964-1970. These data were temporally inconsistent and less accurate than those derived from modern multi-channel passive microwave instruments. Unfortunately, this period did not overlap with the period of operation for passive microwave instruments, so cross-validation tests to ensure consistency are not possible.

Prior to satellite observations, measurements had to be made in-situ. Cotté and Guinet (2007) and De La Mare (2009) used historical data from whaling ships during the 1930-1980 period to infer a northern ice edge. As whaling ships preferred the ice edge whale catch locations were assumed to be direct proxies for the northern ice edge.

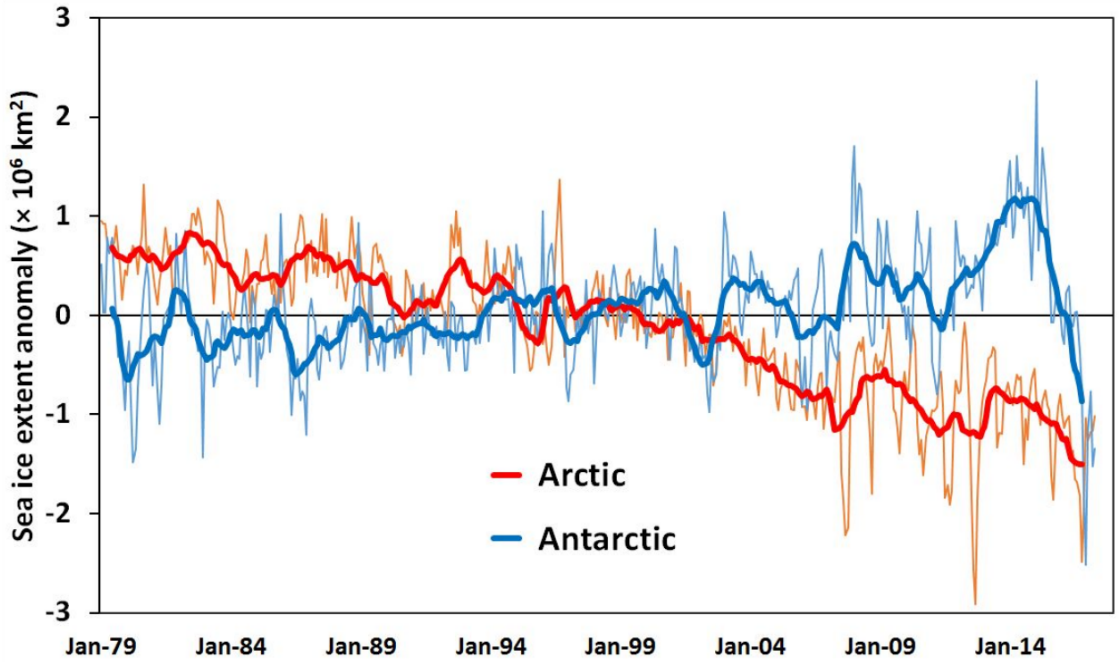

FIGURE 3.4: The Arctic and Antarctic monthly SIE anomalies for 1979-2017 based on the 1981-2010 means. Thin lines show monthly data, with the 12 month running mean data indicated by bold lines. Image and caption retrieved from Turner and Comiso (2017).

3.2 Trends in Antarctic Sea Ice Extent

Although warming trends have been observed throughout the satellite period[4], many authors (Comiso 2017; Comiso and Nishio 2008; Fetterer et al. 2002; Jones et al. 2016; Parkinson and DiGirolamo 2016; Simmonds 2015; Turner et al. 2015) have reported significant positive trends in Antarctic SIE over the same period (Figure 3.4). Record maximum SIE was also recorded in 2012, 2013, and 2014 (Reid et al. 2015). This perplexing result contrasts with the trends observed in the Northern Hemisphere, where a significant negative trend in SIE, and many record-breaking SIE lows, have been observed (Comiso and Nishio 2008; Parkinson and Comiso 2013; Serreze and Stroeve 2015) (Figure 3.4). The trends in Northern Hemisphere SIE observed since 1979 are attributed to recent global warming caused by anthropogenic greenhouse gases (Zhang and Walsh 2006). Whilst warming temperature trends have been observed in many regions of the southern continent (Turner et al. 2005), the expected decreasing response in SIE has not been observed over this period.

An increasing overall SIE trend is observed in the Southern Hemisphere, masking a large amount of regional and seasonal variability (Comiso and Nishio 2008;

[4]1979-present

Region		Year	DJF	MAM	JJA	SON
Whole Antarctic		186**	129	220**	173**	201**
Ross Sea	(160°E–130°W)	117*	95	106*	123**	143*
Amundsen-Bellingshausen	(130°W-60°W)	-54	-104**	-118**	0	-4
Weddell Sea	(60°W-20°E)	46	98	139*	-38	-23
Indian Ocean	(20°E-90°E)	55**	40	48*	71*	68
Western Pacific Ocean	(90°E-160°E)	22	13	43	16	9

*p< 0.05, **p<0.01

TABLE 3.1: Annual and seasonal trends in Southern Hemisphere SIE (10^3 km^2 per decade) for 1979–2013. Statistical significance of these trends are indicated by asterisks. Data and caption retrieved from Turner et al. (2015)

Turner et al. 2015). The greatest positive trends are observed within the Ross and Weddell Seas, whilst negative trends are observed within the Amundsen and Bellingshausen Seas; this variation is detailed in Table 3.1. If SIA is considered instead, the resultant pattern found is similar to that of SIE. Although the trends vary between SIA and SIE, the sign of the trends for each region and season remains the same (Parkinson and Cavalieri 2012).

Turner et al. (2013a) compare the observed Southern Hemisphere SIC record with that predicted by 18 models of the Coupled Model Intercomparison Project phase 5 (CMIP5). It was found that these models were unable to predict the magnitude of the observed positive SIE trend, with the majority of models displaying a negative SIE trend (Zunz et al. 2013). Recent work by Holmes et al. (2019), uses a more complete set of CMIP5 members. While a wide range of historical SIAs are hindcast by the CMIP5 models some models were able to reproduce the observed SIA patterns. Furthermore, one model was able to accurately reproduce the observed sea ice budget, indicating that compensating errors were not a factor. This demonstrates that accurate sea ice modelling is possible with current model resolutions, and that a complete understanding of both atmospheric and oceanic forcing is required.

3.2.1 2016 record low SIE

Despite significant increasing trends in Antarctic SIE being observed from 1979 to 2015 and record maximum SIE being recorded in 2012, 2013, and 2014, SIE was observed to reach a record minimum in March 2016 (Figure 3.4) (Doddridge and Marshall 2017; Stuecker et al. 2017; Turner et al. 2017; Wang et al. 2019). This abrupt departure form the long-term trend was not expected and adds further confusion to the puzzle of Antarctic SIE (Turner and Comiso 2017). SIE anomalies

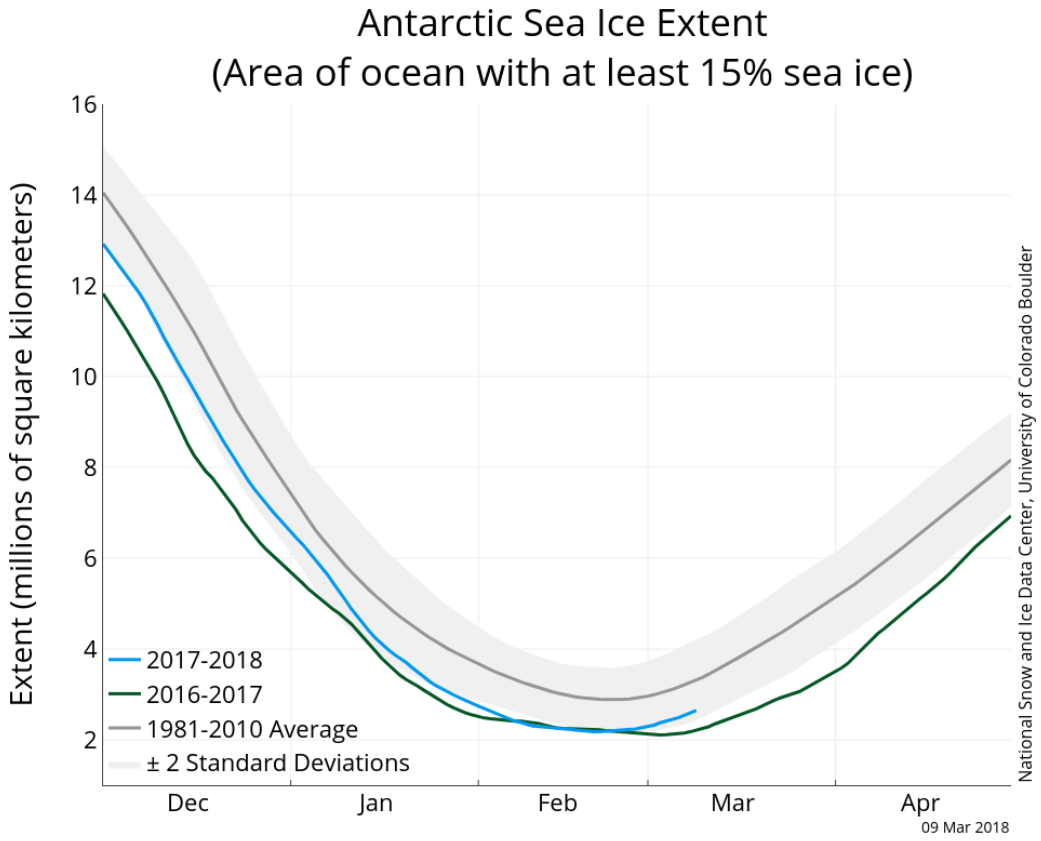

FIGURE 3.5: Daily SIE in the Southern Hemisphere for the austral summer. The grey line indicates the mean SIE for the 1981-2010 period, with the light gray area indicating the $\pm 2\sigma$ range for this period. The Green and Blue lines indicate the SIE during the 2016-17 and 2017-18 summers. Image and caption retrieved from Fetterer et al. (2002).

reached record minima between 3rd November 2016 and the 9 April 2017 with the absolute minimum of 2.07×10^6 km^2 occurring on the 1st March 2017 (Figure 3.5) (Turner et al. 2017). This sea ice event came with warming of most sectors of the Antarctic Continent and Southern Ocean (Ionita et al. 2018).

During September 2016, the first period of anomalous retreat, the Southern Annular Mode (SAM) index was positive and Mean Sea Level Pressure (MSLP) was the lowest value hindcast by ERA-Interm data in the Amundsen Sea Low (ASL) (Figure 3.7a). The enhanced northwesterly flow over the Weddell Sea, driven by the deep ASL, amplified the sea ice retreat in the Weddell Sea (Turner et al. 2017). October 2016 saw sea ice retreat at a rate 35% greater than the mean for the satellite period (Turner et al. 2017). Figure 3.7b indicates that strong meridional wind anomalies occurred in many regions surrounding Antarctica. Meridional winds have a much stronger impact on SIE compared to zonal winds (Holland

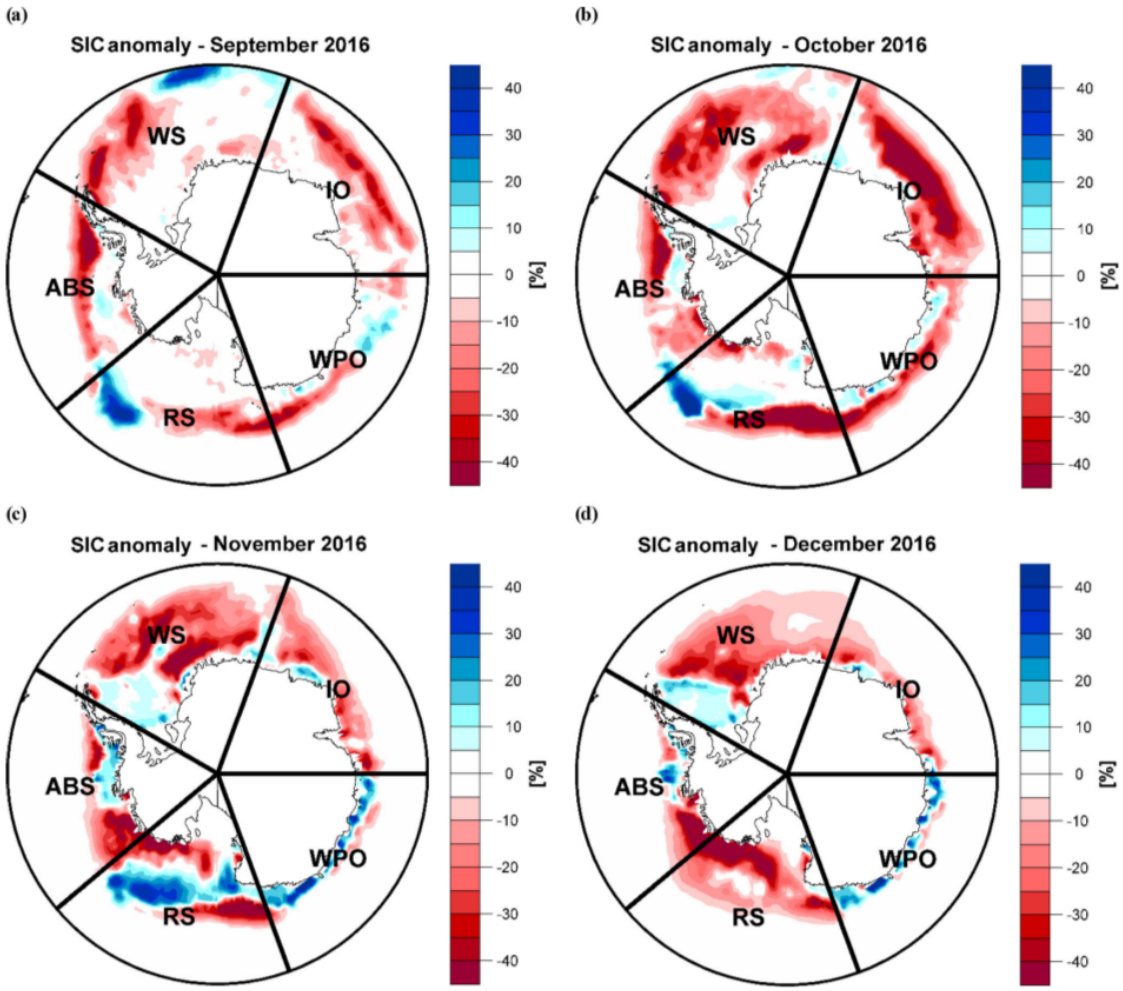

FIGURE 3.6: Sea ice concentration SIC anomalies 2016 for (a) September, (b) October, (c) November, and (d) December. The anomalies are computed relative to the reference period 1979–2010. WS: Weddell Sea; IO: Indian Ocean; WPO: western Pacific Ocean; RS: Ross Sea; ABS: Amundsen–Bellingshausen Sea. Image and caption retrieved from Kusahara et al. (2018)

and Kwok 2012).

The largest retreat anomaly occurred during November 2016. The SIE decrease observed in this month was 34% larger than the mean for the satellite period and the most rapid November retreat on record (Turner et al. 2017). This retreat occurred mostly in the Weddell sea with 62% of the November SIE anomaly occurring within this region (Turner et al. 2017).

This extreme sea ice event coincided with many extreme values for various atmospheric circulation metrics. During November 2016 the SAM index defined by Marshall (2003) dropped to -3.12, this is the most negative value recorded since 1968 (Turner et al. 2017). This period was also a weak La Niña. La Niña

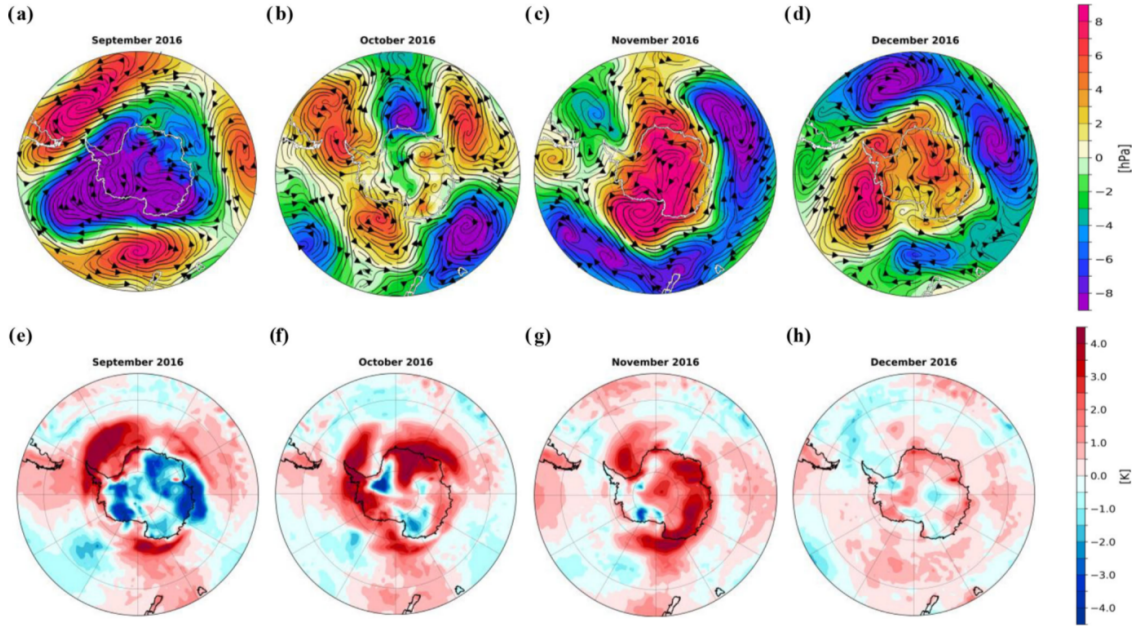

FIGURE 3.7: Sea level pressure anomalies and the associated wind streamlines (a–d) and 2m air temperature anomalies (e–h) from September until December 2016. The anomalies are computed relative to the reference period 1979–2010. Image and caption retrieved from Kusahara et al. (2018)

conditions force the SAM index to be more positive, suggesting that strong, local internal atmospheric variability caused the observed SAM anomaly (Stuecker et al. 2017). Record positive precipitation anomalies were also recorded in the Indian Ocean sector during the spring of 2016 (Meehl et al. 2019).

Doddridge and Marshall (2017) investigate the role of the anomalously negative SAM index during this event. The influence of SAM upon sea ice is discussed in detail in section 3.3.1. Doddridge and Marshall (2017) find that the Sea Surface Temperatures (SSTs) surrounding Antarctica were increased by the negative SAM anomaly and this contributed to the extreme sea ice retreat. Stuecker et al. (2017) add that the weak La Niña during 2016 enhanced the raise SST in the Southern Ocean. Model analysis by Kusahara et al. (2018) suggest that the majority of the 2016 SIE anomaly is attributable to thermodynamic surface forcing. Wind stress and ocean forcing also contributed, but at a smaller scale.

Wang et al. (2019) further investigate the role of tropical forcing on sea ice during this period. Wang et al. (2019) concludes that the weak La Niña coupled with a record negative Indian Ocean Dipole (IOD) provided heat anomalies that contributed to generating a strong wave-3 pattern at high latitudes. This wave-3 pattern forced the rapid sea ice retreat observed in September-October 2016. During

November-December, when the most rapid SIE decline occurred the major forcing was a weakening of the polar vortex due to the negative SAM (Doddridge and Marshall 2017). Wang et al. (2019) also concludes that the 2016 SIE anomalies were most likely a result of natural variability.

3.3 Attribution of SIC Increase

Sea ice is a result of the interaction of two dynamic systems, the ocean and the atmosphere, therefore the interactions of both systems must be considered when attempting to attribute observed changes in SIE (Hobbs et al. 2016). Recent work in search of an explanation for the observed trends has generally focused on changes within the marginal ice zone and areas of sea ice production such as polynyas.

3.3.1 Atmospheric drivers

Kohout et al. (2014) investigate the influence of storm-generated waves on the break-up of sea ice within the marginal ice zone. Wave amplitudes were found to propagate much further than previously thought. Waves with amplitudes greater than three meters were found to follow a linear decay rather than the exponential decay allowing these waves to penetrate hundreds of kilometres inwards from the marginal ice zone. This demonstrates the large role storm-driven waves play in the break-up and retreat of sea ice.

Roach et al. (2018) investigate the formation of pancake sea ice floes within the marginal ice zone during the sea ice advance period. Waves were observed to have a critical influence on the growth of pancake floes, with the maximum diameter of floes being restricted by wave tensile stress dependant on local wavelength and amplitude (Shen et al. 2001). The observed relationship between wave bending stress, and floe diameter by Roach et al. (2018), mirrors theoretical estimates made by Shen et al. (2001) and Shen (2004).

The atmosphere also influences sea ice on scales of larger spatial and temporal extent than weather. These influences are described by various modes of variability. Here we will discuss the influences of the SAM and the ASL, these modes have the largest influence on Southern Ocean sea ice (Hobbs et al. 2016).

Southern Annular Mode

The SAM describes the strength of the zonally symmetric meridional pressure gradient across the Southern Ocean. Since the 1960s a significant positive trend

has been observed in the SAM, with an increase mean in pressure observed north of 50° S and a decrease observed south of 60° S (Gong and Wang 1999; Kidson 1999; Marshall 2003; Thompson et al. 2000). This positive trend in the SAM, during the austral summer, is attributed to stratospheric ozone depletion that occurred in the latter half of the twentieth century (Armour and Bitz 2015; Polvani et al. 2011). Increasing SAM will force strengthening in the prevailing geostrophic westerly winds over the Southern Ocean. These strengthened zonal flows will, therefore, be expected to cause a positive meridional sea ice drift through the Coriolis effect, advecting ice away from the Antarctic coastline (Purich et al. 2016; Sen Gupta and England 2006). This northward advection would cause open water to become exposed at cold southern latitudes and therefore drive sea ice production. In contrast to this, Sigmond and Fyfe (2010), using a coupled climate model show that the opposite effect occurs, a strengthening SAM forces a decrease in Southern Ocean SIE.

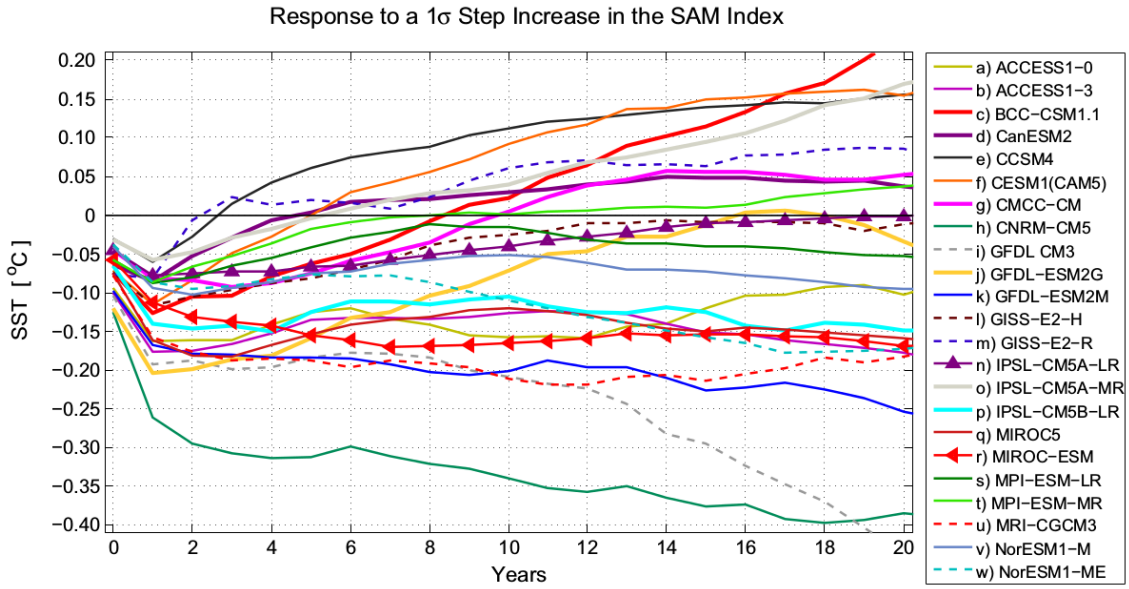

FIGURE 3.8: Annual-mean responses of the Southern Ocean SST [°C] to a step increase in the SAM index of magnitude 1σ across the CMIP5 ensemble. Image and caption retrieved from Kostov et al. (2017)

Ferreira et al. (2015) offer a potential explanation for this; ice production is reduced by the upwelling of warm circumpolar deepwater at the Antarctic coast, forced by the Ekman pumping mechanism. This process occurs over large timescales. Following a strengthening of the SAM, sea ice initially expands due to a northward transport of cool water across the Southern Ocean meridional SST gradient. Over larger timescales, the sea ice response reverses as upwelling of warm water raises SST and reduces the rate of sea ice production. Kostov et al.

(2017) also investigate this nonmonotomic temporal response to SAM, a 1σ step in SAM was applied to various model within the CMIP5. The SST response to this shift varied between models. Some models demonstrated a reversed, warming response as soon as 2 years after the step increase, while other models did not show a reversal and the initial cooling of SST within the Southern Ocean persisted (Figure 3.8). Analysis by Doddridge and Marshall (2017) also support a short-timescale cooling response to increases in the SAM.

Amundsen Sea Low

Another important mode of variability within the atmosphere over the Southern Ocean that has been found to have an influence on sea ice formation is the ASL[5]. This describes the strength and position of a persistent low-pressure anomaly over the Amundsen Sea (60°-70° S, 100°-140° W) (Baines and Fraedrich 1989; Raphael et al. 2016; Turner et al. 2013c). While the ASL is closely linked to the SAM, the cyclonic flow driven by this feature has a unique influence on sea ice production around West Antarctica. The ASL is described by three variables: ASL intensity (ASLp), which is defined as the relative central pressure; ASL longitude (ASLx), and ASL latitude (ASLy) which describe the position of the low-pressure system (Coggins and McDonald 2015). Over the 1979-2008 period Turner et al. (2013c) report the ASLp deepened at a rate of 1.7 hPa dec^{-1}. This trend is consistent with the strong trend observed in the SAM, with lower pressures observed at southern latitudes (Marshall 2003).

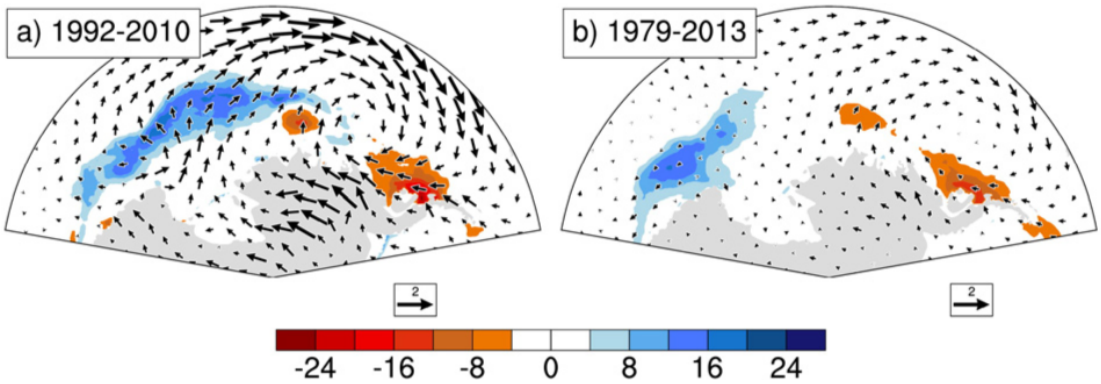

FIGURE 3.9: April-June seasonal mean trends in SIC (%/decade) and ERA-Interim 10 m winds (ms^{-1}/decade) for the analysis period of (Holland and Kwok 2012), compared to the full passive microwave period. Image sourced from Hobbs et al. (2016).

[5]The Amundsen Sea Low is sometimes referred to as the Amundsen-Bellingshausen Sea low (Fogt et al. 2012)

The cyclonic flows associated with the strengthening ASLp drives warm air from the Southern Ocean poleward over the Antarctic Peninsula and the Bellingshausen Sea, while cold air is drawn northwards from the Antarctic interior towards the Ross Sea. These meridional flows have a much stronger influence on sea ice formation compared to the zonal flows associated with the SAM (Hobbs and Raphael 2010; Holland and Kwok 2012; Raphael 2007). Strengthening of the ASLp will reduce sea ice production in the Bellingshausen Sea, and increase sea ice production in the Ross Sea through increased meridional advection and heat transport (Holland and Kwok 2012; Hosking et al. 2013; Turner et al. 2015, 2016).

Figure 3.9 shows the long term trends in winter SIC and ERA-Interim 10 m wind vectors within the Ross, Amundsen, and Bellingshausen Seas, for two time periods. Both time periods show strengthening in cyclonic winds representative of a deepening of the ASL. The dipole pattern in the SIC fields are consistent with the increasing meridional wind speeds over these periods (Hosking et al. 2013). Stronger trends wind speeds over the Ross Sea were observed over the 1992-2010 period (figure 3.9a) than the 1979-2013 period (figure 3.9b). This is somewhat due to an eastern shift of the ASLx over the longer period (Coggins and McDonald 2015). Despite the weaker meridional wind trend over the western Ross Sea, a strong, positive trend in SIC is still observed in this region. This suggests that this trend in the western Ross Sea is not influenced by the ASL and is driven by other, local factors (Haumann et al. 2014).

Snowfall upon sea ice

A layer of snow that often forms upon the ice pack effects the production and maintenance of sea ice, however, this effect is complex and non-linear. Snow has a thermal conductivity an order of magnitude lower than that of sea ice (Maykut and Untersteiner 1971; Sturm and Massom 2009). This inhibits heat flux from the ocean to the atmosphere and reduces the rate of sea ice production during the winter. Snow also has an albedo lower than that of sea ice. When paired with the low thermal conductivity of snow, the amount of sea ice melt that occurs during summer is reduced by the presence of a snow layer. A secondary effect of snow forming upon the sea ice is that the weight of the snow layer reduces the free-board of the sea ice (Eicken et al. 1995). In extreme cases this can cause the entire layer of sea ice to become submerged, which then forms a layer of slush that eventually freezes, contributing to sea ice production (Maksym and Markus 2008).

3.3.2 Ocean feedbacks on sea ice extent

Zhang (2007) presents a feedback mechanism which would allow increased SIE to occur as a result of increasing surface temperatures. During the autumn sea ice advance, the production of sea ice causes brine rejection, this dense, high-salinity water falls through the ocean column and causes mixing in the otherwise stratified ocean (Zhang 2007). Decreasing the volume of brine rejected in the autumn will increase the stratification of this upper layer and prevent entrainment of warm AABW. This causes a negative feedback between autumn ice production and SIE in the following summer. This feedback requires the surface heating that caused the deficit in autumn sea ice growth to be less than the vertical heat flux of entrainment. Martinson (1990) show that this condition occurs in several regions around Antarctica.

Goosse et al. (2009) and Goosse and Zunz (2014) suggest that an alternate, positive feedback in sea ice production occurs. Brine rejection causes an annual net downward transport of salt. This increases stratification of the ocean column as buoyant freshwater lies above dense rejected brine, preventing vertical heat transport and lowering the SST. This feedback contrasts with the Zhang (2007) process as it operates on a multi-year time scale.

3.3.3 Influence of ice shelf and ice sheet melt

Many authors have focused their effort on the hypothesis that freshwater introduced into the Southern Ocean by melting Antarctic ice shelves and ice sheets could lead to the increase in SIE observed over the satellite period (Bintanja et al. 2015, 2013; Pauling et al. 2016, 2017; Swart and Fyfe 2013). The introduced freshwater near the surface could form a buoyant layer and increase stratification of the water column preventing vertical heat flux.

Rye et al. (2014) estimate the total freshwater flux due to melt of grounded ice and ice shelves within Antarctica to be $350 \pm 100\,\mathrm{Gt\,yr^{-1}}$. Using the EC-Earth model Bintanja et al. (2013) and Bintanja et al. (2015) were able to demonstrate positive trends in Antarctic SIE when constant freshwater inputs of $250\,\mathrm{Gt\,yr^{-1}}$ and $120\,\mathrm{Gt\,yr^{-1}}$ were applied respectively. In contrast, Swart and Fyfe (2013) was unable to produce a positive trend when a linearly increasing freshwater input ranging from 0 to $890\,\mathrm{Gt\,yr^{-1}}$ over a 29 year period was added to the University of Victoria-Earth System Climate Model. Furthermore Pauling et al. (2016) found no significant change in trend of sea ice area when freshwater fluxes up to $3000\,\mathrm{Gt\,yr^{-1}}$ were applied to the Community Earth System Model version 1 and

the Community Atmosphere Model version 5. Pauling et al. (2016) also investigated the effect of introducing freshwater at various depths through the ocean column and found that there was little relation between the depth of introduction and the resultant forcing upon sea ice.

Although freshwater input may have caused a slight increase in SIE in some regions, freshwater input is unlikely to have altered SIE within the Southern Hemisphere (Hobbs et al. 2016).

3.4 The Ross Sea Polynya

The topic of this thesis is the interactions of the atmosphere and the cryosphere within the Ross Sea. A particular focus is the atmosphere-ocean-sea ice interactions that occur within the Ross Sea Polynya (RSP). SIE anomalies within the Ross Sea are primarily responsible for the positive SIE trend observed around Antarctica over recent decades (Table 3.1) (Turner et al. 2015). The Ross Sea also has a positive net sea ice export, contributing to SIE trends in neighbouring sectors (Drucker et al. 2011). Drucker et al. (2011) estimates that between 20%-50% of the sea ice production within the Ross Sea occurs within polynyas. Three major polynyas regularly reside within the Ross Sea: the Terra Nova Polynya, the McMurdo Sound Polynya, and the Ross Sea Polynya (Figure 3.10). The latter is the largest regularly forming polynya on Earth and provides over twice the rate of sea ice production of any other polynya (Tamura and Ohshima 2008).

The formation of the Ross Sea polynya is primarily driven by advection of sea ice due to local wind stress (Nakata et al. 2015; Reddy et al. 2007). Ocean currents also provide a SIC forcing, at a lesser magnitude to that of wind stress. This forcing is stronger in the western Ross Sea and results in the asymmetric shape of the RSP (Nakata et al. 2015). Bromwich et al. (1998) finds that 25% of the SIC variance within the RSP is related to wind and temperature variations observed at the nearby Ferrell Automatic Weather Station (AWS).

Holland and Kwok (2012) investigates how trends in wind vectors over the Southern Ocean affect sea ice drift. Between 1992-2010 statistically significant trends in sea ice drift were observed in many sectors. Over this period, northward sea ice export increased by $2\,\mathrm{cm\,s^{-1}}$ in the Ross Sea (Holland and Kwok 2012). While significant correlations were found between the sea ice drift trend and the 10 m wind vector trend over much of Antarctica. The southward wind vector trend in the western Ross Sea opposed the northward sea ice drift trend (Holland and Kwok 2012).

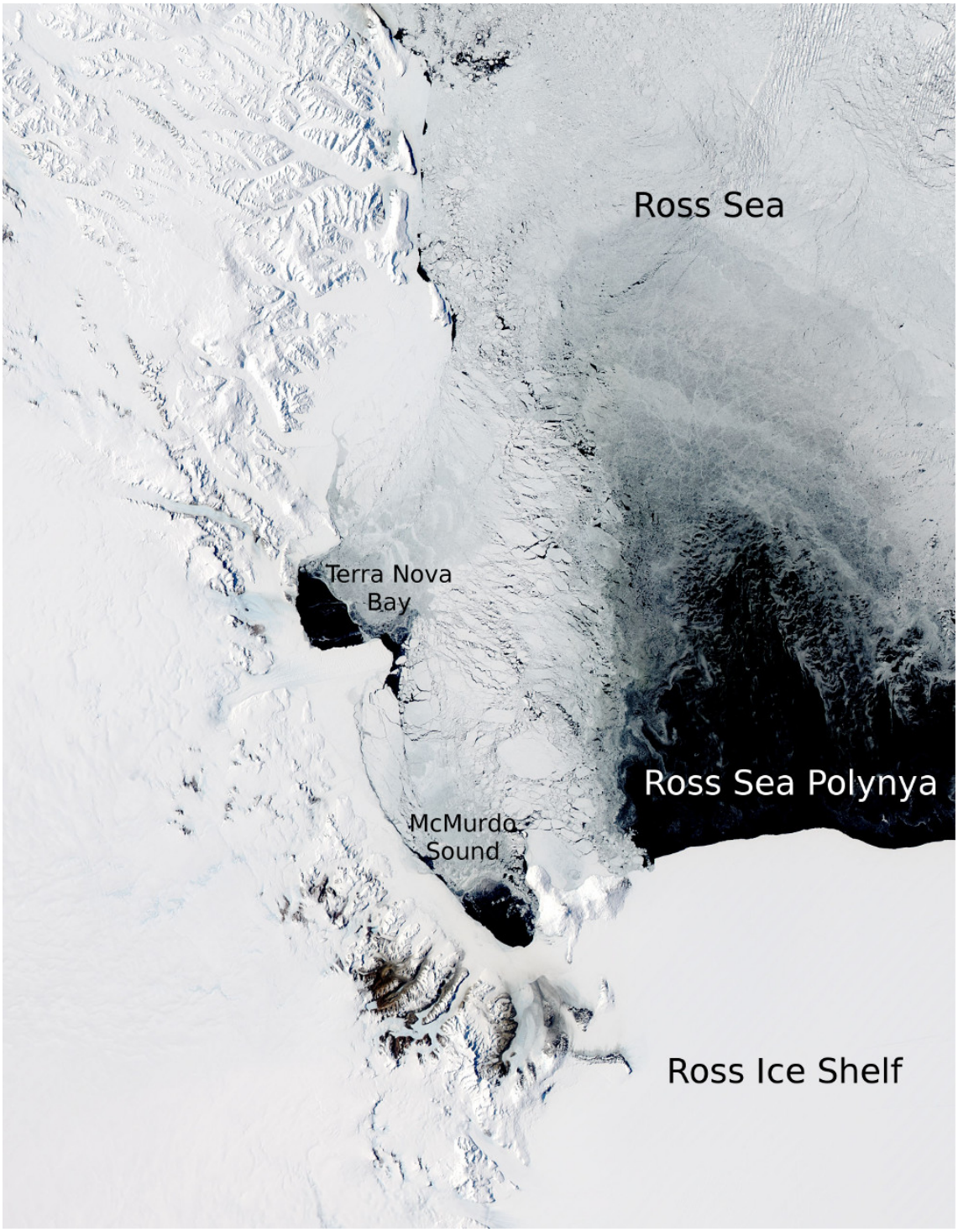

FIGURE 3.10: Natural colour image of the south-western Ross Sea taken by the Aqua satellite on 16th November 2011. The Terra Nova bay, McMurdo Sound and Ross Sea Polynyas can be seen. Image retrieved from www.earthobservatory.nasa.gov/images/76474/polynya-off-the-antarctic-coast.

Wind-driven advection of sea ice away from the Antarctic coastline leaves an

area of open water that will quickly freeze during winter months. Air temperatures over the Ross sea rarely rise above freezing during the austral winter, the water below the sea ice is consistently at the freezing point for seawater ~-1.8° C (Tamura and Ohshima 2008). The exposed open water within the polynya readily freezes into frazil ice. This unconsolidated ice is rapidly advected northwards by the prevailing offshore winds towards consolidated ice at the northern border of the RSP (Nakata et al. 2015). This process causes the production of large volumes of sea ice when offshore winds flow over the RSP. Chapter 4 investigates how the RSP and sea ice within the Ross Sea respond to strong wind events.

The open polynya also allows upward heat flux into the atmosphere from the exposed warm seawater (Bromwich et al. 1998). Chapter 5 presents Controlled Meteorological (CMET) balloon observations in the vicinity of the RSP and investigates the effect of heat flux from the RSP on the atmosphere and its representation within the Antarctic Mesoscale Prediction System (AMPS) forecast model.

Chapter 4

Atmospheric Forcing of Sea Ice Anomalies in the Ross Sea Polynya Region

This chapter was initially published as a standalone journal article in *The Cryosphere*:

Ethan R. Dale et al. (Jan. 2017). "Atmospheric forcing of sea ice anomalies in the Ross Sea polynya region". In: *Cryosphere* 11.1, pp. 267–280. DOI: 10.5194/tc-11-267-2017

Abstract

We investigate the impacts of strong wind events on the sea ice concentration within the Ross Sea Polynya (RSP), which may have consequences on sea ice formation. Bootstrap sea ice concentration (SIC) measurements derived from satellite SSM/I brightness temperatures are correlated with surface winds and temperatures from Ross Ice Shelf (RIS) Automatic Weather Stations (AWSs) and weather models (ERA-Interim). Daily data in the austral winter period were used to classify characteristic weather regimes based on the percentiles of wind speed. For each regime a composite of a SIC anomaly was formed for the entire Ross Sea region and we found that persistent weak winds near the edge of the Ross Ice Shelf are generally associated with positive SIC anomalies in the RSP and vice versa. By analysing sea ice motion vectors derived from the SSM/I brightness temperatures we find significant sea ice motion anomalies throughout the Ross Sea during strong wind events, which persist for several days after a strong wind event has ended. Strong, negative correlations are found between SIC and AWS wind speed within the RSP indicating that strong winds cause significant advection of sea ice in the region. We were able to partially recreate these correlations using co-located, modeled ERA-Interim wind speeds. However, large AWS and model differences are observed in the vicinity of Ross Island, where ERA-Interim underestimates wind speeds by a factor of 1.7 resulting in a significant misrepresentation of RSP processes in this area based on model data. Thus, the cross-correlation functions produced by compositing based on ERA-Interim wind speeds differed significantly from those produced with AWS wind speeds. In general the rapid decrease in SIC during a strong wind event is followed by a more gradual recovery in SIC. The SIC recovery continues over a time period greater than the average persistence of strong wind events and sea ice motion anomalies. This suggests that sea ice recovery occurs through thermodynamic rather than dynamic processes.

4.1 Introduction

Throughout the satellite observation era the total winter sea ice cover in the Southern Ocean has followed a well established increasing trend, a process that is mainly driven by significant sea ice expansion in the Ross Sea (Comiso and Nishio 2008; Holland 2014; Turner et al. 2009, 2015). However, there is still uncertainty about the mechanisms that have driven this change. The central aim of this work is to study how the variability of strong southerly winds over the western Ross Ice Shelf impacts sea ice concentration (SIC) in the region near the Ross Sea Polynya (RSP). A polynya is an area of open water or decreased SIC surrounded by either concentrated sea ice or land ice. Due to the increased ocean-to-atmosphere heat flux within these regions, polynyas are areas of high sea ice production (Tamura and Ohshima 2008). The RSP is a large polynya that regularly forms near the northwestern edge of the Ross Ice Shelf as a result of persistent offshore winds.

This work builds on previous studies, such as those by Bromwich et al. (1998), Comiso et al. (2011), Drucker et al. (2011), Holland and Kwok (2012), Kwok et al. (2007), Reddy et al. (2007), and Turner et al. (2015), who have shown that the Ross Sea polynya and the related atmospheric forcing plays an important role in sea ice production. For example, Drucker et al. (2011) estimate that 20–50 % of the sea ice production in the Ross Sea occurs in the RSP and that the increase in sea ice extent in the Ross Sea region is related to the changes in wind forcing. Bromwich et al. (1998) compare Automatic Weather Station (AWS) wind speeds and temperatures with SIC derived from Special Sensor Microwave/Imager (SSM/I) data within the RSP. Bromwich et al. (1998) found that 25 % of SIC variance within the RSP can be explained by wind and temperature variations observed at Ferrell AWS.

Coastal polynyas, such as the RSP, are driven by sea ice export from the coast, with sea ice drift being controlled by both oceanographic and atmospheric forcings. Ice in free drift will have a velocity equal to that of the local ocean current plus some component due to the effect of wind stress (Holland and Kwok 2012). This wind component will fall to the left of the wind vector in the Southern Hemisphere and has a magnitude of up to about 2 % of the local wind speed (Brümmer et al. 2008). In consolidated ice, internal stresses will oppose the geostrophic wind and therefore decrease ice drift velocity (Brümmer and Hoeber 1999). Holland and Kwok (2012) used sea ice motion data and reanalysis wind fields to show that wind-driven changes in ice advection are the dominant drivers of SIC trends around much of West Antarctica. Also, wind-driven thermodynamic changes

play a large role in coastal regions of the Atlantic sector (Kong Håkon VII Sea) where autumn SIC trends oppose the near-surface wind variations.

As sea ice production occurs within the RSP brine, rejection occurs, forming negatively buoyant, dense water. This leads to the formation of Antarctic bottom Water (AABW) (Whitworth and Orsi 2006). AABW formation is suggested as a major sink for CO_2 and heat and is a driver of global ocean circulations (Ohshima et al. 2013). A change in the rate of sea ice production within the RSP and therefore the rate of AABW production could have significant effect on the global ocean circulation.

Previous studies were constrained by a lack of detailed meteorological measurements. The weather patterns over the Ross Sea contain many small-scale features that are governed by the topography of the area. Thus, current models such as the Antarctic Mesoscale Prediction System (AMPS; Powers et al. 2012) are unable to resolve many of these features (Coggins et al. 2013; Jolly et al. 2016). This means that understanding the direct influence of strong winds on the formation of the RSP, a region of major sea ice production, has been limited. The analysis of the seasonal patterns of Antarctic sea ice growth and decline and its interannual variability is complicated by the fact that they depend on a number of atmospheric and oceanic forcings that occur at a wide range of timescales. In particular, SIC is influenced by both atmospheric and oceanic factors, including the strength of near-surface winds, air temperature, ocean currents, ocean temperature and salinity of the ocean (Bintanja et al. 2013; Holland 2014; Holland and Kwok 2012; Turner et al. 2015).

The primary synoptic-scale atmospheric variations affecting sea ice include the overall magnitude of the geostrophic wind (Sen Gupta and England 2006), the localised zonal and meridional wind anomalies (Holland and Kwok 2012; Kwok 2002; Sen Gupta and England 2006; Stammerjohn et al. 2008; Turner et al. 2009), surface air temperature anomalies (Kwok 2002; Sen Gupta and England 2006), and variations in energy fluxes between the atmosphere–ocean–sea ice systems. Geostrophic winds are also central to describing the variations in localised Ekman transport patterns within the ocean. Specifically, (Stammerjohn et al. 2008) identified that enhanced Westerlies throughout the 1990s in the western Ross Sea caused a more persistent northward Ekman sea ice drift, which affected the seasonal ice extent of the region by causing earlier ice advance and later ice retreat.

In this study, we investigate winter in situ measurements from weather stations directly upwind of the Ross Sea polynya in relation to satellite measurements of sea ice cover in order to better understand the timescales over which surface wind

impacts on sea ice drift and potential sea ice formation. We do this in comparison with winds from a low-resolution reanalysis model (ERA–Interim. Dee et al. 2011) in order to find out to what extent simulated wind fields in the region can reproduce the statistical relationship and dependence between weather and sea ice anomalies. This work therefore has a wider relevance given that atmospheric circulation changes in the Ross Sea may explain a significant portion of the climate variation in the region and particularly increases in sea ice extent and the northward drift of sea ice (Holland and Kwok 2012; Nicolas and Bromwich 2014).

4.2 Data and methods

We utilise both basic bootstrap algorithm and AMSR-E bootstrap algorithm SIC data (henceforth "bootstrap" collectively) provided by the National Snow and Ice Data Centre (NSIDC) (Comiso 2000; Maslanik and Stroeve 2004). Bootstrap SIC is available on a daily basis sampled on a 25km by 25km grid since 1987 and every other day prior to this date (starting in 1978). Daily averages of SIC swath data are provided by NSIDC; these were assumed to be centred around midday with measurement spread 12 h before and after the reported time. We obtain 2 m wind speed and 2 m temperature data measured at the Laurie II automatic weather station (AWS), located at 77.52° S, 170.81° E, provided by the University of Wisconsin-Madison Automatic Weather Station Program detailed in Lazzara et al. (2012). The Laurie II station has been providing data at 10 min temporal resolution since February 2000. In this study we focus on output from the Laurie II station because of its long continuous record and proximity to the RSP. The analysis presented has also been completed for a number of other stations, including Vito, Emilia, and Ferrell stations, and these results remain rather similar.

Figure 4.1 shows the standard deviation of SIC, calculated from the daily variation from the long-term winter mean of bootstrap SIC data over the period 20 April until the 1 November for the years 1979 until 2014. This period was chosen to exclude the annual break out of sea ice to minimise variability not associated with day-to-day polynya activity. Coastal pixels often display a large variability, for example the area longitude 170°and 180° E extending several hundred kilometres offshore. The orientation of this area corresponds well with both the dominant wind directions observed at the Laurie II AWS site and the location of the RSP as identified in Nakata et al. (2015) amongst others. Large deviations from the mean are due to the high variability in SIC within the polynya, as displayed in figure 4.2.

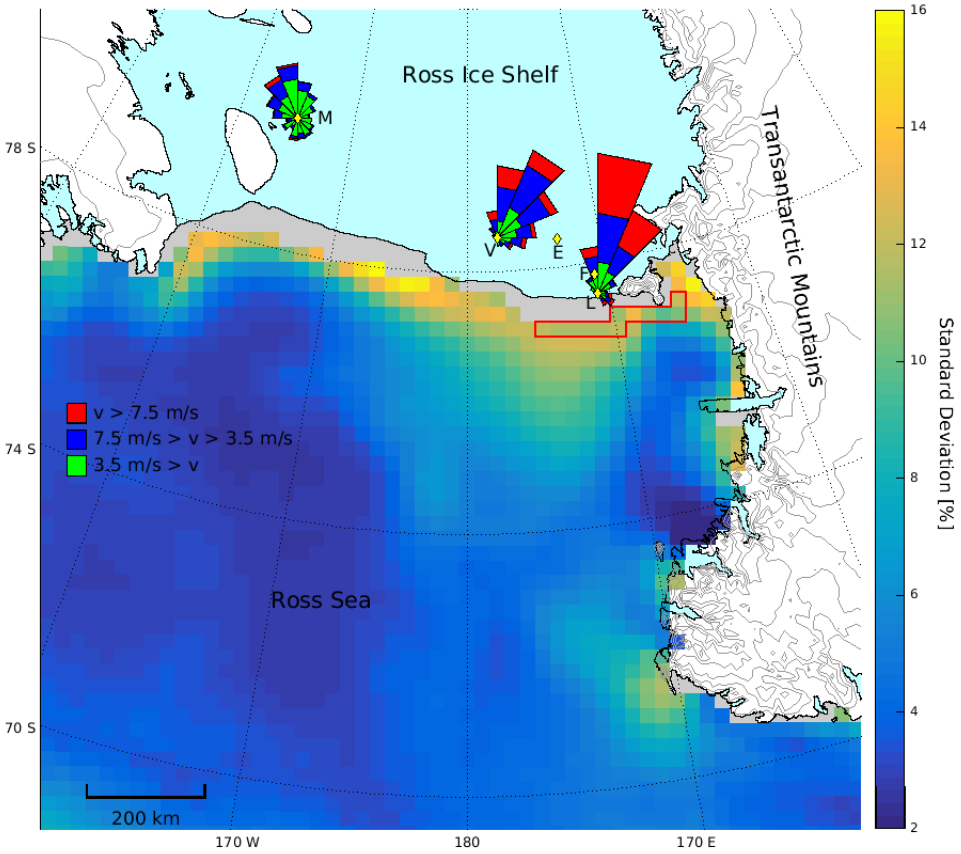

FIGURE 4.1: Map of Ross Sea region, grey contour lines indicate topography at 500 m intervals (Liu et al. 2001). The colour scale indicates the standard deviation of bootstrap SIC for 20 April–1 November 1979–2014. Yellow diamonds indicate the positions of Margaret, Vito, Emilia, Ferrell, and Laurie II AWS sites, labelled M, V, E, F, and L, respectively. Wind roses for Margaret, Vito, and Laurie II are included. The green, blue, and red colours indicate the low, medium, and high wind speeds based on the 33rd and 66th percentile wind speeds (3.5 and 7.5 ms^{-1}) as measured at Laurie II. The red line outline indicates the region discussed in section 4.2.

For our analysis we define a region comprised of pixels adjacent to the bootstrap land mask and 10°wide in longitude centred on the Laurie II AWS site, identified in red in figure 4.1. This gives a 25 km by 250 km region close to the Ross Ice Shelf and Ross Island, co-located within the area where the Ross Sea polynya can be observed. The wind roses in figure 4.1 display the distribution of wind vectors observed at various AWS sites (Margaret, Vito, and Laurie II).

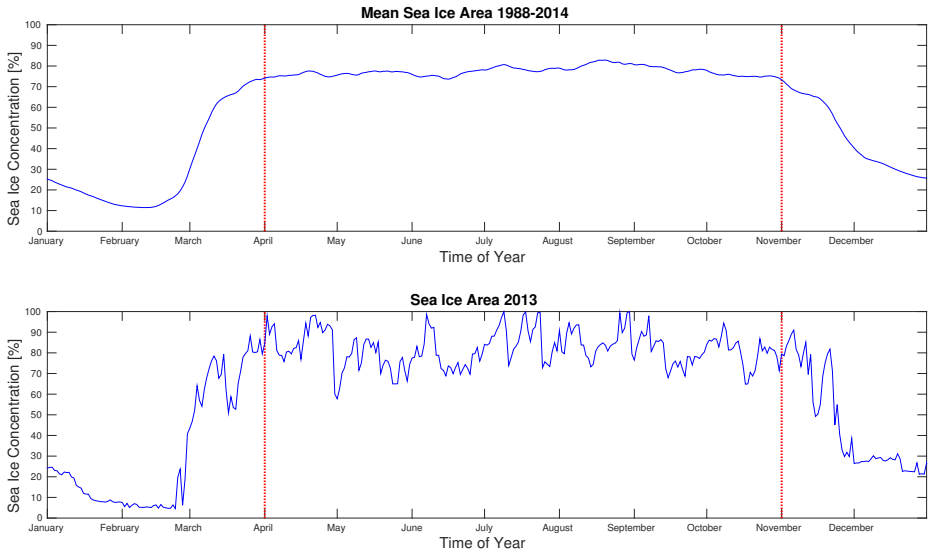

FIGURE 4.2: (**a**) Mean SIC within RSP north of the Laurie AWS from the region identified in figure 4.1. (**b**) SIC during 2013, highlighting day-to-day variability. Red dotted lines identify the period from April to October used in this study.

We derive sea ice motion vectors from the National Snow and Ice Data Center's 12.5 km resolution polar stereographic gridded brightness temperatures, retrieved from the Special Sensor Microwave/Imager (SSM/I) and Special Sensor Microwave/Imager Sounder (SSM/IS) instruments (Maslanik and Stroeve 2004). Daily averages are available from July 1987 to December 2015. We utilise the vertical and horizontal polarizations of the 85.5 GHz channel from 1987 to 2009 and the 91.7 GHz channel from 2010 onwards.

Following multiple authors (Emery et al. 1997; Heil et al. 2006; Holland and Kwok 2012), we estimate ice motion via a maximum cross-correlation method. We track 9×9 grids of stereographic cells (112.5×112.5 km) over a radius of eight grid cells (100 km). The search radius provides an upper limit for ice velocity of approximately $1.2\,\mathrm{ms}^{-1}$, defining a physically plausible range (Heil et al. 2006).

The cross-correlation method proceeds by comparing consecutive daily averages of brightness temperature data. For each day, brightness temperatures in a particular grid are correlated against those in the surrounding grids on the subsequent day. The sea ice is assumed to have moved to the grid with the highest correlation. A correlation threshold of 0.7 was chosen to limit erroneous designations. Our method uses the maximum correlation from both the horizontal and vertical polarizations. From the resulting displacement and time period the ice velocity was estimated.We subsequently smoothed the gridded velocities to a 25 km

stereographic grid.

Using this simple method, fast small-scale motions as well as rotations and divergence of the ice pack are not resolved. Furthermore, motion in coastal areas is likely to be less accurate due to the difficulties in applying the method to incomplete grids. Brightness temperature-derived motions are considered inaccurate outside of the winter season due to surface melt and high levels of atmospheric water vapour (Emery et al. 1997; Holland and Kwok 2012). Hence, we restrict our analysis of sea ice motions to the cold months of April to October.

We compare winds observed at the AWS sites with 10m winds of the ERA-interim meteorological reanalysis model (Dee et al. 2011). The model output is available on a $0.75^\circ \times 0.75^\circ$grid at a 6 h temporal resolution running from late 1979 until present. Although AMPS provides higher-resolution weather data, ERA-Interim was used due to its temporal consistency and data set spanning the AWS period. ERA-Interim does not assimilate wind speed measurements over land (including ice shelves) and is therefore independent from AWS measurements. For comparison of AWS and ERA-Interim wind data, virtual AWSs were created by interpolating the wind speed from the ERA-Interim grid to the location of the AWS sites using a bilinear interpolation.

4.3 Results

4.3.1 SIC within the Ross Sea polynya

Figure 4.2 shows the mean SIC within the coastal area identified in figure 4.1 averaged over the period 1988 to 2014. Throughout the winter period, defined between 1st April and 1st November in this study, the total SIC within this area is relatively constant. Outside this period we observe a gradual decrease in SIC from November until a minimum is reached in mid-February, followed by a more rapid increase in SIC in early March. For the remainder of this analysis we will only consider the period from April to October to remove the effects of summer melt and to avoid periods with low SIC and large gradients in SIC. Figure 4.2b shows the daily SIC for the same area derived from data in 2013 to show the high degree of variability in the SIC in this region; these results resemble a previous analysis reported in Bromwich et al. (1998). The large day-to-day variability between April and October (Figure 4.2b) is likely to be associated with polynya processes. The sawtooth features observed in this specific year, for example around 1 May, are common features and illustrate that decreases in SIC generally occur

more rapidly than the following increases in SIC, a point that will be supported by later analysis.

4.3.2 Inter-comparison of AWS and ERA-Interim wind speeds

The wind climatology of the region, derived from AWS data, is represented by wind roses in figure 4.1. Wind roses are angular histograms indicating prevailing winds; the colours indicate the distribution of wind speed in each angular sector. Inspection of the wind rose closest to Ross Island (Laurie II) shows that the wind in this region is dominated by strong southerly flows. These strong southerly flows are also an important feature of the wind distribution at the other AWS sites displayed in figure 4.1 but are not observed as frequently. However, as identified previously, the results presented do not change appreciably if data from other AWS sites in the northwestern corner of the Ross Ice Shelf are utilised.

The wind speeds measured at four AWSs, Laurie II, Ferrell, Emilia, and Vito, were compared to the virtual sites interpolated from the ERA-Interim model grid. Scalar wind speeds at Laurie II, Ferrell, and Emilia correlated well with $R^2 > 0.75$, while Vito was found to have a weaker correlation of $R^2 = 0.55$. Inspection of ERA-Interim and AWS wind roses revealed no significant directional bias between the two data sets. However, when linear least square fits between the model and the Laurie and Ferrell AWS winds were applied, slopes of 1.70 and 1.52, respectively, were found, indicating that at these sites ERA-Interim generates significantly weaker wind speeds than measured by the AWS. Scale factors measured at Emilia and Vito were 1.06 and 0.96, respectively, indicating a better agreement between the AWS and ERA-Interim wind speeds at these sites. Laurie and Ferrell are located 36 km and 57 km from Cape Crozier (at the eastern end of Ross Island), while Emilia and Vito lie 140 km and 223 km east of Ross Island. Thus, the differences observed are likely linked to the local topography that is not well represented in the ERA-Interim reanalysis. Recent work by Jolly et al. (2016) comparing AWS observations with the Antarctic Mesoscale Prediction System output (a much higher-resolution atmospheric model) also identifies that the effect of topography in the region can not be reproduced by the model (Powers et al. 2012). It should also be noted that ERA-Interim does not assimilate wind speed measurements over land and so the two data sets are independent (Dee et al. 2011).

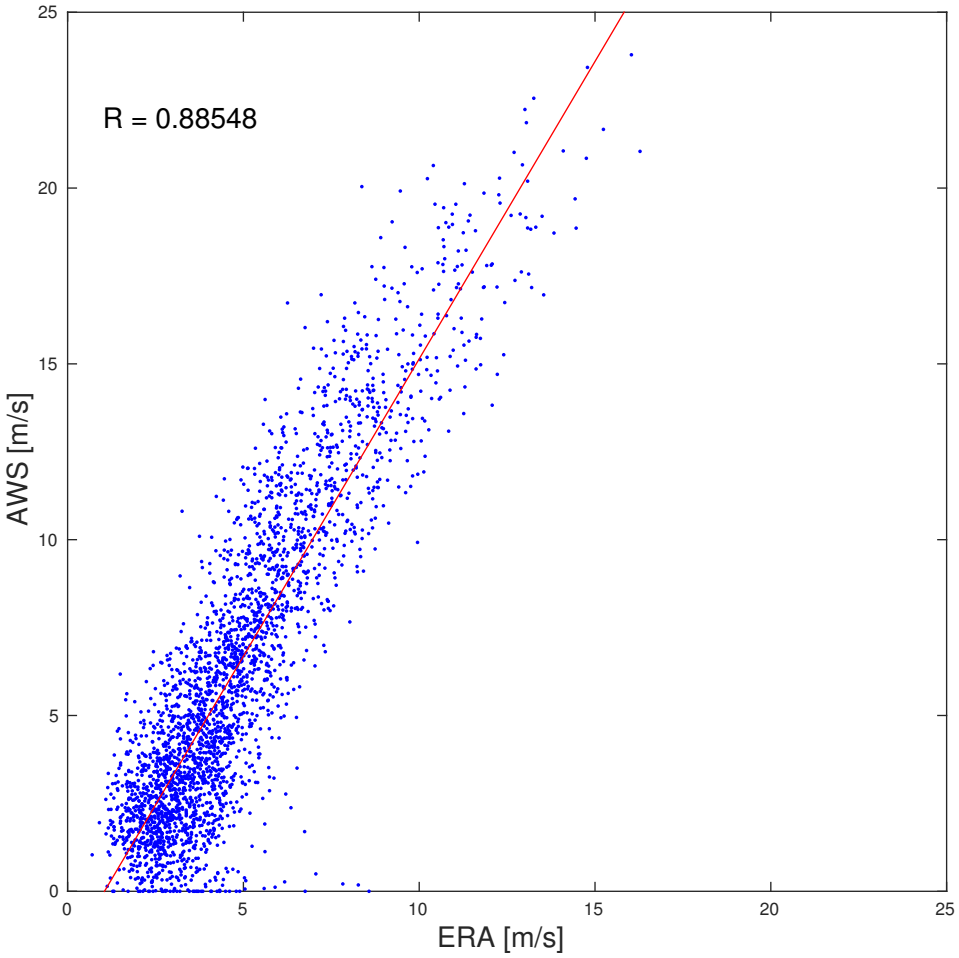

FIGURE 4.3: Scatter plot of 24 h mean wind speed for winter 2000-2014, measured by Laurie II AWS against that of ERA-Interim. The red line indicates the linear least squares fit.

4.3.3 Correlations between SIC and AWS measurements

Cross-correlation functions (CCFs) between the time series of SIC within the region in figure 4.1 and both wind speeds and temperatures measured at the Laurie II AWS site were calculated for the 2000-2014 period. For comparison with daily bootstrap SIC data, 24 h running means of the 10 min AWS measurements were used. Although SIC data were only available on a 24 h resolution, wind data were available at a 10 min resolution. By varying the time lag between these two time series and calculating the Pearson correlation coefficient for each lag, CCFs were able to be calculated at a 10 min time resolution. The bootstrap SIC is derived from 24 h binned brightness temperatures and we compared these with the 24 h rolling mean of AWS data. The resulting correlation functions will be blurred

over a 24 h period. The CCF between the time series of SIC and both scalar wind speeds and temperatures measured at the Laurie II AWS site are shown in figure 4.4.

In figure 4.4a we find a strong negative correlation between SIC and wind speed, with the maximum magnitude correlation occurring after a 12 h time lag. The minimum is preceded by a rapid decrease and followed by a more gradual increase in correlation with respective *e*-folding times of -48 and 100 h. This indicates that during high-wind events the SIC in the RSP area is generally low. The difference in the decrease and increase *e*-folding times suggests that the two changes are controlled by different processes. For example, we expect that the decrease in SIC is dominated by more rapid northward advection, while the increase in SIC during sea ice formation is dominated by slower ice formation. This interpretation is supported by the recent analysis detailed in (Nakata et al. 2015), which used a simplified model to understand polynya changes.

Laurie II is located about 50km south of the region used for the SIC analysis. A change of predominantly southerly winds (Parish and Bromwich 2007) is first observed upwind at Laurie II before the signal propagates to the RSP downwind. Wind blowing at $5ms^{-1}$ would take about 3 h to travel the distance, meaning the 12 h delay observed cannot be entirely explained by this process. Another contributing factor is that the region used for calculating the SIC is not directly adjacent to the northern edge of the RIS and an area of sea ice may exist south of the studied polynya area. If a northward advection of sea ice occurs, the ice advected from the region will be replaced by ice in the unobserved region between the Ross Ice Shelf and the region specified in figure 4.1. This could allow advection of sea ice to occur for a short period of time without a decrease in SIC occurring, causing the minimum in sea ice to occur several hours after a significant increase in wind speed. In addition, as a strong wind event progresses, the sea ice will ridge and raft upon itself, causing the surface roughness of the ice to increase.We speculate that this will make the ice slightly more susceptible to the wind stress (Mårtensson et al. 2012). As the SIC decreases, internal stresses prohibiting motion will decrease, allowing advection to become more significant. These effects will cause the minimum SIC to occur slightly after the time of maximum wind speed and are likely causes of the location of the minimum correlation between SIC and wind occurring at approximately a 12 h delay, though the collection of swath data also introduces some uncertainty in the exact timing. Wind speeds in the area autocorrelate with an e-folding time of 36 h (figure 4.4a), which explains the significant correlations in the CCF between AWS wind speed and SIC

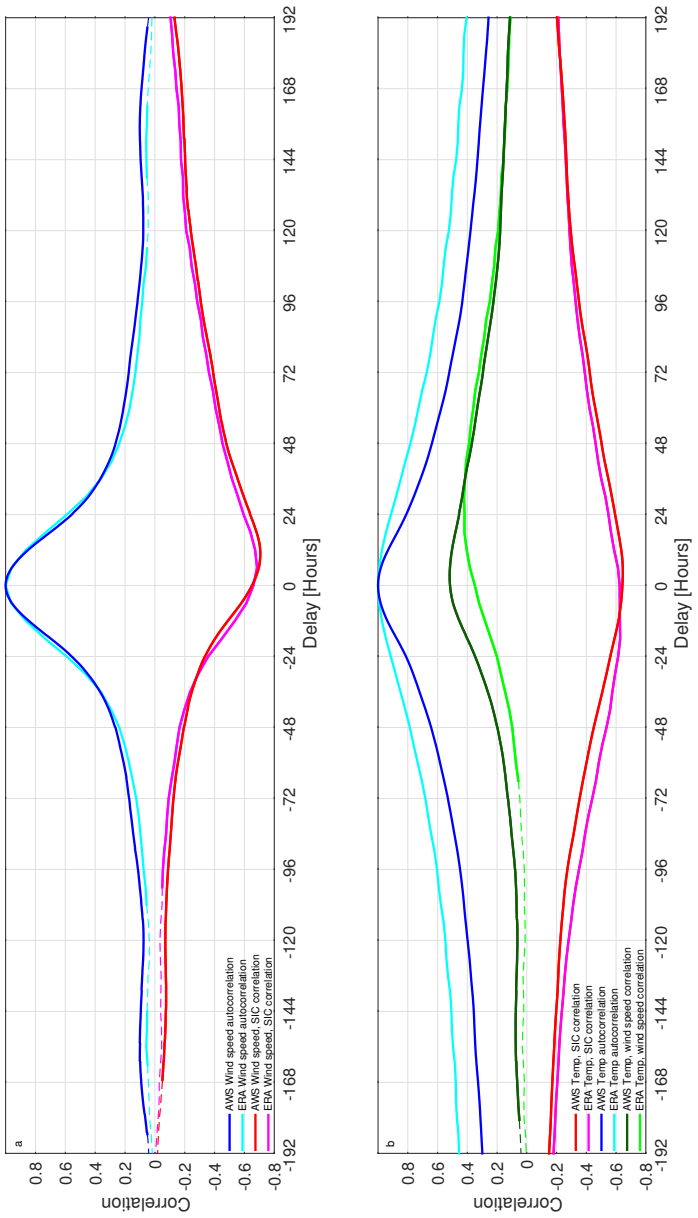

FIGURE 4.4: (**a**) Cross-correlation curve for sea ice concentration and AWS (red) and ERA-Interim (magenta) wind speeds and autocorrelation curve for wind speed at Laurie II AWS (blue) and ERA-Interim (cyan). (**b**) Cross-correlation curve for sea ice concentration and temperature for AWS (red) and ERA-Interim (magenta); autocorrelation curves for wind speed at Laurie II AWS site (blue) and ERA-Interim (cyan) are also shown. Cross correlation for wind speed and temperature measured at Laurie II AWS (dark green) and ERA-Interim (light green). Dashed lines indicate significance $p > 0.01$. The delay is defined such that positive values indicate meteorology measures leading SIC.

at negative delay. The *e*-folding time for the decrease in this CCF is −48 h and the extrema occurs at a delay of 12 h corresponding with the 36 h *e*-folding time for AWS wind speeds.

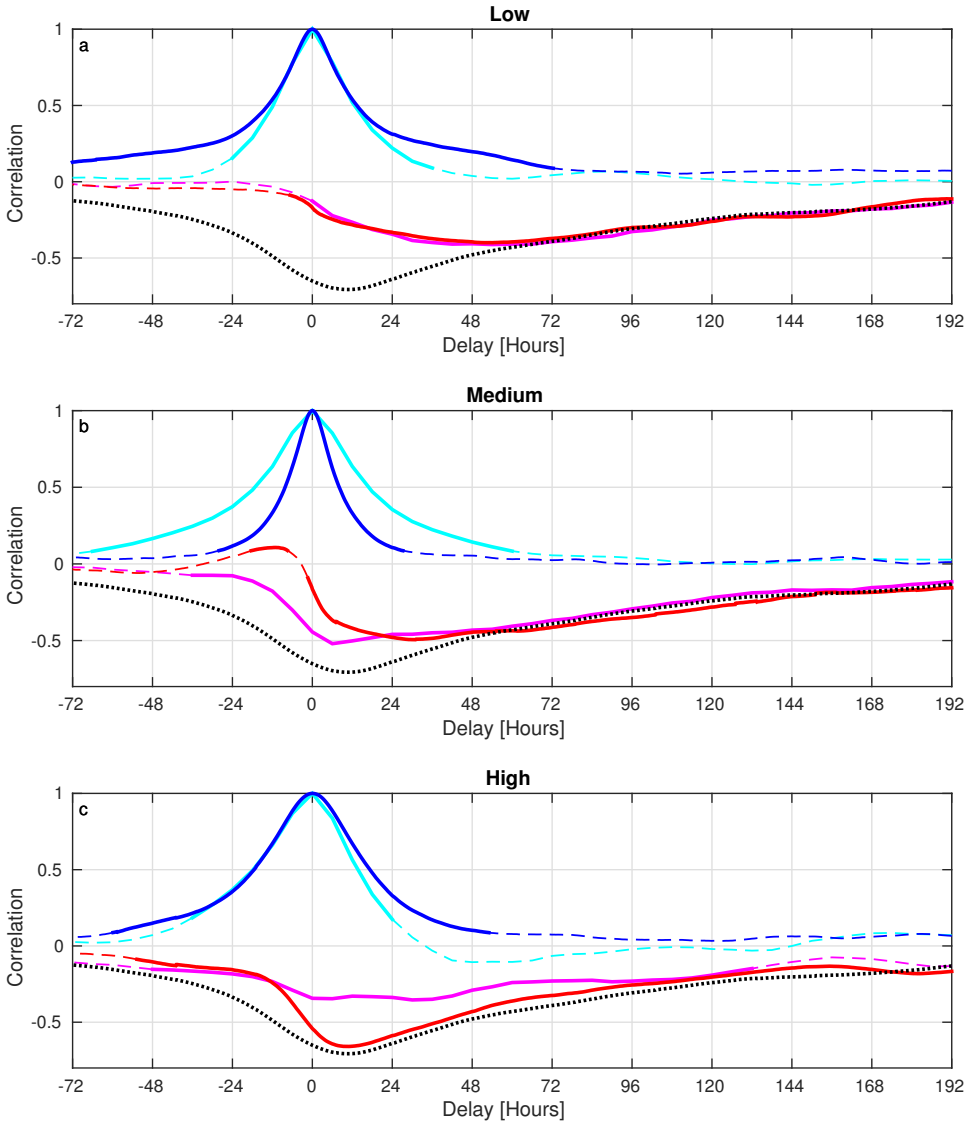

FIGURE 4.5: Cross-correlation curves for SIC and AWS (red) and ERA-Interim (magenta) wind speeds at the Laurie II AWS site for periods of low **(a)**, medium **(b)** and high **(c)** winds. Wind autocorrelation curves for low-, medium- and high-wind cases from AWS (blue) and ERA-Interim (cyan). Dashed lines indicate significance $p > 0.01$. The dotted black line represents the cross-correlation curve for the total of all wind cases for comparison.

The CCF of temperature versus sea ice concentration also shows a significant negative correlation with the minimum occurring at a 0 h delay (Figure 4.4b). The

e-folding times for this curve are −120 and 170 h for the decreasing and increasing periods, respectively. These values are both similar to the autocorrelation *e*-folding time for temperatures measured at Laurie II of 150 h. As a strong wind event progresses and SIC decreases, the heat flux from the ocean to the atmosphere will increase, causing the production of new sea ice through freezing. The rate of freezing of open water will depend on the temperature differential between the ocean and the atmosphere, potentially explaining the significant correlations observed. Significant positive correlations can also be found between the temperature and wind speeds measured at the Laurie II station (Figure 4.4b), which we interpret as at least partially the cause of the correlation between temperature and SIC. In addition, work detailed in Coggins et al. (2014) also suggests that strong wind events, particularly Ross Ice Shelf airstream (RAS) events (Parish et al. 2006), are related to warm surface temperature anomalies. This is due to changes in low-level stratification. During periods of low winds, a layer of cool, dense air is observed near the surface, while during higher wind speeds the warmer overlying layer is mixed down toward the surface. Adiabatic warming linked to air traversing the Trans-Antarctic Mountains also contributes to this temperature anomaly. However, given that the correlation between temperature and wind speed at Laurie II is 0.5 at zero hours and the correlation between temperature and SIC is −0.65, there must be some other causal link between temperature and SIC. We suggest that this is likely due to a more gradual rate of freezing of open water during periods of higher air temperatures (effectively a smaller temperature differential between ocean and air temperatures impacting the sensible heat flux)

4.3.4 Comparison of ERA-Interim and AWS CCFs

CCFs were also produced using the ERA-Interim virtual AWSs in the same manner, although at a 6 h temporal resolution dictated by the temporal resolution of the ERA-Interim output. We found that both the wind speed, SIC and wind speed autocorrelation were very similar to those found using the AWS wind speeds (Figure 4.2a). This is not surprising since the ERA-Interim wind speeds correlate well with those of AWS at Laurie. The CCF of temperature versus SIC, CCF of temperature versus wind speed and the temperature autocorrelation from the ERA-Interim output have similar forms to the relationships derived using AWS data but are generally smoother and the magnitude of the largest correlations are generally smaller. The temperature autocorrelation curve shows that ERA-Interim predicts more persistent temperatures than the Laurie II AWS measures.

This likely indicates that high-frequency temperature fluctuations are not accurately modelled within ERA-Interim. The ERA-Interim CCF of wind speed versus temperature shows weaker correlation for delays less than 24 h, with the difference becoming negligible around −72 h. This probably indicates that the warming of the air due to mixing, suggested in Coggins et al. 2013 and other studies, caused by strong winds is underestimated in ERA-Interim. These effects likely cause the small differences between the ERA-Interim temperature and SIC correlations and the correlations of the Laurie II AWS.

Cross-correlation curves for SIC and wind speed measured at Laurie II AWS site and wind speed hindcast from the ERA-Interim virtual station are now examined (Figure 4.5a-c). The daily mean wind speeds measured at Laurie II were categorised into low, medium and high-wind events based on 33rd and 66th percentile AWS wind speeds measured at Laurie II (3.5 and 7.6 ms^{-1}, respectively). Wind direction was not considered in this classification because of the predominance of southerly flows at the site. CCFs for SIC with wind speed were calculated only for periods when the mean wind speed during a −12 to +12 h period was within one of the three categories (Figure 4.5). Autocorrelation curves for the wind in each of these three cases were also calculated to allow the persistence of each of the three strengths of wind speed events to be identified. The AWS medium-wind case autocorrelation curve (Figure 4.5b) shows considerably lower persistence than either of the extreme cases, indicating that this is a transition state that occurs frequently for short periods. The high-wind case (Figure 4.5c) shows a CCF very similar to that of all cases (Figure 4.4b), excluding the period from −36 to +12 h delay.

The force exerted on sea ice is proportional to the wind stress, which is proportional to the square of the wind speed. This will cause the winds within the high-wind case to have a greater impact on sea ice motion than those of the lower cases. All cases show negative correlations between SIC and wind speed. With the exception of a short period in the medium case, spanning −30 to 6 h, when weak positive correlations were observed. The medium case has a correlation extrema of −0.5 at 30 h, while the extrema for the low case is −0.4 at 50 h between AWS and SIC data. Both these values are significantly weaker and later than those of both the high and total cases. This could be because weaker wind speeds will not have as significant of an effect on sea ice, causing any advection of sea ice and subsequent sea ice break up to occur much less rapidly than the high-wind case. Another possible cause is that the higher wind speeds within each class are more likely to increase to stronger cases after the classified period,

causing a decrease in SIC at a large delay. Due to the autocorrelation for both medium and low cases being very low at their respective times of extrema, the former explanation seems unlikely since there would be little coherence between wind speed at 0 h and wind speed at the extrema.

The categorised autocorrelation curves found using the ERA-Interim virtual station are not as perfectly symmetrical as those for the AWS data. This is due to sampling issues that occur at the beginnings and ends of the broken time series, obtained because of the wind speed classifications used. These sampling issues are also present in the AWS autocorrelation curves but are of greater significance when using the low-temporal-resolution ERA-Interim data. The medium ERA-Interim wind speed autocorrelation curve shows persistence similar to that of the low and high cases, differing from that of AWS, which showed a much shorter persistence in the medium case. In the low-wind case, CCF of wind speed versus SIC derived from ERA-Interim output is very similar to that found using AWS. In contrast, the ERA-Interim CCFs in the medium- and high-wind-speed cases differ significantly from those of AWS. In particular, the ERA-Interim medium case displays stronger negative correlations than that of the AWS between -24 and 24 h, after which the two are very similar. The high-wind regime for ERA-Interim displays significantly weaker correlations between -12 and 72 h than the corresponding pattern derived using AWS data. The latter point likely reflects the fact that the ERA-Interim data are generally poor at representing the strength of the wind in the strong-wind-speed periods for this region, this being supported by the large gradient derived (1.70) when applying a linear least squares regression to the ERA-Interim and AWS wind speeds.

4.3.5 SIC anomalies during extreme wind events

To gain a greater understanding of the influence of winds on SIC in the region, we now consider the spatial structure of the SIC anomalies for the high- and low-wind classes previously identified for different periods relative to the onset of those classes. For both low- and high-wind classes, the April to October mean bootstrap SIC anomaly for each pixel in the Ross Sea region was calculated over the 2001-2014 period (defined by Laurie II AWS coverage) (Figure 4.6). Composites for several days of delay before and after the wind event onset were then derived to highlight how the sea ice anomaly varies spatially prior to and following these wind classes. Histograms are also shown to indicate how the distribution of each wind class changes throughout the period examined. On day zero all cases

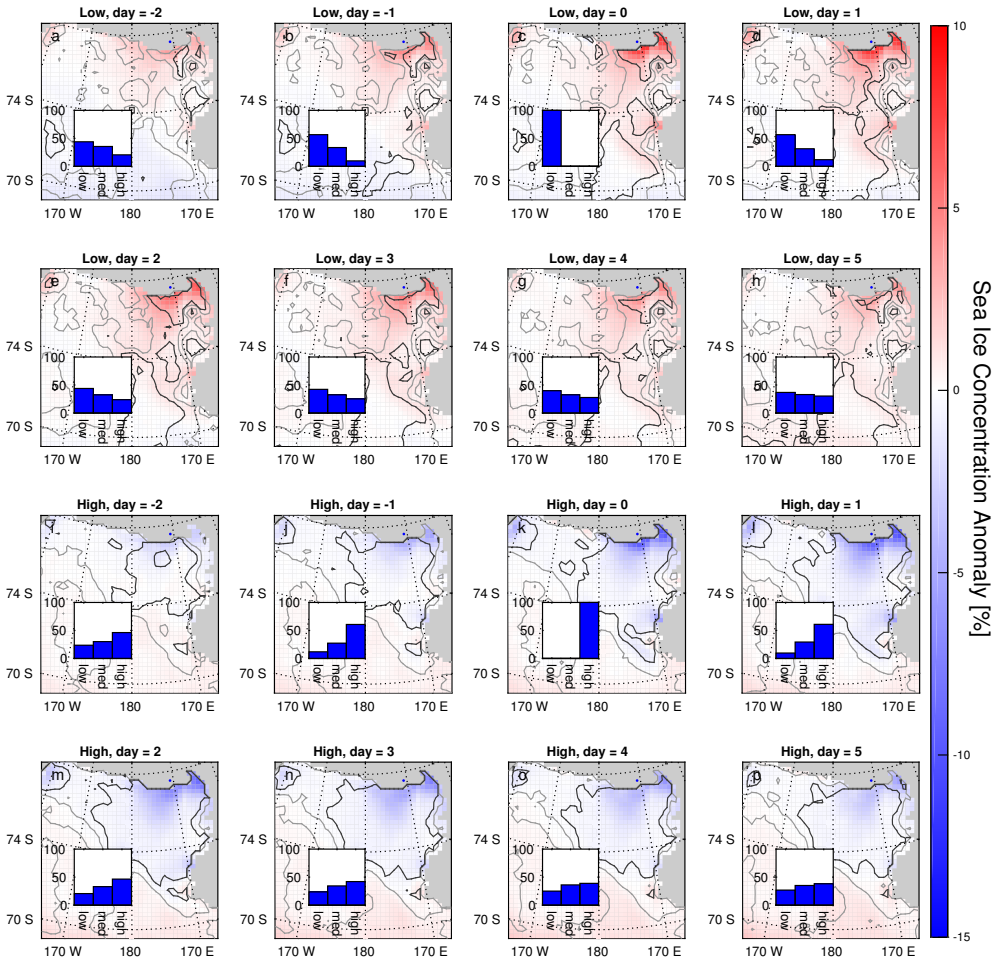

FIGURE 4.6: Composites of 2000–2014 sea ice concentration anomaly at varying delay for low-wind cases **(a–h)** and high-wind cases **(i–p)**. The grey and black contours indicate 80 and 99 % significance, respectively. The inset histograms indicate the percentage of the three wind cases that occur at the respective delay.

are either 100% high or low winds, but on following days the winds are not classified. This allows the persistence of these wind events to be observed.We find significant, positive anomalies within the Ross Sea polynya during low winds and negative anomalies during high winds in general (Figure 4.6). No significant anomalies were found during the medium-wind cases and these are therefore not displayed. All significant anomalies found occur within known polynyas; this is likely because sea ice is generally thinner and has a lower concentration within polynyas. Significant anomalies are observed 2 days before the measured wind and remain until 5 days after. An imbalance in the proportions of the three wind

classes (indicated by the inset histograms) also remains for a similar period. The CCF of SIC versus wind speed displayed increase and decrease e-folding times of -48 h and 100 h (Fig. 4.4). Thus, during a high-wind event the period where SIC is decreasing seems to be significantly impacted by advection.

4.3.6 Sea ice motion anomalies during extreme wind events

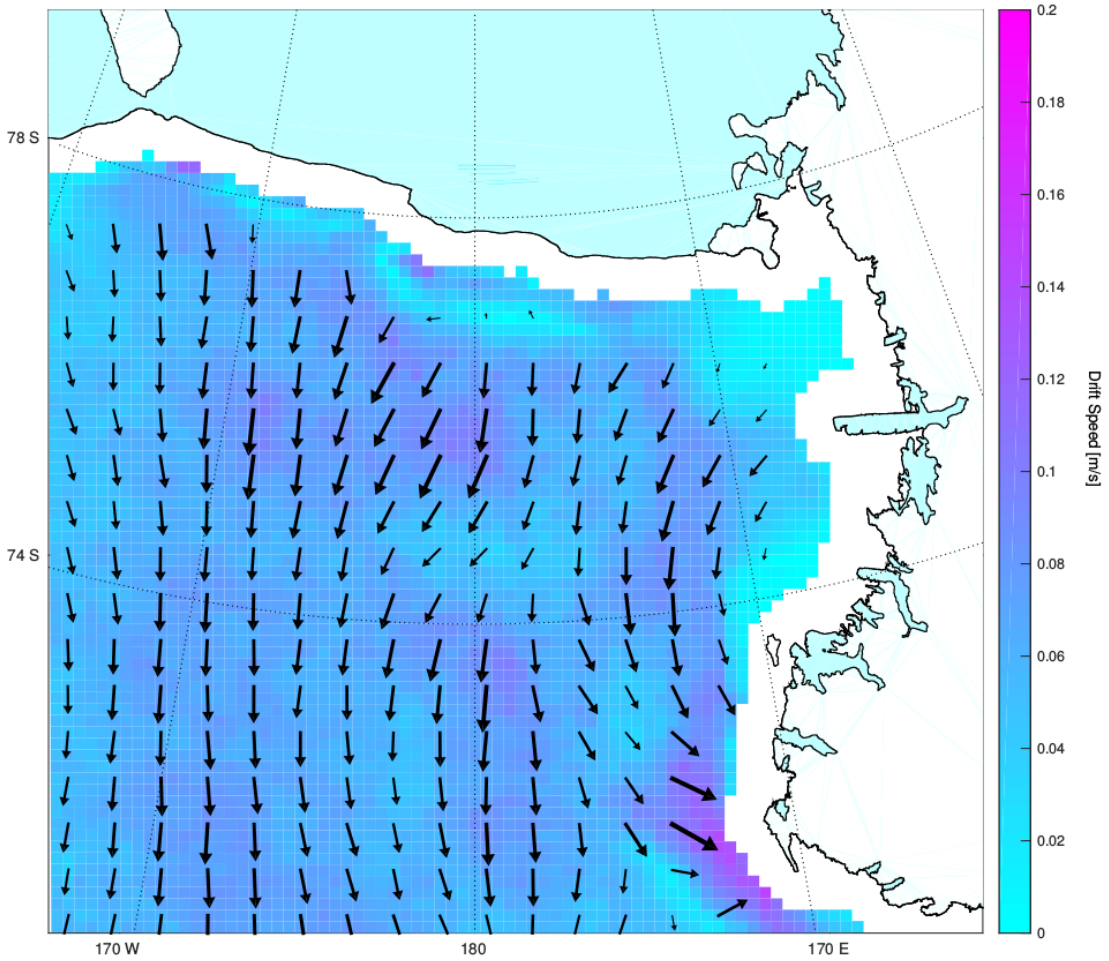

FIGURE 4.7: Mean sea ice motion vectors in the Ross Sea region. Arrows indicate the mean sea ice drift vector over a 100×100 km region. The color scale indicates the magnitude of this vector field.

The mean sea ice motion vectors for April-October 2001 until 2014 (Figure 4.7) show northward flow throughout the Ross Sea, with an easterly component occurring to the east of Cape Adare. This highlights the net export of sea ice from the north-facing coasts of the Ross Sea throughout this period (Comiso et al.

2011). Composites of sea ice motion anomalies related to high- and low-wind states at delays varying from −2 to 3 days from the wind event are displayed in figure 4.8. During periods of low wind speed at Laurie II, anticyclonic anomalies occur throughout the Ross Sea (figure 4.8a-f). Conversely, cyclonic anomalies are found during periods of high winds at Laurie II (figure 4.8g-l). These anomalies are largest at zero lag but persist for 24 h after the wind event, with weak anomalies being found in both low and high states 48 h after the wind event. It is also noticeable that no coherent pattern in the sea ice anomalies associated with the medium-wind state are observed (not shown). The cyclonic anomalies during strong wind events and anticyclonic anomalies during low-wind events highlight the critical influence of atmospheric near-surface winds on sea ice motion in the region.

4.4 Discussion

Bromwich et al. (1998) found annual correlations between SIC in the RSP and wind speed at the Ferrell AWS for 1988–1991 ranging from −0.3 to −0.52. We found the multiyear correlation for SIC in the RSP and wind speed at the Ferrell AWS from 2001 to 2014 to be −0.67. Bromwich et al. (1998) used a RSP area that extended significantly further from the shore than the one used in our analysis. Winds over the Bromwich RSP area were not as well represented by the Ferrell AWS, explaining the weaker correlations. We found a minimum correlation between Ferrell wind speed and SIC to be −0.72 at a 10 h delay; Bromwich et al. (1998) did not calculate correlations at varying delay, making comparison with this value impossible. Bromwich et al. (1998) also found correlations between SIC and inverse temperature ranging between 0.44 and 0.55. We found a correlation of 0.64 between SIC and inverse temperature; this difference is due to the different RSP area and time periods used.

ERA-Interim was able to generate wind speeds that correlated well with those of several AWS sites, indicating that the relative wind speeds within ERA-Interim were consistent with the AWS measurements. However, at AWS sites near significant topography, ERA-Interim was found to predict wind speeds significantly weaker than the winds measured by the AWS, with slopes of the regression lines of 1.70 and 1.52 (implying that the ERA-Interim values are this factor smaller than the AWS measurement) at the Laurie II and Ferrell sites, respectively (Fig. 4.3). This is likely because ERA-Interim is unable to accurately model the mesoscale barrier affect of Ross Island and the resulting flow convergence. This hypothesis

is supported by recent comparisons between AWS data and mesoscale model output in the region (Jolly et al. 2016). The CCF of wind speed versus SIC produced using the virtual Laurie station was very similar to that found using the Laurie AWS data. However, when the data were separated into low-, medium- and high-wind regimes, based on a categorisation derived from the AWS data, significant differences were found between the ERA-Interim and AWS CCFs. This suggests that the ERA-Interim output provides a good representation of the occurrence of the different wind states, but the magnitudes from the ERA-Interim underestimate the values observed by AWS. This indicates that ERA-Interim output is not be a reliable way to identify relevant wind thresholds used in models simulating polynya dynamics. This factor makes the usage of ERA-Interim problematic for polynya studies since they generally form on coastlines near topography in Antarctica. ERA-Interim provides 10 m wind speeds, while the AWS wind speeds are measured at 2–3 m (Dee et al. 2011; Lazzara et al. 2012). This would suggest that a scale factor exists between the two data sets, an effect that was not corrected. While this will not affect the correlation comparisons performed, it may explain the scale factors observed. However, this small height difference is not able to explain the large-scale factors found, indicating that topography must have a significant effect.

Sea ice motion vector anomaly composites indicate that wind-driven sea ice drift is significant 12 h before through to 36 h after strong wind events peak. This coincides with the peak cross correlation between SIC and wind speed, indicating that during a strong wind event, SIC within the RSP is at a minimum during the period where wind-driven sea ice drift is found to be significant. Following strong wind events, significant negative SIC anomalies are also found and persist for up to 5 days after the event. This period is longer than the persistence of most strong wind events (see autocorrelation in figures. 4.4 and 4.5), and it therefore seems unlikely that the SIC recovery following strong wind events is controlled by wind-driven advection of sea ice. During the recovery period, sea ice motion vectors do not demonstrate an advective recovery. Thus, the recovery of sea ice is presumed to be dominated by formation of new sea ice within the RSP rather than advection of existing sea ice, an assumption supported by recent analysis detailed in Nakata et al. 2015. During periods of high wind, negative SIC anomalies were found within the Ross Sea polynya. Similarly, positive anomalies were found during periods of low wind. The significant anomalies were also only found within areas of known polynyas, likely due to thinner, less concentrated sea ice being present within the polynyas. Correlations between wind speed and SIC were significantly stronger for the high-wind class than the

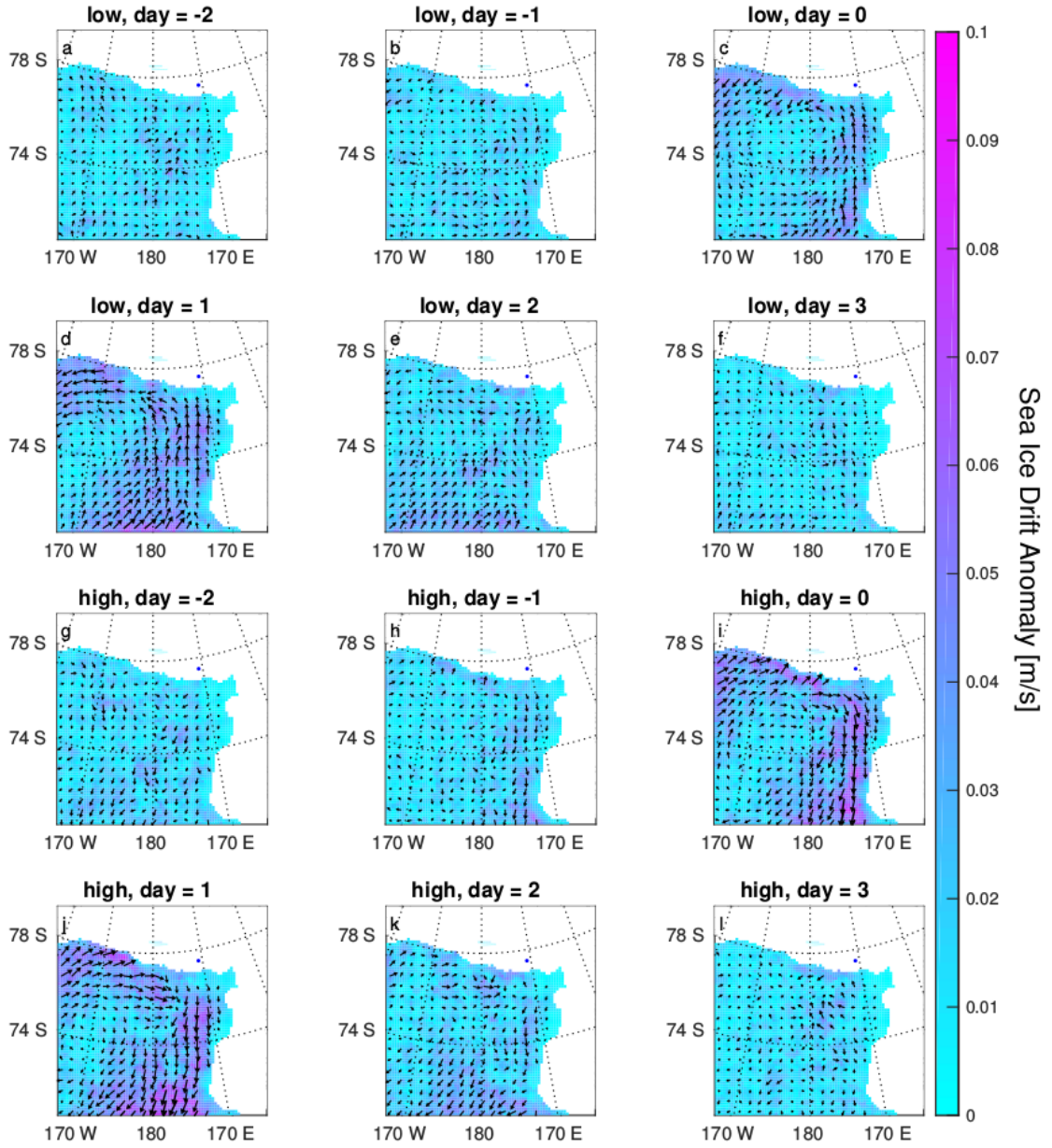

FIGURE 4.8: **(a–f)** Sea ice motion anomalies for days −2 to 3 for low-wind events. **(g–l)** Sea ice motion anomalies for days −2 to 3 for high-wind events. Composites are formed over the 2000–2014 period.

two weaker classes (Figure 4.5), indicating that the wind-driven polynya mechanism is driven by the strongest wind speeds and moderate winds have a less significant effect.

The wind stress on sea ice depends on the square of the wind speed. This does not however result in a linear relationship between SIC and the square of the wind speed because wind stress only defines the force causing the advection. For

this reason wind speed was correlated with SIC rather than the square of wind speed. Only wind speed was considered in this study; therefore northerly winds were not distinguished from southerly winds, even though they would have a vastly different effect on polynyas. Coggins et al. 2014 found that the majority of wind measurements in the northwestern RIS fall within the southwestern quadrant due to the dominance of katabatic-fed drainage and barrier flows related to the Transantarctic Mountains and a semi-persistent low-pressure system east of the Ross Sea. This was also identified in detail analysis around the Laurie II region presented in Jolly et al. 2016. This directional bias becomes even stronger when only the largest wind speeds are considered. This means that errors due to northerly winds are minimal in our analysis.

Only the results obtained from weather data taken at Laurie II are presented in this study because of its proximity to the RSP. However, a similar set of analyses were performed for the Vito, Emilia, and Ferrell AWS sites. These produced similar results, with the only significant difference being that weaker correlations were found at these sites when compared to those with Laurie II. This is hypothesised to be because these sites are based further inland, and are therefore more distant from the center of the RSP than Laurie II. This would mean that the winds at these locations would be less representative than those at Laurie II.

Due to lack of weather data available within the RSP, AWS data from sites on the nearby Ross Ice Shelf were assumed to be representative of that over the RSP. A multitude of effects will cause the actual winds and temperatures over the RSP differ somewhat from those measured at the Laurie II AWS site. These effects will be inhomogeneous across the RSP. Proximity to topography, particularly Ross Island, differs between the RSP and Laurie II. Southerly katabatic drainage flows will accelerate around Ross Island, causing stronger winds to be observed within the RSP. Meanwhile, other areas of the RSP north of Ross Island will be somewhat sheltered from many of the predominant southerly winds. Due to the relatively warm ocean, an upward heat flux will occur within the RSP when open water or thin ice is present. This will cause an increase in surface air temperatures over the RSP. This effect will not occur at Laurie II due to the insulation of the thick ice shelf. Due to the lack of measurements within the RSP, the net result of these effects is unidentifiable.

When within 50 km of the coastline, the sea ice motion vectors used in this study are biased. This coastal area coincides with the majority of polynya activity and therefore the dynamic effects of changing wind speeds were not able to be observed directly within the RSP. The assumption is made that offshore sea ice drift

will be representative of drift in coastal polynyas. Although derived sea ice motion is coherent throughout the Ross Sea, the motion within coastal polynyas may be different since thinner, less concentrated ice exists within coastal polynyas.

The bootstrap SIC data used throughout this study use passive microwave measurements to calculate SIC. The microwave signature for a thin sheet of ice can be identical to that of scattered thick ice. For sea ice thickness less than 10 cm, the bootstrap sea ice concentration is a function of sea ice thickness (Kwok et al. 2007). During periods of low wind speed, bootstrap SIC within the RSP often reaches 100 %, indicating a continuous covering sheet of sea ice with thickness greater than 10 cm. During a strong wind event, the SIC decreases via dynamic processes, leaving areas of open water with scattered, likely thick ice. As freezing of the open water occurs, a layer of thin ice will form, causing a gradual increase in the bootstrap SIC. As this sea ice thickens, the heat flux between the warmer ocean and the cooler atmosphere will decrease, causing the rate of freezing to also decrease. Because both bootstrap SIC and the rate of freezing within a polynya depend on the thermal conductivity of the sea ice, the bootstrap SIC may actually provide a more meaningful measure of sea ice production within polynyas than true SIC values.

Despite the length of the bootstrap SIC time series, we were unable to identify any significant trends in polynya activity. This may be due to changing polynya structure as a result of calving from the Ross Ice Shelf and the ice shelf gradually advancing northward. As the coastline evolves, so does the RSP. This causes issues since the land mask for bootstrap SIC data does not change with time. Over long periods, a changing amount of the RSP is visible in the bootstrap SIC data, causing biases in any metric for polynya activity. This effect was particularly obvious in 2005 when iceberg B15 calved from the Ross Ice Shelf, moving a 300 km long section of the northern coastline 40 km further south.

4.5 Conclusions

During the austral winter, strong negative correlations were found between AWS wind speeds and SIC in the RSP. In contrast to previous studies, we examined these correlations as a function of lag and found that they persisted for several days and exceeded the persistence of the wind speed autocorrelation. When the data were split into low-, medium- and high-wind cases and correlations were calculated from the separate data sets, the high-wind states displayed stronger correlations than the other two states, indicating that stronger winds had the

most significant impact on sea ice within the RSP. This analysis was repeated using a virtual AWS site interpolated from ERA-Interim reanalysis wind fields. It was found that although strong correlations existed between the AWS and ERA-Interim wind speeds, a linear scale factor, significantly greater than 1 was present at AWS sites in close proximity to topography. Wind speeds measured at the Laurie II AWS correlated strongly with co-located ERA-Interim wind speeds, but a scale factor of 1.70 (indicating AWS wind speeds were 1.70 times faster than ERA-Interim wind speeds) was found. The ERA-Interim wind speeds were used to calculate a wind speed against SIC CCF that agreed with the CCF formed using AWS wind speeds. However, when the data set was categorised into low-, medium- and high-wind cases and individual CCFs were calculated, significant differences from the AWS CCFs were found in the high-wind state. Likely due to the effects of nearby small-scale topography, ERA-Interim wind speeds were unable to reproduce the relationships found between AWS wind speeds and SIC in the RSP. This difference has implications for interpreting sea ice anomalies using ERA-Interim winds in regions close to complex topography.

For low-, medium- and high-wind states measured at Laurie II, AWS composites of SIC were made. During periods of low wind speed ($< 3.5\,\mathrm{ms}^{-1}$), significant positive SIC anomalies that persisted for 5 days after the wind event were found within the RSP. Conversely, significant negative SIC anomalies that persisted for 5 days after the wind event were found within the RSP during periods of high wind speed ($> 7.5\,\mathrm{ms}^{-1}$). No significant anomalies were found during medium-wind-speed periods. Significant SIC anomalies were only found to occur in coastal areas where polynya are known to occur. Composites of sea ice motion vectors were also calculated for these wind states. During periods of high-wind cyclonic motion, anomalies were found throughout the Ross Sea, while anticyclonic anomalies were found during periods of low wind. These sea ice motion anomalies were found to persist for 48 h after the wind event. SIC anomalies persisted several days longer than sea ice motion anomalies. This suggests that following a strong-wind event, polynyas reform sea ice through thermodynamic, rather than advective processes, resulting in increased sea ice production within polynyas following strong-wind events. This implies that changes of winds in this region would have significant impacts on polynya processes, potentially strongly impacting coastal sea ice production. This study shows that coarse resolution atmospheric reanalysis data would not capture the correct magnitude of this effect.

Chapter 5

A Comparison of Antarctic Mesoscale Prediction System (AMPS) Forecasts near the Ross Sea Polynya With Controlled Meteorological (CMET) Balloon Observations

This chapter has been submitted as a standalone journal article in the *Journal of Geophysical Review - Atmospheres* and is in review at the time of writing.

Abstract

This study presents atmospheric boundary layer observations made over the Ross Sea using a long-duration Controlled Meteorological (CMET) balloon and a comparison with Antarctic Mesoscale prediction System (AMPS) forecasts. The CMET balloon was launched on the 22nd of November 2017 at 1230 UTC, this flight performed 31 repeated soundings of the atmospheric boundary layer over a period of 70 hours. During the flight the balloon made close passes of the open Terra Nova Bay and Ross Sea polynyas. We use the AMPS forecast during the flight to understand the influence of the polynya on the air sampled by the CMET balloon. Balloon observations of temperature, humidity, and wind velocity generally agree with AMPS forecasts, with the largest disparities in the wind direction field during periods of light wind, and when the path of the balloon was near complex topography. To understand the thermodynamic interaction between these polynyas and the atmospheric volume sampled by the balloon, a Lagrangian trajectory model forced by AMPS winds was used to calculate the total and partial derivatives of potential temperature as well as the total water mixing ratio. This allowed us to identify sources and sinks of both observed heat and moisture, and to directly quantify and assess the thermodynamic profile of the overlying atmospheric boundary layer. We were able to quantify the spatial footprint of the region influenced by the heat emitted from the Ross Sea Polynya at the time of the flight to be 20,000 km^2 based on the AMPS forecast.

5.1 Introduction

Meteorological variability over the Ross Sea and Ross Ice Shelf (RIS) is strongly impacted by synoptic and mesoscale dynamics driven by orographic features such as the Trans-Antarctic Mountains, surrounding ice sheets, and the mixed surface cover (open waters and sea ice) of the Ross Sea (Cassano et al. 2016; Costanza et al. 2016; Nigro et al. 2012a). These features induce both synoptic and mesoscale modulations in the lower atmosphere, resulting in the observed, highly variable temperature and precipitation patterns. Radiatively cooled air over the East and West Antarctic Ice Sheets feed katabatic flows down steep glacier valleys from East Antarctica, and more moderate slopes from West Antarctica, onto the Ross Ice Shelf (Bromwich 1989). These katabatic flows frequently combine with synoptic scale cyclones over the Southern Ross Sea, which produce pressure gradients parallel to the Trans-Antarctic Mountains, driving a strong, southerly airflow along the barrier formed by the Trans-Antarctic Mountains (Parish and Bromwich 1997, 1998). This climatological airflow pattern is known as the Ross Air Stream (RAS) (Coggins et al. 2014; Costanza et al. 2016; Parish et al. 2006).

The strong winds during RAS events are known to cause the break-up of sea ice in the polynya region and the advection of sea ice from the Ross Sea Polynya (RSP), a large coastal polynya that forms in the Southern Ross Sea (Bromwich et al. 1998; Dale et al. 2017). The combination of thin ice and exposed warm water relative to the overlying atmosphere within the RSP is responsible for large ocean-to-atmosphere fluxes of heat and moisture (Batrak and Müller 2018). Previous work detailed in Bourassa et al. 2013 has identified that the representation of sea ice in weather prediction models has important consequences for the atmosphere-sea ice interaction on a wide range of spatiotemporal scales, since sea ice is a dominant constraint for atmospheric surface fluxes in polar regions. This in turn results in accelerated sea ice production rates (Tamura and Ohshima 2008).

Sea Ice cover is the most dynamic component of the Antarctic cryosphere and any change is related to variations in the atmosphere and oceanic patterns over a multitude of scales (Bourassa et al. 2013). The observed increase of Antarctic sea ice extent over the satellite observation period is largely driven by changes in the Western Ross Sea and likely related to feedbacks in the ice-ocean-atmosphere system (Holland and Kwok 2012). The highest sea ice production rates are observed within coastal polynyas, which control the production of high salinity shelf water and thermohaline circulation (Drucker et al. 2011). Despite this climatological significance and the possible link between increased sea ice production and

meteorological variability the boundary layer processes linking the synoptic and mesoscale are still relatively under explored in this area. This is largely to the lack of suitable measurement technologies and the limitations to conduct such measurements in this hostile and extreme region.

The Antarctic coast's complex topography and the effect of variable sea ice cover can introduce significant departures from large-scale influences with localised impacts. For example, it is well established that prominent coastal topographies, like the Antarctic Peninsula, interact with synoptic or large cyclonic weather systems to shed smaller cyclonic eddies downstream of the topography and develop strong downslope storms that have implications on the surface heat budget and snow mass balance (Elvidge et al. 2015). The high frequency of occurrence of mesocyclones in the Terra Nova Bay region is of particular interest. These occur as a result of the convergence of the offshore surface wind field with northerly warm air currents and sea ice variability in this area (Carrasco and Bromwich 1993). Heinemann (1990) studied a 6-year climatology of mesocylones in the Weddell Sea and concluded that the majority of the mesocyclones occurred over ice-free areas and areas of converging offshore winds from valley tributaries. These studies reinforce the importance of the feedback mechanisms of the surface on such weather systems. These are usually maximised as cold air currents of an continental origin interact with the relatively warmer open water within polynyas, causing an uptake of moisture and heat and a resultant destabilisation into mesocyclonic systems. Several other studies (Bromwich 1991; Carrasco and Bromwich 1993; Turner and Thomas 1994) have suggested that localised weather systems occur during the open water seasons, driven by the main driving mechanism of heat and moisture uptake by the atmosphere. These results exemplify the dynamic nature of the atmosphere-sea ice-ocean interactions within the Ross Sea region.

In the context of regional climate predictions and both surface temperature and precipitation variability, it has become more important to assess the skill of our dynamical down-scaling models in representing these weather patterns in the Antarctic. Pezzi et al. (2016), when down-scaling climate model outputs, showed a 46% increase in mesocyclone frequency when compared to the lower resolution ERA-Interim reanalyses. This result was mainly attributed to the enhanced resolution and better resolved boundary-layer dynamics due to their smaller spatial scales. Pezzi et al. (2016) also attributes an increase in mesocyclone frequency to areas of large anomalies in surface sensible heat flux such as: the edge of the sea

ice, during cold air outbreaks over warmer lower latitude sea surface temperatures, and over polynyas (Bracegirdle and Kolstad 2010; Papritz and Pfahl 2016; Papritz et al. 2015). **Petrelli2008** demonstrated the importance of high resolution models for sea ice modelling. In a coupled sea ice-atmosphere model, winter sea ice formation within the Ross Sea and Terra Nova polynyas was found to double when model resolution was increased by a factor of five.

Flight and ground operations in Antarctica rely upon weather forecasts, such as the Antarctic Mesoscale Prediction System (AMPS). Several studies have sought to validate this model using surface-based automatic weather stations, including Nigro et al. (2012a, 2011), Bromwich et al. (2013), and Jolly et al. (2016). These studies have found that the greatest errors in AMPS simulations occur in regions of complex topography and low wind speeds. The accuracy of this model is limited by its spatial grid resolution in regions such as the Antarctic coast, where complex topography exists (Bromwich et al. 2005).

The main objective of this study is to compare observations made using Controlled Meteorological (CMET) balloons with predictions made by the AMPS forecasts. These observations were initiated from the complex coastal topographies of the western side of the Ross Sea region. Balloons then drifted with the synoptic, regional, and local weather systems over the variable surface cover of the Ross Sea including the Terra Nova Bay and Ross Sea polynyas. CMET balloons are designed for flights within the lower troposphere with height-controlled flights capable of repeated vertical probing of the atmospheric boundary layer over several days. These balloons have a payload mass similar to that of a standard weather balloon (Voss et al. 2012) and their unique design allow observations of inaccessible regions, such as the Ross Sea which contains complex coastal topography as well as vast areas of open water and sea ice.

CMET balloons have previously been successfully tested in both the Arctic and Antarctic regions. Voss et al. (2012) report a series of CMET launches from Svalbard during 2010 and 2011; the longest of these lasted for 24 hours and completed 18 vertical profiles. Roberts et al. (2016) compare data collected from 5 of these launches in Svalbard with model hindcasts made by ERA-Interim and the Arctic System Reanalysis (ASR). They found that the higher resolution ASR modelled the observations made by the CMET balloons more accurately than ERA-Interim. A CMET balloon was also launched from Troll Station, Antarctica by Stenmark et al. (2014) in January 2012. Hole et al. (2016) also launched two CMET balloons from Aboa Station, Antarctica in January 2013. These had flight times of 60 and

106 hours respectively, and the latter observed a mesoscale anti-cyclone over the Weddell Sea.

Here we use data from one of four CMET flights launched in 2017 from Mario Zucchelli station, located in Terra Nova Bay Antarctica (Figure 5.3) (74.695° S, 164.096° E). Two of these flights produced relevant data over the Ross Sea, spanning 18 and 70 hours of flight time. The other two balloons were less successful, the first was over-pressurised during inflation and suffered a loss of control 8 hours into the flight. The flight was terminated safely and the balloon therefore provided data of limited use. The final balloon suffered an electrical fault immediately after launch that prevented communications with the balloon thus no data was able to be collected from this balloon.

In this study we focus our analysis on data retrieved from the CMET balloon that provided the longest period of continuous observations. These CMET observations are compared to predictions made by AMPS, with particular focus on a 24 hour period starting at 0800 UTC on the 23rd of November 2017, in which the balloon flew into a region of air that was impacted by heat and moisture fluxes from the Ross Sea Polynya.

Another objective of this work is to quantify the thermodynamic representation of the Terra Nova Bay and Ross Sea polynyas using AMPS and CMET observations. This is achieved by the calculation of the Lagrangian and Eulerian derivatives of total water mixing ratio and potential temperature predicted by AMPS. The unique height controlled balloon observations of the Ross Sea region's atmospheric boundary layer, combined with moisture and heat budgeting from a numerical mesoscale model, allow new insights into AMPS skill in resolving surface-atmospheric exchange processes. As well as demonstrating a successful observational method for future regional weather and climate studies in this region.

5.2 Data and Methods

5.2.1 CMET balloons

CMET Balloons are controlled helium balloons designed to make flights with durations up to several days at altitudes less than 4 km (Voss et al. 2012). Throughout their flight CMET balloons measure air temperature, pressure, relative humidity, and GPS location. From the GPS location, the balloon's velocity can be derived and thus the local wind can be inferred. Data is transmitted back in

FIGURE 5.1: The author with a CMET balloon shortly after launch

real-time through the usage of an on-board Iridium 9603 satellite modem. This satellite connection is also used to receive commands, controlling the balloon's altitude and data acquisition frequency during flight.

Each balloon consists of two bladders: a high pressure reservoir and an outer

buoyancy bladder that is kept at atmospheric pressure. By pumping helium between the two bladders, the buoyancy of the balloon can be altered, allowing control over the balloon's altitude. This gives the CMET balloon a unique capability to make repeated soundings through the same altitude range. A schematic of the CMET balloon is shown in Figure 5.2.

The CMET balloon's 230 g payload comprises the control electronics, GPS receiver, satellite modem, pump-valve system, lithium polymer battery, photovoltaic panel, aspirated T-RH sensor, and a vacuum-insulated pouch. With this insulation, the payload temperature is maintained within acceptable operating limits (typically +20 K above ambient) even at altitudes of several kilometres in the polar regions. Pressure is measured using an aviation-grade pressure sensor (Freescale MPXH6115A) with a 16-bit analog-to-digital converter (Analog Devices AD7795). During flight, altitude is determined every 10 s by interpolating pressure to the US Standard Atmosphere. In post-flight processing, the pressure altitude is corrected for pressure offsets using the in-flight GPS altitude (Inventek ISM420). GPS latitude and longitude provide the position during flight and are also further analysed post-flight to determine eastward (U) and northward (V) wind speeds. The specified GPS position accuracy is $\pm$10 m RMS. Temperature is measured using a thermistor (General Electric MC65F103A) in a 10 k-Ohm divider circuit coupled to the aforementioned analog-to-digital converter. The specified thermistor accuracy is $\pm 0.1^\circ$ K over the temperature range 0 to 70° C. We note that during the flights presented here temperatures were outside this range so the accuracy of this thermistor was likely worse than $\pm 0.1^\circ$ K. A capacitance humidity sensor (G-TUCN.34 from UPSI, covering 2 to 98% RH range over -40 to +85° C) generates a variable-frequency signal which is a function of the ambient relative humidity (RH) with respect to water. While the humidity sensors have a specified accuracy of $\pm$2% RH, a pre-flight inter-comparison of the sensors indicated that the actual accuracy was substantially lower (on order of $\pm$10% RH).

As the altitude that the balloon flies at is changed, it often passes through a vertical wind shear. This can be used to provide limited control over the balloon's flight path, providing added flexibility during flights. Although the balloon is equipped with a solar panel, power management remains a major challenge throughout a flight. During periods of limited solar availability, the rate that data is sampled can be decreased to minimise power draw. This results in the data having a variable temporal resolution.

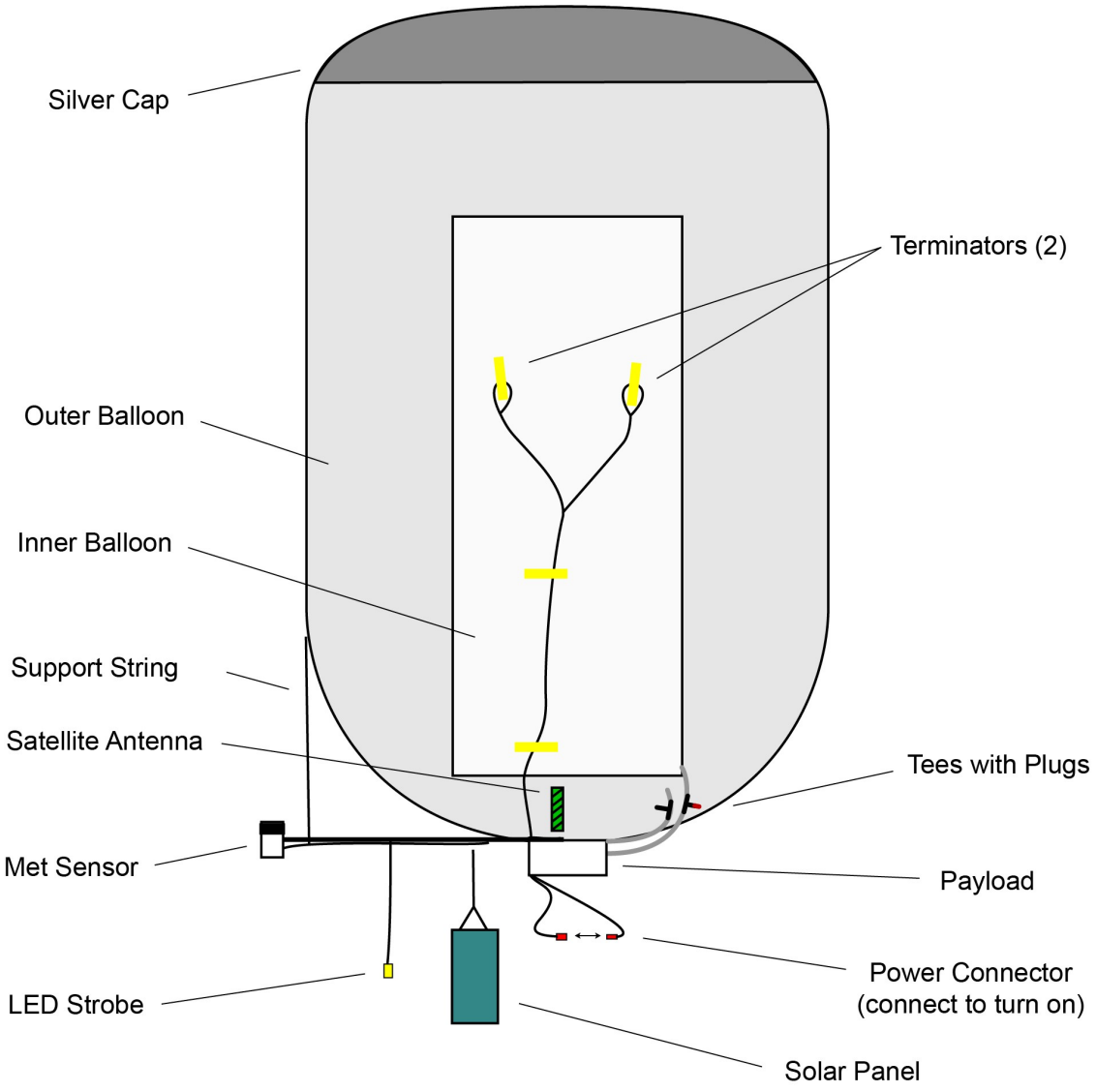

FIGURE 5.2: Schematic diagram of a CMET balloon

Hysteresis was observed between ascending and descending profiles of temperature and relative humidity measured by the CMET balloon. This is likely due to radiative heating of the slowly ascending balloon. Effectively a heated pocket of air enveloping the balloon is formed, which then rises alongside the balloon as it ascends. On descending profiles, this effect would be reduced as the heated air would continue to rise buoyantly away from the sinking balloon. Sensors were mounted on a 800 mm boom to increase the distance between them and the balloon with the aim of minimising this effect. Unfortunately, hysteresis was still observed. Consequently, measurements of temperature and relative humidity made during ascending profiles are excluded from our analysis. Measurements of wind speed and direction, derived from the GPS location of the balloon, were

not subject to this procedure.

Relative humidity measurements were calibrated post flight to agree with the measurements made by radiosonde balloons regularly launched from Mario Zucchelli station. Vaisala RS92-SGP radiosondes were launched twice daily, less than 1 km from the CMET launch site. CMET balloons were launched 1-1.5 hours after a radiosonde launch as radiosonde data were used to determine appropriate launch conditions for the CMET balloon. The first descending pass of each CMET flight was compared to the radiosonde observations. Radiative heating on the radiosonde balloons does not have a significant influence as the balloon rises much more rapidly than the CMET balloon, allowing the ascending profile from the radiosonde to be used A simple constant was added to the CMET relative humidity observations, so that a least-squares difference between the first descending pass of the CMET balloon and the ascent profile of the radiosonde was achieved.

The CMET balloon was launched at 1230 UTC on the 22nd of November 2017 from Mario Zucchelli station (74.695° S, 164.096° E). This balloon initially travelled northeast, roughly parallel to the Antarctic coast, for a period of 14 hours. The balloon then continued eastward towards the centre of the Ross Sea, passing just north of the Ross Sea Polynya by 2000 UTC on the 23rd of November. After 0600 UTC on the 24th, the synoptic scale flow changed direction, resulting in the balloon being carried north east out of the Ross Sea towards a large cyclone in the Southern Ocean (Figure 5.3). The total flight time of the balloon was just over 70 hours, though we focus on just over the central 30 hours of this period. For the majority of the first half of this flight, until 2000 UTC on the 23rd, the balloon performed repeated soundings between 50 m and 600 m altitude (Figure 5.3). Unfortunately, solar charging was limited due to overcast conditions, and after 2000 UTC on the 23rd of November a decision was made to stop the balloon sounding, the balloon remaining at an altitude close to 500 m after this point, and the data rate was decreased in order to conserve the balloon's battery power.

5.2.2 Antarctic Mesoscale Prediction System

The Antarctic Mesoscale Prediction System is a version of the Weather Research and Forecasting (WRF) model modified for polar regions (Powers et al. 2012). AMPS operates over several domains that cover a range of horizontal spatial extents and grid resolutions. This study analyses output from AMPS domain 3; which operates on a 2.67 km horizontal spatial resolution and has an output frequency of 1 hour. In this study we use AMPS WRF version 24 documented at: http://www2.mmm.ucar.edu/rt/amps/information/amps_esg_data_info.html.

Domain 3 covers a 1802 × 2766 km area spanning the Ross Sea, the Ross Ice Shelf, and the South Pole and is shown as a red rectangle in Figure 5.3a. Each AMPS domain uses 61 vertical levels, with 60 additional half levels between each full level. The model top is at 10 hPa and within the top 7.5 km vertical velocity dampening is applied. AMPS forecasts are issued at midday and midnight UTC. Forecasts output by the higher resolution domains 3, 5, and 6 have a output frequency of one hour spanning 40 hours, resulting in considerable overlap between consecutive forecasts. Forecasts for the lower resolution domains 1 and 2 instead cover 121 hours with a 3 hour output frequency.

AMPS obtains initial and boundary conditions from NCEP 0.25° GFS model output which operates on a 6 hour time resolution. Sea surface temperature data are obtained from the daily NCEP 0.5° model. Near-real-time ice and snow extent (NISE) data provide input sea ice concentration values (Brodzik and Stewart 2016). Data is assimilated using WRFVAR 3D variational data assimilation, with sea ice fields being updated in every other forecast.

The polar WRF model used in AMPS utilises a specific set of physics options. Cloud micro-physics are modelled using the WRF single-moment 5-class scheme which includes mixed phase processes and super-cooled water. The rapid radiative transfer model for GCMs models longwave radiation while shortwave radiation is modelled by the Goddard shortwave scheme. The Monin-Obukhov (Janjic Eta) scheme models the surface layer and surface physics are modelled using the Noah land surface model. The boundary layer is modelled using the Mellor-Yamada-Janjic (Eta) scheme. The higher resolution domains, including domain 3, do not include a cumulus parameterisation scheme. Sea ice is implemented using a fractional method, in order to determine surface fluxes, the surface-layer scheme is called twice, once for the area of open water and a second time for the area of sea ice within the cell. The resulting fluxes are then area averaged based on grid cell sea ice concentration (SIC) to determine the total flux within the cell.

5.2.3 Lagrangian trajectories

Lagrangian trajectories were used to trace the pathway of hypothetical air parcels. These were calculated using the AMPS forecast wind vectors (Powers et al. 2012), following the methodology detailed in Alexander et al. (2013) and Friedrich et al. (2017). Trajectories were launched from 500 m above the local surface topography, and were free to move vertically as they propagated. These trajectories were started at this altitude so that they started at close to the level that the CMET balloon travelled. At each trajectory time step, a 3 dimensional wind vector was

interpolated within the 4 dimensional (latitude, longitude, pressure, time) AMPS fields using cubic splines. A fourth order Runge-Kutta method was then used to propagate the trajectory path to the next time step. Trajectory calculations were performed in a local three dimensional Cartesian grid and then converted back to a latitude, longitude, and pressure coordinate system. For each trajectory, the potential temperature and specific humidity at each time-step were also calculated using a cubic spline interpolation from the AMPS grid.

A 5 minute temporal resolution was used for trajectory calculations; this is considerably shorter than the 60 minute output frequency of the AMPS output. The accuracy of trajectories is likely limited by the AMPS temporal resolution, therefore using higher temporal resolution for trajectory propagation will provide diminishing returns.

From each launch site, trajectories were propagated 12 hours forwards and backwards from the central start time, revealing both the origin and destination of each air parcel relative to its initial location. To avoid discontinuities between consecutive forecasts, each forward/backward trajectory set was calculated entirely using data from a single, continuous issue of the AMPS forecast. Each issue of a AMPS domain 3 forecast spans hours 0-39 and is calculated from one set of initial conditions. This results in the first 8 hours of the AMPS forecast not being used, removing potential errors due to model spin-up in AMPS (Bromwich et al. 2005; Guo et al. 2003; Jolly et al. 2016).

5.2.4 Lagrangian derivatives

Gridded Lagrangian derivatives of potential temperature and total water mixing ratio predicted by AMPS was calculated by launching Lagrangian trajectories both forwards and backwards in time from each grid point. Lagrangian derivatives describe the rate of change that a freely moving parcel of air would experience. Trajectories were launched on a 3.7 km by 3.7 km grid covering the South-Western Ross Sea. The mean derivative for a particular AMPS field was then approximated as the difference of that field at the time and location of endpoints from both the forward and backward trajectories. For this work, a trajectory length of 12 hours was used for both the forward and backward component, resulting in a mean derivative of a 24 hour period. Lagrangian derivatives were calculated using a two-dimensional grid of launch sites covering the Western Ross Sea, with constant initialisation heights of 250 m, 500 m, and 1000 m above the ground surface. Trajectories were allowed to freely propagate in three

spatial dimensions. The Lagrangian, or total derivative, can be related to the Eulerian derivative with the following equation:

$$\frac{\partial}{\partial t} = \frac{D}{Dt} - v \cdot \nabla$$

The partial, or Eulerian term, on the left hand side was also calculated over the same period for each point on the horizontal grid used as launch sites for the Lagrangian trajectory model within the AMPS domain. The final term on the right hand side, $-v \cdot \nabla$ is the advection term and was calculated as the difference between the Eulerian and Lagrangian terms. The advection term describes the effect of the wind field on the local rate of change of the given derivative By comparing the rates of change for variables in the Eulerian and Lagrangian frameworks, we can identify the causes for change at a specific location. We use this methodology to demonstrate that the CMET observations represented air masses, which were modified as they passed over the RSP.

5.3 Results

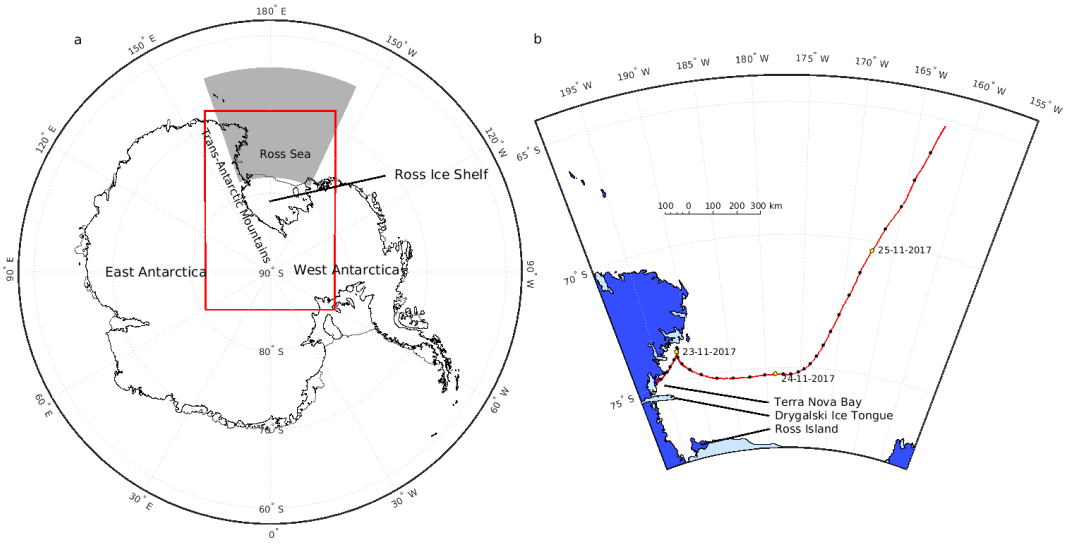

FIGURE 5.3: (a) Map of Antarctica, showing relevant geographical features. The red box represents the spatial extent of the Antarctic Mesoscale Prediction System (AMPS) domain 3 grid. The grey region indicates the area shown in panel (b). (b) Map of Ross Sea region showing the CMET flight path in red. The yellow dots represent the position of the balloon at 0000 UTC on the dates indicated, while the black dots are spaced at 2 hour intervals.

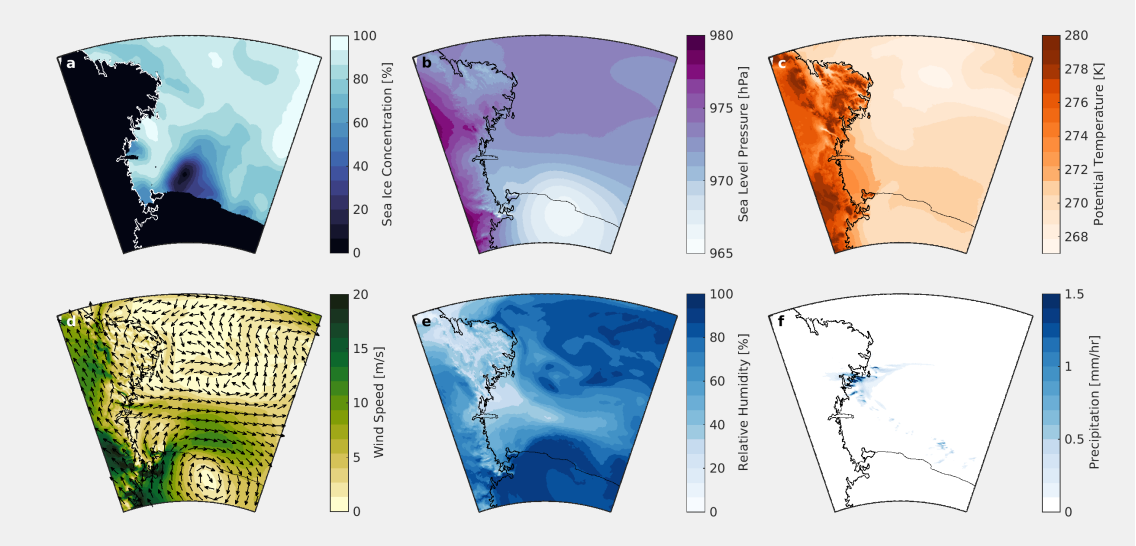

FIGURE 5.4: (*a*) AMPS sea ice concentration (SIC) over the Ross Sea on the 23rd of Nov 2017. (*b*), mean sea level pressure on the 23rd of Nov 2017. (*c-f*) Mean potential temperature, mean wind velocity, mean relative humidity, and mean precipitation over a 24 hour period starting at 0800 UTC on the 23rd of Nov 2017. As predicted by AMPS forecast issued at 0000 UTC 23rd of Nov 2017.

Figure 5.4 displays atmospheric parameters and sea ice conditions associated with the 23rd of November, to provide context for later discussion. The AMPS sea ice concentration on the 23rd of November (Figure 5.4a) indicates that the Ross Sea Polynya was open during this period, with 0% sea ice concentration being measured at the centre of the polynya. Decreased sea ice concentrations were also found in the McMurdo and Terra Nova Bay polynyas, although the SIC within these regions do not fall below 40%.

Average mean sea level pressure predicted by the AMPS forecast issued at 0000 UTC on the 23rd averaged over a 24 hour period, starting at 0800 UTC on the 23rd of November, is plotted in Figure 5.4b. Figures 5.4c-e show potential temperature, wind speed and direction, and relative humidity averaged over the same 24 hour period at 500 m above ground level. A cyclone is present over the northern edge of the Ross Ice Shelf, driving strong, southerly winds connected to a Ross Ice Shelf air stream event over the Ross Sea Polynya. A weaker anti–cyclonic system lies over the North–Western Ross Sea, enhancing the offshore flow near Terra Nova Bay also driven by the cyclone over the Ross Ice Shelf resulting in strong, dry, westerly winds over the Southern Ross Sea.

The relative humidity field (Figures 5.4e) shows two regions of very humid air over the Ross Ice Shelf and Northern Ross Sea. These regions are separated by a relatively dry band of air. This band of dry air originates over Terra Nova Bay,

with cool, dry air flowing down from Victoria Land and being drawn east by both the cyclone to the south and the anti-cyclone to the north. Meanwhile, the anti-cyclone to the north draws moist air that was previously north of the ice edge eastwards. Figure 5.4f shows the mean precipitation rate over a 24 hour period, starting at 0800 UTC on the 23rd of November. This shows a small area of precipitation over the Antarctic coast, just north of Terra Nova Bay, trapped between the cyclone and the anti-cyclone.

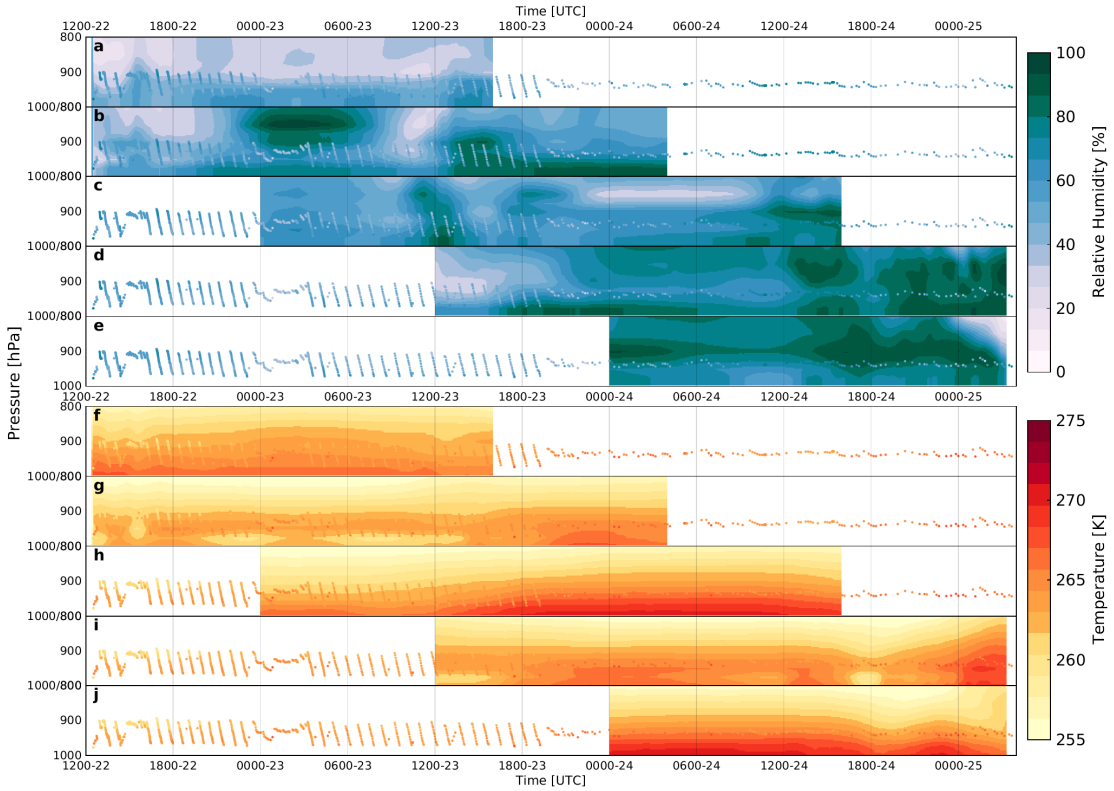

FIGURE 5.5: (a-e) Relative humidity forecast by AMPS on a pressure-time plane following the CMET flight-path. The individual panels represent consecutive AMPS forecasts. The overlying dots represent co-located CMET observations. (f-j) As for a-e but instead showing temperature.

Figure 5.6 and Table 5.1 provide a comparison of specific humidity and temperature predicted by AMPS at five different forecast initialisations (from 0000 UTC on the 22nd to 0000 UTC on the 24th of November at 12 hour intervals) with that observed by the CMET balloon along its flight-path. Similarly Figure 5.7 and Table 5.1 compares wind strength and direction forecast by AMPS for the same five forecast initialisations with CMET observations.

A vertical surface which follows the flight-path of the CMET balloon in space and time was derived, producing a two-dimensional curtain along the flight-path of the balloon. AMPS variables were interpolated using cubic splines from the

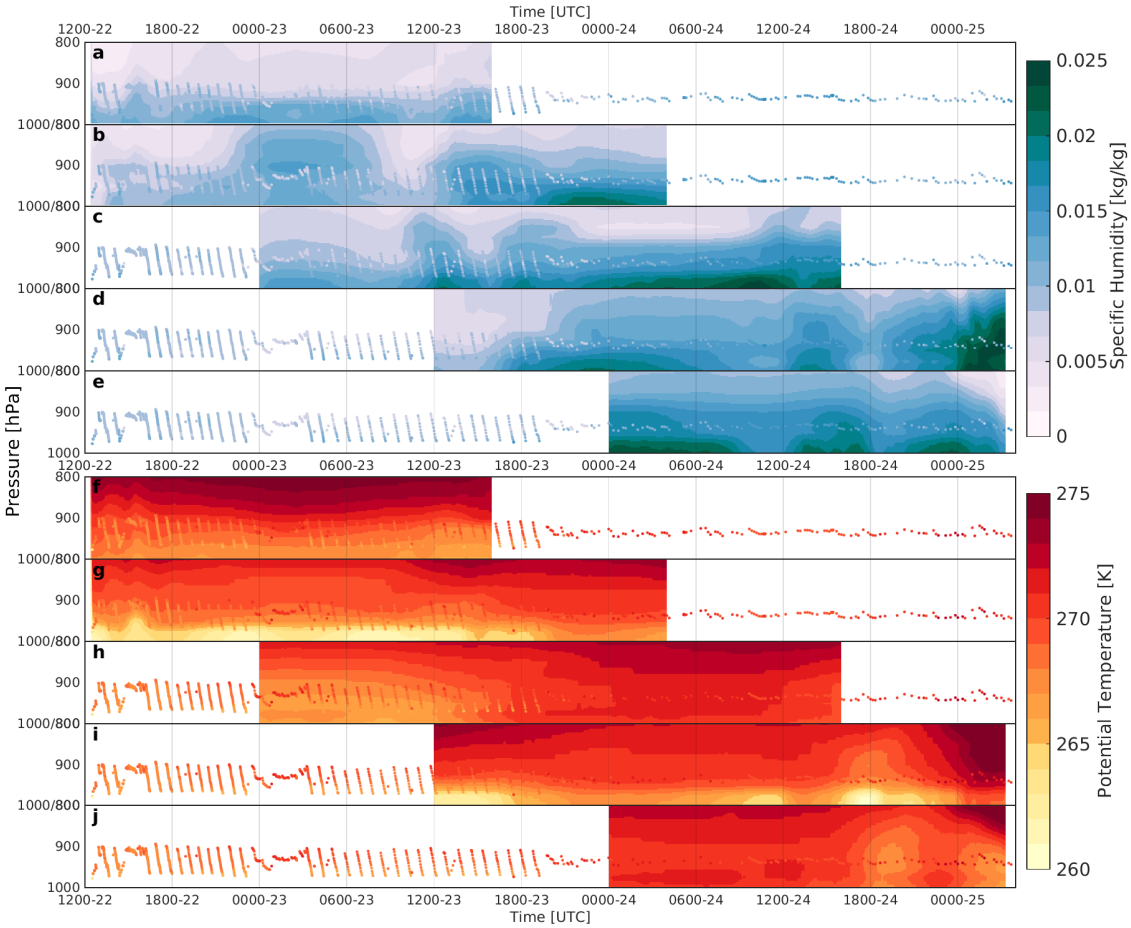

FIGURE 5.6: (a-e) Specific humidity forecast by AMPS on a pressure-time plane following the CMET flight-path. The individual panels represent consecutive AMPS forecasts. The overlying dots represent co-located CMET observations. (f-j) As for a-e but instead showing potential temperature.

four-dimensional (latitude, longitude, pressure, and time) AMPS grid to this two-dimensional (pressure and time) surface. CMET observations were then plotted over these surfaces using the same colour scheme, allowing for a qualitative comparison of AMPS and CMET observations.

A further, in-depth comparison of two individual descending CMET profiles and co-located AMPS forecast predictions is also provided in figures 5.8 and 5.9. Potential temperature and specific humidity predictions from the AMPS forecast issued at 0000 UTC on the 23rd were interpolated in four dimensions to the spatiotemporal location of each CMET observation. Figure 5.8 shows a sounding that was made by the CMET balloon between 0314 and 0337 UTC on the 23rd. This occurred during a period of weak wind strength shortly after the balloon had turned south back down the coast (Figure 5.3). During this sounding AMPS

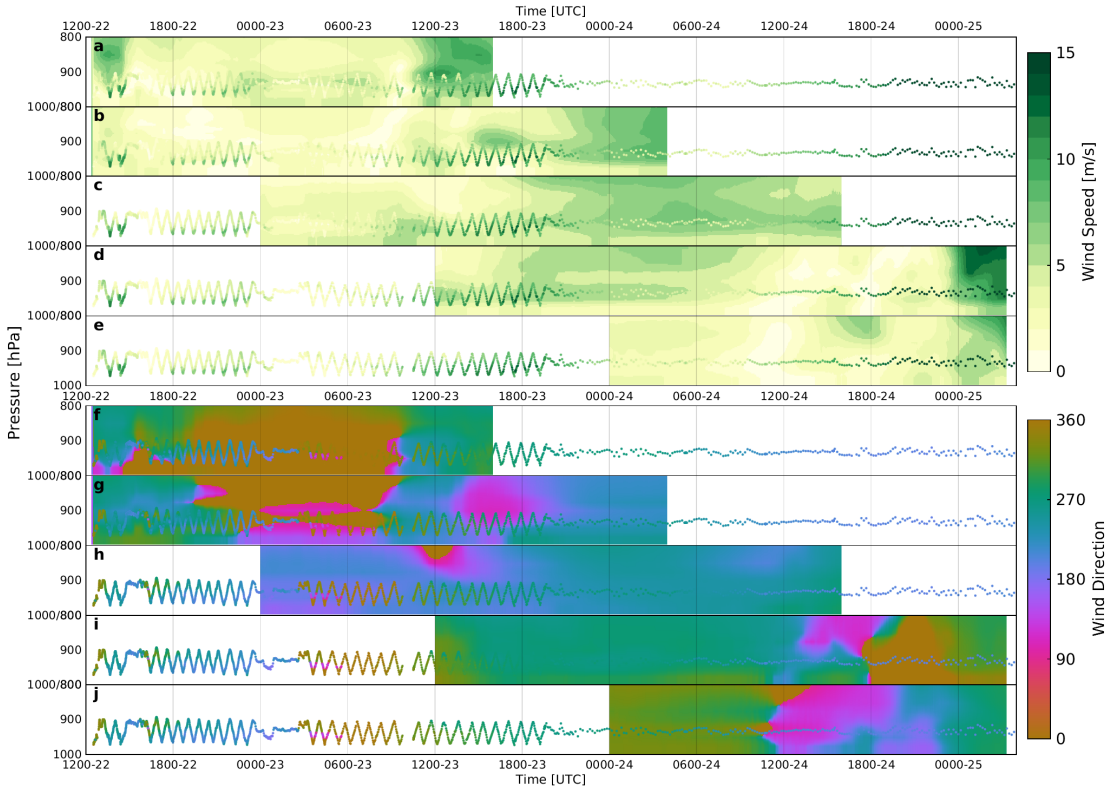

FIGURE 5.7: (a-e) Wind speed interpolated from the forecast by AMPS onto a pressure-time plane following the CMET flight-path. The individual panels represent consecutive AMPS forecasts. The overlying dots represent co-located CMET observations. (f-j) As for a-e but instead showing wind direction.

overestimated the specific humidity by about 0.02 kg/kg, but otherwise, the vertical gradient in humidity predicted by AMPS agrees well with the balloon observations at this time. The potential temperature in this location agrees well below 950 hPa. However, above this height, AMPS predicted a stronger lapse rate than was observed by the balloon, with potential temperatures diverging upwards.

The profiles between 1846 and 1914 UTC on the 23rd (Figure 5.9) show a comparatively larger bias between AMPS predictions and the CMET balloon observations. As for the earlier period, the specific humidity profile predicted by AMPS showed a similar vertical gradient to that observed by the CMET balloon. The potential temperatures predicted by AMPS show a 3 K bias near the surface with the two data sets gradually converging upwards meeting at 910 hPa.

Table 5.1 displays the mean values for AMPS model output and CMET observations for potential temperature, specific humidity and wind speed for a range of forecast issue times and dates. Table 5.1 also displays the Root Mean Squared Error (RMSE) between co-located and synchronous AMPS model output and CMET

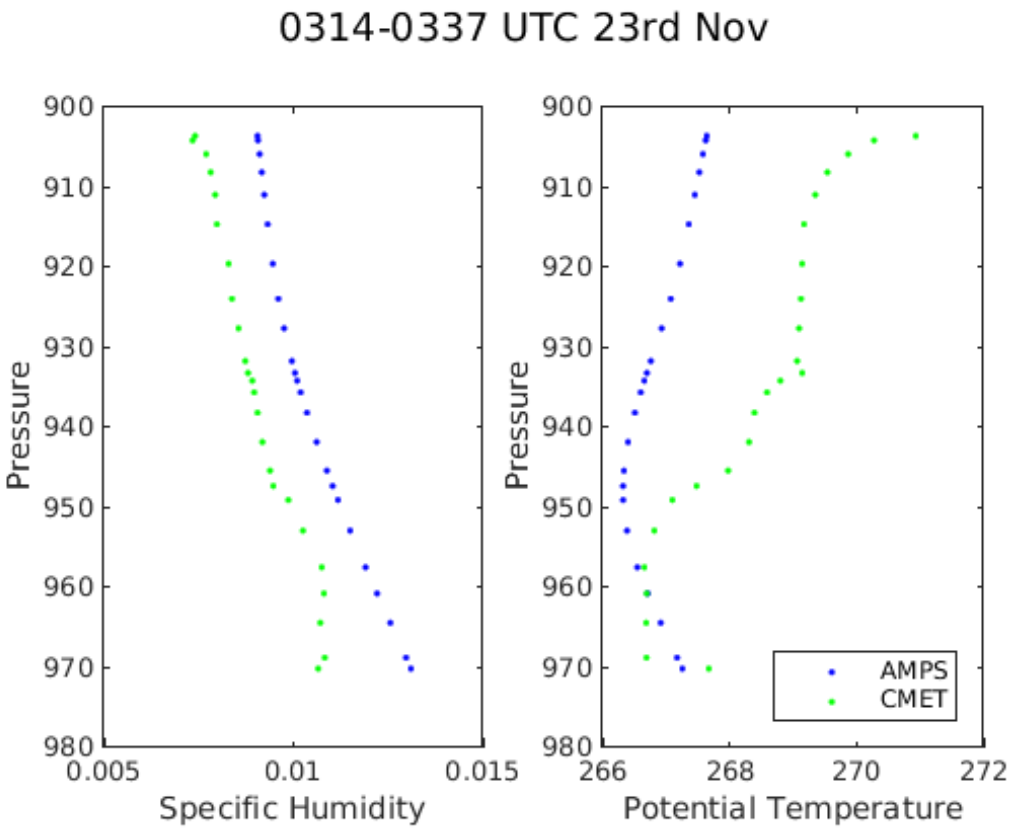

FIGURE 5.8: Specific humidity (left) and potential temperature (right) from a descending profile observed by the CMET balloon (green) compared with co-located AMPS forecast data (blue). The data from the AMPS forecast issued at 0000 UTC on the 23rd November was interpolated to the same spatiotemporal location as each CMET observation using cubic splines.

observations for potential temperature, specific humidity and wind speed averaged over the forecast period. Examination of Table 5.1 shows that the difference between the mean values from AMPS output and CMET observations is a minimum for the AMPS forecast issued at 0000 UTC on 23rd of November for wind speed. During this period, the bias for potential temperature was also very low, with the bias at 0000 UTC on the 22nd being slightly smaller. This is not true for the specific humidity field, but as detailed in Section 5.2.1 the absolute values of the relative humidity measurements made by the CMET balloon are quite uncertain, so we choose to ignore this fact. Given that this AMPS forecast displays a small bias in the potential temperature and wind speed and also represents the period where the CMET balloon is closest to the Ross Sea Polynya we focus on this forecast in the rest of this study. However, we note that the RMSE increases from the first to last forecast period in both potential temperature and specific humidity. Thus, there is clearly evidence of misrepresentation of some features of

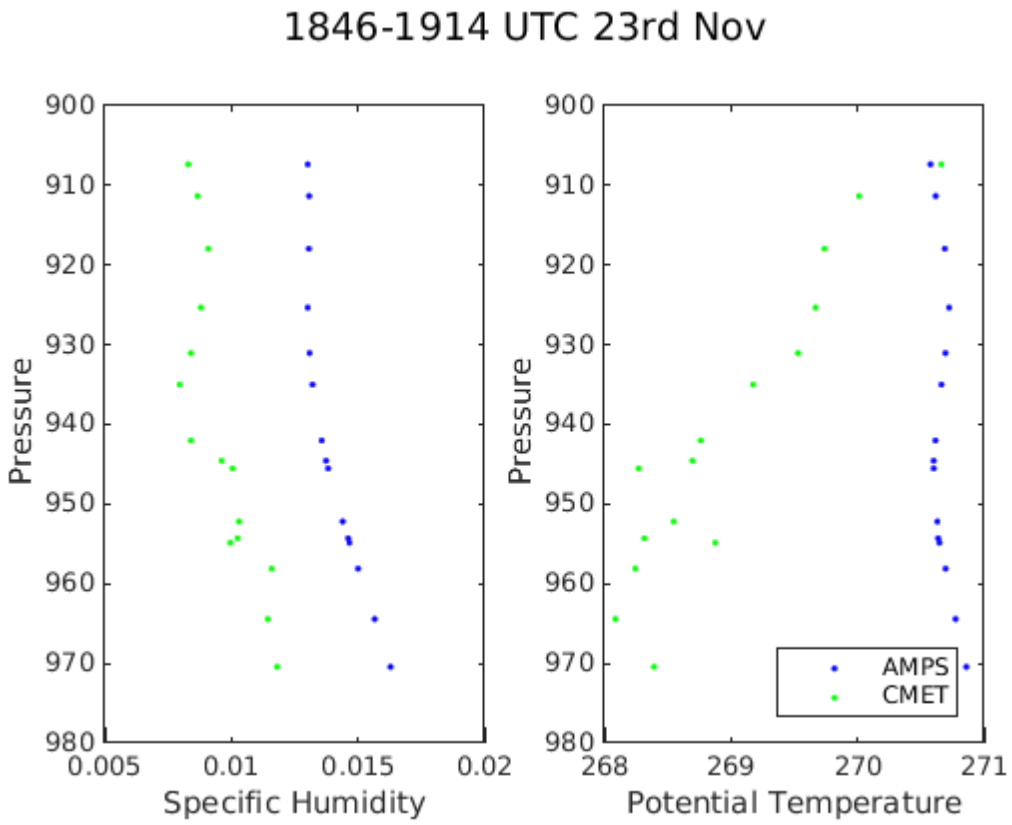

FIGURE 5.9: Specific humidity (left) and potential temperature (right) from a descending profile observed by the CMET balloon (green) compared with co-located AMPS forecast data (blue). The data from the AMPS forecast issued at 0000 UTC on the 23rd November was interpolated to the same spatiotemporal location as each CMET observation using cubic splines.

the atmospheric state in the AMPS forecast which must be borne in mind when interpreting future results. Though, we also note that this may partially reflect the fact that CMET stops vertical profiling in the latter portion of these periods which will impact the RMSE.

Examination of the differences between the CMET observations and the corresponding AMPS model output as a function of time also shows a significant variation across the various forecasts (see Figure 5.6 and 5.7). However, this is largely dominated by the change between the period where the balloon was profiling and after that period. This suggests that the biases between the CMET observations and the AMPS forecasts and the RMSE were strongly altitude dependent. In particular, we note that the potential temperatures had larger errors near the surface, as did the wind speeds. This may partially explain issues highlighted later on around disparities associated with sensible and latent heat fluxes.

TABLE 5.1: The mean values over the forecast period for the potential temperature, specific humidity and wind speed are shown for AMPS output and the CMET observations for a range of forecast start dates and times. The Root Mean Squared Errors (RMSE) between the AMPS output and the CMET observations are also displayed.

Forecast	Potential Temperature [K]			Specific Humidity [kg/kg]			Wind Speed [m/s]		
Date	CMET	AMPS	RMSE	CMET	AMPS	RMSE	CMET	AMPS	RMSE
0000-22	268.87	268.95	1.23	0.0088	0.0089	0.0021	5.81	3.74	11.01
1200-22	269.25	268.26	1.57	0.0090	0.0114	0.0037	6.25	3.41	9.61
0000-23	269.56	269.43	3.40	0.0103	0.0132	0.0040	6.76	5.18	8.96
1200-23	270.12	269.73	3.18	0.0112	0.0142	0.0052	8.92	4.38	6.00
0000-24	270.48	269.90	4.05	0.0123	0.0163	0.0053	10.66	2.63	7.36

Inspection of the AMPS predictions in Figure 5.6 reveal large variations between consecutive forecasts at the same time. For example, between 0000 UTC and 0600 UTC on the 23rd of November, a zone of high specific humidity was predicted above 900 hPa by the forecast issued at 1200 UTC on the 22nd. This moist area was not predicted by the forecasts issued at 0000 UTC on the 22nd and 23rd of November. Similarly, the forecast issued at 1200 UTC on the 22nd predicted a low level temperature inversion between 2000 UTC on the 22nd and 1500 UTC on the 23rd. This feature was not predicted by the forecasts immediately preceding and following.

AMPS performed comparatively more poorly when predicting wind speed and direction. Wind speed over the period from 1800 UTC on the 22nd to 0000 UTC on the 23rd proved particularly difficult for AMPS to model with CMET tending to provide higher wind speeds than AMPS, especially near the surface. From around 0800 UTC on the 23rd CMET also observed higher wind speeds than the AMPS forecast. Though, between 0000 UTC and 0800 UTC on the 23rd the AMPS forecast is very close to the values measured by CMET. During this time, the southerly winds observed by the CMET balloon weakened and gave way to strengthening northerly winds. Following the wind shift at 0300 UTC on the 23rd of November, the CMET balloon, which was close to the Antarctic coast, observed winds from a variable direction that were not accurately modelled by any of the AMPS forecasts. Within regions of varied topography, the quality of AMPS forecasts is known to be limited by the grid resolution, which likely explains this issue (Bromwich et al. 2005; Jolly et al. 2016). During the period examined in this paper, 0800 UTC on the 23rd of November to 0800 UTC on the 24th of November, the differences between the AMPS output and the CMET observations were close to the minimum observed (see Table 5.1).

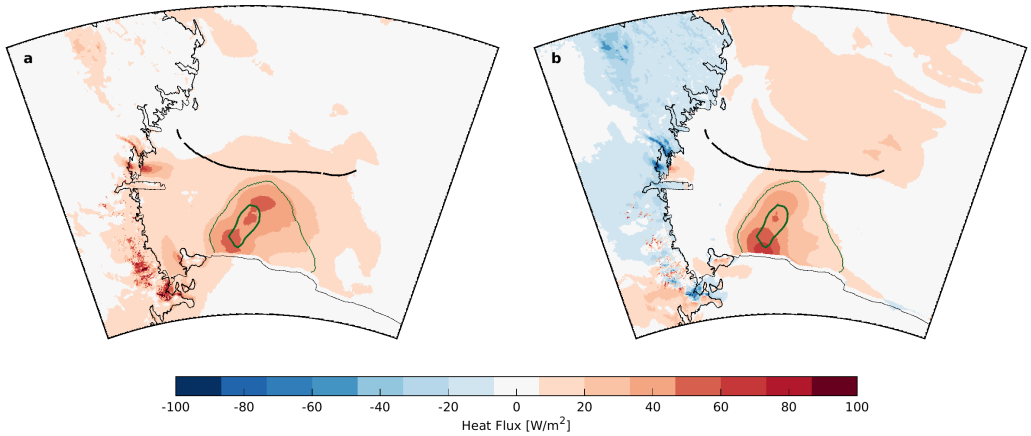

FIGURE 5.10: (a) Mean latent heat flux on the 23rd November 2017 from AMPS forecast issued at 0000 UTC on the 23rd Nov. (b) Mean sensible heat flux over the same time period. The black lines indicate the CMET flight path during this period. The thick and thin green lines indicate the 15% and 50% SIC isopleths respectively.

Figure 5.10 shows the mean latent and sensible heat fluxes over a 24 hour period, starting at 0800 UTC on the 23rd of November, predicted by the AMPS forecast issued at 0000 UTC on the 23rd of November (Figures 5.6 c and h). The thick and thin green contours in Figure 5.10 represent 15% and 50% SIC respectively, and indicate the position and size of the Ross Sea Polynya during this period. The strongest upward latent and sensible heat fluxes are predicted within both the Ross Sea and Terra Nova Bay polynyas. This indicates that AMPS modelled heat fluxes from the warm, open ocean into the atmosphere, and evaporation of sea water and consequent moisture fluxes. Sea water has a freezing point of approximately -1.8$^{\circ}C$, therefore open water provides a large source of heat to the cooler air above, the air temperature at the nearby Laurie II weather station being -8$^{\circ}C$. These latent and sensible heat fluxes were of moderate magnitude compared to values derived over polynya (**Fiedler2010**; Bourassa et al. 2013). We note that the comparison of the low–level wind speeds between the CMET observations and the AMPS output suggests that the AMPS low–level wind speeds are overestimates of the reality, given that the temperatures are rather similar this means that the sensible and latent heat fluxes estimated by AMPS are likely underestimates.

Figures 5.11a-c show the Lagrangian, Eulerian, and advection terms respectively

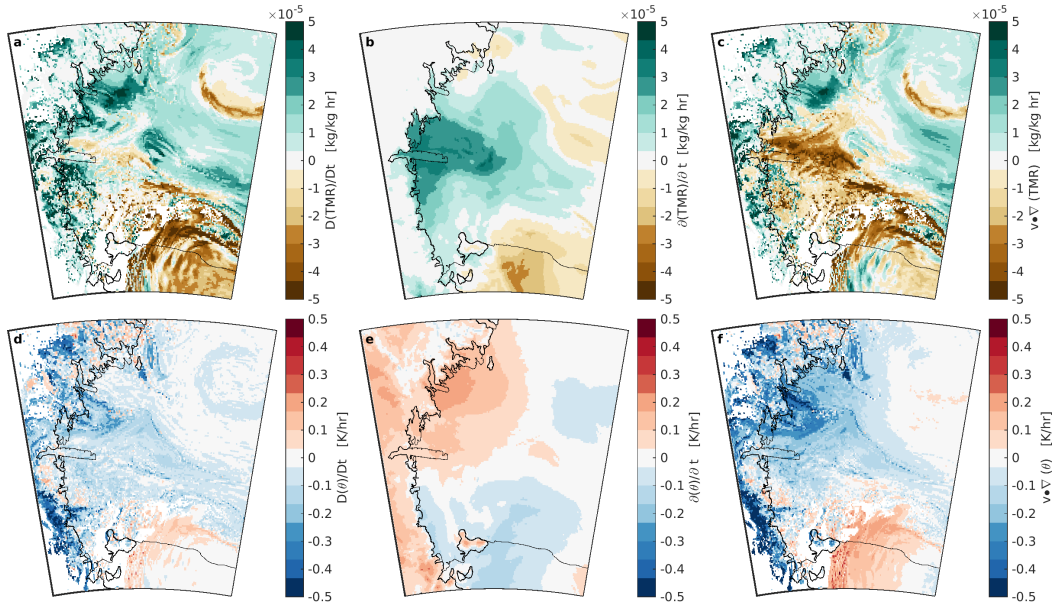

FIGURE 5.11: (*a*) Lagrangian derivative of the total mixing ratio over a 24 hour period starting at 0800 UTC on the 23rd of Nov 2017, calculated using trajectories launched 500 m above the surface. (*b*) Eulerian derivative of the total water mixing ratio at 500 m over the same 24 hour period. (*c*) The advection field of the total water mixing ratio over the same 24 hour period. (*d*) Lagrangian derivative of potential temperature over the same period. (*e*) Eulerian derivative of potential temperature at 500 m over the same 24 hour period. (*f*) The advection field for potential temperature over the same 24 hour period.

for the total water mixing ratio (TWMR) predicted by AMPS over a 24 hour period, starting at 0800 UTC on the 23rd of November, on a surface 500 m above the ground. These derivatives are therefore centred upon 2000 UTC on the 23rd of November. We selected the 500 m level because it relates to the altitude that the CMET balloon travels after it stopped vertical profiling because of low battery power. The Lagrangian derivative, calculated as the difference over time in the given variable between the ends of the forward and backward trajectories, represents the rate of change that would experienced by a free parcel of air. The Eulerian derivative, calculated as the difference in the given variable over the same period of time at a fixed location, represents the rate of change that a stationary observer would observe. The advection term, calculated as the difference of the Eulerian and Lagrangian derivatives, describes the contribution of air motion on the local rate of change of the given variable. We note that the trajectories used to derive the Lagrangian derivative were calculated within the AMPS domain 3 field, however some trajectories travelled beyond the spatial bounds of this domain and were therefore not able to be continued. This causes some regions of

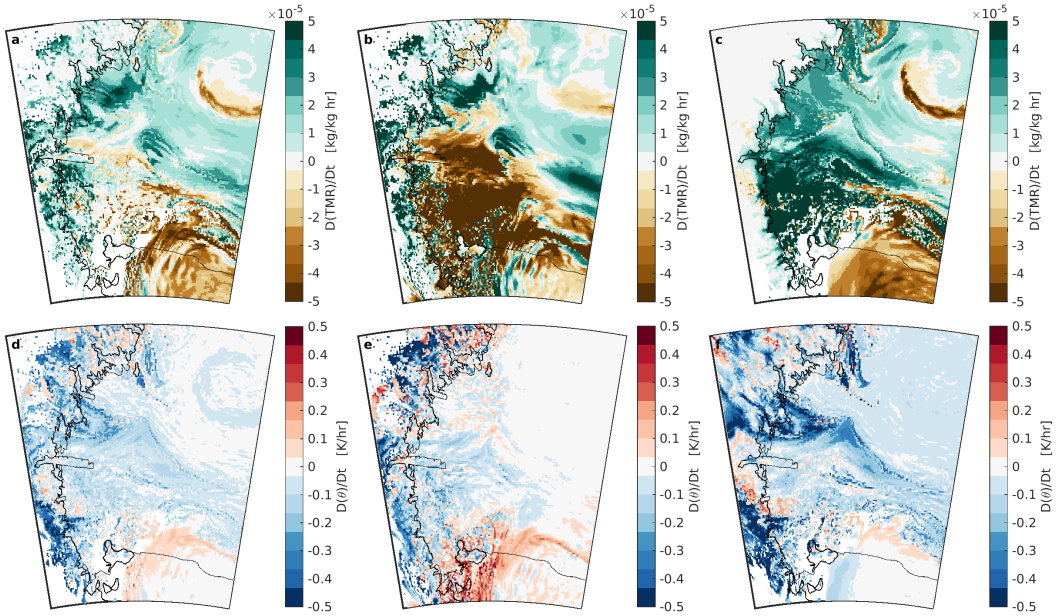

FIGURE 5.12: (*a*) Lagrangian derivative of the total mixing ratio over a 24 hour period starting at 0800 UTC on the 23rd of Nov 2017, calculated using trajectories launched 500 m above the surface. (*b*) The forward component of the TWMR Lagrangian derivative. (*c*) The backward component of the TWMR Lagrangian derivative. (*d*) Lagrangian derivative of potential temperature over the same period. (*e*) The forward component of the potential temperature Lagrangian derivative. (*f*) The backward component of the potential temperature Lagrangian derivative.

the Lagrangian derivative field to be undefined (Figure 5.11a). These are mostly over the Trans-Antarctic Mountains, where back trajectories follow fast-moving, directionally consistent streamlines towards the edge of the field, allowing air parcels to cover a large distance in a short time.

TWMR is defined as the sum of the mixing ratios for water vapour, cloud water, cloud ice, rain, and snow. These mixing ratios are all defined within AMPS. The Lagrangian derivative of the total water mixing ratio (Figure 5.11a) shows that air passing over the Southern Ross Sea and over the Ross Ice Shelf became drier, while air passing over more northern parts of the Ross Sea and the Trans-Antarctic Mountains became moister.

A thin band of air which has lost moisture is observable in figure 5.11a near the anti-cyclone approximately 400 km to the north of the RSP. In this location, the Eulerian derivative does not show a corresponding feature. Thus the advection term in this location opposed the Lagrangian derivative indicating that moisture

was advected into this region. The Eulerian derivative for the same altitude surface and time period shows an increase in local moisture in an area surrounding the Drygalski Ice Tongue. However, air parcels passing over this region did not moisten, as shown by the varied signal in the Lagrangian derivative (Fig 5.11a). Therefore this local moistening must be driven by advection towards the vicinity of the Drygalski Ice Tongue. This is demonstrated by the strong negative advection term over the Drygalski ice tongue. We note that the initial level of humidity in this region was low initially allowing for increased net moisture transport towards this region. An area with a negative Lagrangian derivative exists over the edge of the Ross Ice Shelf which is counter to our expectation based on the latent heat flux displayed in Figure 5.10. The resultant advection term (Figure 5.11c) for this period shows that grid cells over the Southern Ross Sea acted as a moisture sink during this period, with scattered southern regions and a larger area to the north providing a moisture source.

The Eulerian derivative, Lagrangian derivative, and the advection term for potential temperature at the same altitude and time period are shown in Figures 5.11d-f. The Lagrangian derivative (Figure 5.11d) shows air passing over the edge of the Ross Ice Shelf and the RSP was weakly warming, while air passing over the rest of the Ross Sea was weakly cooling. Air passing over the Trans-Antarctic Mountains was dominated by cooling. Figure 5.11e shows the Eulerian derivative of potential temperature for this same altitude and time period. Warming was observed over the Trans-Antarctic Mountains and the north-western coast of the Ross Sea, while a cooling trend was observed over the Ross Ice Self and the southern Ross Sea. The resultant advection (Figure5.11f) term is spatially very similar to the Lagrangian derivative, with the area over the edge of the Ross Ice Shelf and RSP providing a source of heating and the rest of the mapped area acting as a heat sink. These are clear signs that a significantly sized air mass, approximately 200km by 100km, was impacted by heat fluxes from the RSP, as might be expected based on inspection of Figure 5.10. Note that the size of the air mass impacted by the surface fluxes was estimated from the trajectories and the resultant derivatives displayed in Figure 5.11.

5.4 Discussion

From 1800 UTC on the 22nd of November until 1200 UTC on the 23rd of November, AMPS predictions for wind direction performed relatively poorly (Figures

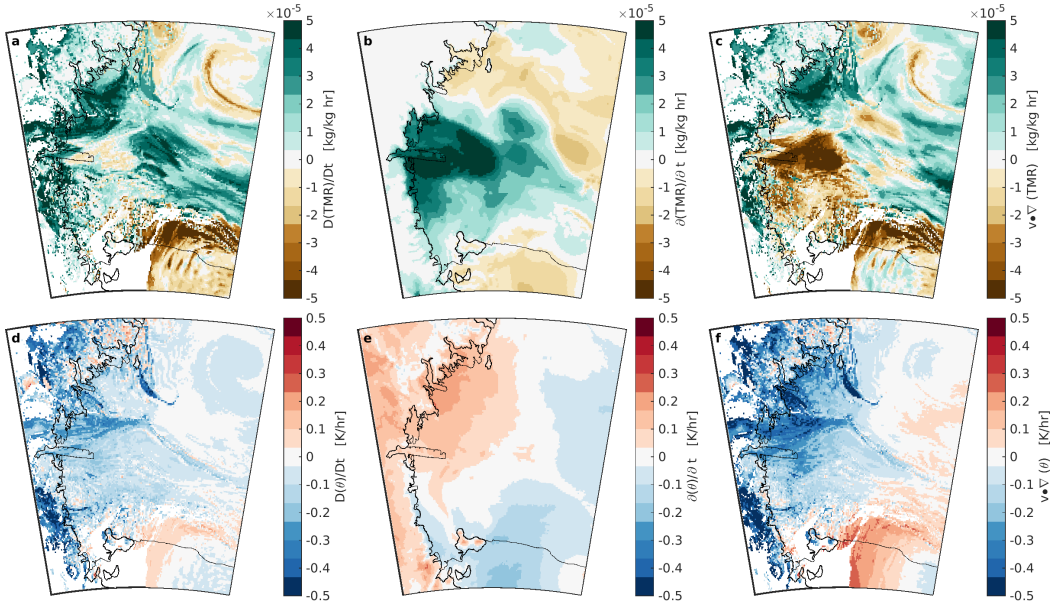

FIGURE 5.13: (*a*) Lagrangian derivative of the total water mixing ratio over a 24 hour period starting at 0800 UTC on the 23rd of Nov 2017, calculated using trajectories launched 250 m above the surface. (*b*) Eulerian derivative of the total water mixing ratio at 250 m over the same 24 hour period. (*c*) The advection field of the total water mixing ratio over a the same 24 hour period. (*d*) Lagrangian derivative of potential temperature over the same period. (*e*) Eulerian derivative of potential temperature at 250 m over the same 24 hour period. (*f*) The advection field for potential temperature over the same 24 hour period.

5.7f-h). AMPS predicted several discontinuities in wind direction, and consecutive forecasts did not agree on wind direction. During this period, AMPS consistently predicted weak wind speeds (Figures 5.7a-c). The CMET balloon observed variable wind directions and wind speeds, suggesting that this period lacked significant synoptic scale forcing in terms of a pressure gradient because of the combination of the anticyclone and cyclone. Though, we note that the differences between the AMPS forecast wind speeds and the CMET observations were worse nearer the surface and better at higher altitudes. Initially the balloon travelled northwards, between 0000 and 0600 UTC on the 23rd of November the balloon was almost stationary, and then began travelling southwards. During this time the observed wind direction was variable, with a strong vertical gradient in wind direction observed. A similar pattern also being observed in the wind speed. Wind direction is difficult to accurately predict when wind speeds are low as a small magnitude change in the wind vector can cause a large change in direction (Jolly et al. 2016). The balloon was also relatively close to the significant topography of Ross Island during this period, and AMPS, as well as other similar models,

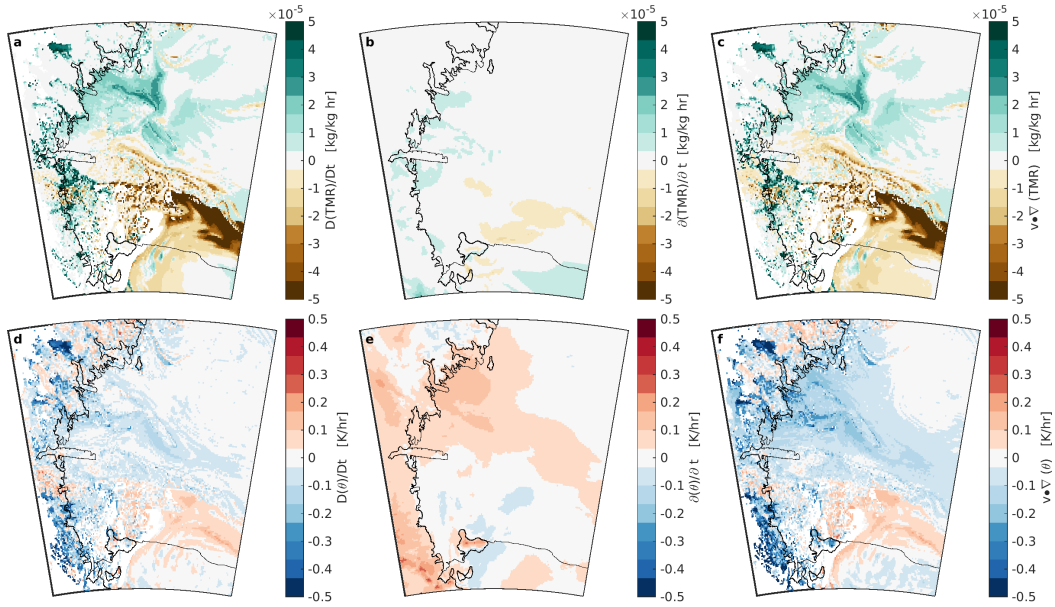

FIGURE 5.14: (*a*) Lagrangian derivative of the total water mixing ratio over a 24 hour period starting at 0800 UTC on the 23rd of Nov 2017, calculated using trajectories launched 1000 m above the surface. (*b*) Eulerian derivative of the total water mixing ratio at 1000 m over the same 24 hour period. (*c*) The advection field of the total water mixing ratio over a the same 24 hour period. (*d*) Lagrangian derivative of potential temperature over the same period. (*e*) Eulerian derivative of potential temperature at 1000 m over the same 24 hour period. (*f*) The advection field for potential temperature over the same 24 hour period.

are known to have difficulty modelling the effects of complex terrain (Bromwich et al. 2005; Jolly et al. 2016).

Observations made by the CMET balloon often fell between the values predicted by the different AMPS forecasts. Particularly in the wind direction field, regions where consecutive AMPS forecasts disagreed often coincided with regions where AMPS had its largest anomalies from the CMET observations. This reinforces the idea that anomalies between consecutive AMPS forecasts may be used as a indicator of the accuracy of AMPS forecast in that region.

AMPS utilises near-real-time ice and snow extent (NISE) sea ice concentration data as an input (Brodzik and Stewart 2016). These data were provided at a 25 km horizontal grid resolution, and have a temporal resolution of 24 hours. Whilst this spatial resolution is significantly smaller than the spatial extent of the Ross Sea Polynya, it is comparable to that of the McMurdo and Terra Nova Bay polynyas. In Figure 5.4a the minimum sea ice concentration within these polynyas is greater than 50%. However sub-pixel sized areas of open water were observed visually

during field operations within Terra Nova Bay. These areas are not identified by the NISE product as they are averaged out over the coarse resolution grid. This, in addition to the low temporal resolution of the NISE data set, will limit the ability of AMPS to model the influence these regions have on the atmosphere above (Batrak and Müller 2018). We therefore suggest that the influence of the polynya derived from AMPS should be considered to be a low estimate particularly when the biases in the AMPS low-level winds are considered.

The Ross Sea Polynya and surrounding regions were shown to provide a local heat source associated with advected warm air linked to increases in the potential temperature in Figure 5.11f. Lagrangian derivatives were calculated over a 24 hour period, which removed the diurnal cycle temperature but caused a loss of coherent structure in the resultant field. If a small, localised heat source existed over the 24 hour period, air in regions immediately upwind and downwind of the source, regions of open water in this case, would pass over this region and also register a heat gain. This effect is highlighted in figure 5.12 which shows the forward and backward components that make up the total Lagrangian term. This effect also flows through to the advection term, producing positive values over the Ross Ice Shelf in figure 5.11f. In this case, the Ross Sea Polynya acted as a source of heat for the atmosphere, causing an increase in potential temperature, but given the averaging over the 24 hour period a larger region was impacted by this heat source.

The Lagrangian and Eulerian derivatives for potential temperature (Figure 5.11d-e) generally oppose each other, particularly in areas surrounding the Ross Sea Polynya. The Eulerian derivative indicates that air over the RSP cooled over the period of concern, whilst the Lagrangian derivative indicated the potential temperature of air passing over the RSP increased. This highlights the importance of considering both the Lagrangian and Eulerian derivatives, as simple inspection of the Eulerian derivative would lead to the conclusion that the RSP did not provide a significant source of heat and caused the air above to cool. But, when the Lagrangian derivative is also considered, it is found that air passing over the RSP warmed over the same period and the RSP supplied heat to the atmosphere. This indicates that the cooling found in the Eulerian derivative (Figure 5.11e) is caused by a cool body of air being advected over the RSP, replacing a warmer body of air. Thus, the RSP was observed to provide heat to the above atmosphere over the studied time period. We can identify that the polynya in the region have a significant and near continuous impact on the atmosphere during this period of the year.

The RSP in this period appears to have been connected to a Ross Ice Shelf Air Stream event, these events occur most frequently in the austral winter (Coggins et al. 2014). Thus, we speculate that the RSP could be a significant source of local heating in the winter during and after RAS events, this being particularly significant because the temperature differential between the ocean and the overlying atmosphere will be larger in winter resulting in a larger heat flux. In addition, work detailed in Coggins and McDonald (2015) suggests that the strengthening of the Amundsen Sea Low has likely increased the frequency of RAS events over the Ross Sea region. This suggests that there may be significant trends in the atmosphere-ocean heat fluxes over the RSP, which may have in turn impacted sea ice production.

The latent heat provided by the RSP (Figure 5.10a) indicates potential for evaporation of water within this region, thus providing an upward moisture flux from the ocean to the atmosphere. However, this effect was not represented in Figure 5.11a-c, which show the derivatives of total water mixing ratio over the Ross Sea at 500ṁ. We speculate that this suggests that the evaporated moisture is not able to reach this altitude. To examine this hypothesis we also created derivative fields at 250ṁ and 1000ṁ (Figures 5.13, 5.14) these reveal similar results, with the 250ṁ showing more similarities with the 500ṁ result that the 1000ṁ. The main difference from the 500ṁ result in these cases is the larger magnitudes of change being observed at the lower, and therefore warmer and generally more moist, altitude. This potentially highlights the limited ability for moisture to mix vertically to 250ṁ and above in the AMPS model associated with this event. It also potentially suggests an inconsistency in the representation of humidity with the parameterisation of latent heat flux (Figure 5.10).

5.5 Conclusions

This work presents meteorological observations made in situ over the Ross Sea in November using a long-duration CMET balloon. CMET observations from a single flight lasting over 70 hours are compared with forecasts made by AMPS, an operational version of the Polar WRF model used to support Antarctic operations. During this flight, the balloon made repeated soundings through the marine boundary layer, and flew near both the Terra Nova and Ross Sea Polynyas.

AMPS predictions of atmospheric conditions generally compared favourably with CMET observations. Discrepancies were found to be most frequent in the wind direction, particularly during periods of weaker winds and time periods

surrounding changes in wind direction. CMET observations generally fell within the range of variability found between consecutive AMPS forecasts, indicating that the forecasts bound the observations.

AMPS SIC and surface heat flux predictions indicated that the Ross Sea Polynya was open and provided a source of heat and moisture to the atmosphere during the period of the CMET measurements. Calculation of the Lagrangian and Eulerian derivatives, which also allowed the advection of the potential temperature field at 500 m above ground to be derived, allow the influence of the RSP on the air mass sampled by the CMET balloon to be examined. To the extent of the authors knowledge, analysis of this type has never been done before. This analysis indicates that the area over the Ross Sea Polynya provided a source of heat and that the influence of this heat source conservatively covered a region of 200 km by 100 km in this case. However, calculation of a total water mixing ratio advection field indicated that AMPS did not predict this area to act as a moisture source above 250 m. Evidence of diabatic heating at these levels was observed in the potential temperature derivatives. We also showed that this case was relatively representative of this time of year and the good correspondence between AMPS and the CMET balloons suggest that our derivative calculation methodology might be more widely useful in understanding the influence of polynya on the local atmospheric environment.

Chapter 6

Large Trajectory Ensembles for Understanding Moisture Transport and Resultant Precipitation Over the Ross Ice Shelf, Antarctica

Abstract

Air parcel origins for a site over the Ross Ice Shelf are studied using Lagrangian back trajectories. Over 50,000 Lagrangian back trajectories were systematically calculated from ERA-Interim reanalysis wind fields. Spatial distributions of trajectory origin locations between 1979 and 2016 are examined. Specific precipitation events identified from the ERA-Interim reanalysis are shown to have particular pathways and moisture sources. We find that during periods of precipitation, air parcels over the Ross Ice Shelf originate from the Ross and Amundsen Seas more frequently. In contrast, during dry periods over the Ross Ice Shelf, air parcels originate more frequently from the Bellingshausen and Weddell Seas, with trajectory pathways frequently crossing over continental Antarctica. Reanalysis humidity data along each trajectory is also considered, allowing a more comprehensive identification of the origin of moist air, as well as identifying a representative 'residence time' of moisture. We find that a period of 5 days is most suitable for our analysis. Trajectories with similar locations and humidities at origin are found to have vastly different humidity upon arrival over the Ross Ice Shelf depending on the pathway the trajectory followed. This indicates that conditions at a specific location are not sufficient for understanding the moisture transport of a specific trajectory.

6.1 Introduction

The break-up of ice shelves leads to rapid thinning of tributary glaciers (Kuipers Munneke et al. 2014). West Antarctica and the Antarctic Peninsula have shown significant warming trends with resulting break-up of several ice shelves and thinning of glaciers over previous decades. It is not clear whether similar trends exist in East Antarctica (Kuipers Munneke et al. 2014; Martín-Español et al. 2016; Turner et al. 2007). As the RIS is the largest ice shelf in Antarctica, understanding the surface mass balance (SMB) within this region is important for predicting future climate change and sea level rise contributions from this region.

Measurements of the SMB on the RIS are scarce, with the first set of large scale measurements being made by Crary et al. (1962), with subsequent measurements being published by Clausen and Dansgaard (1977), Heap and Rundle (1971), Bentley (1990), and Favier et al. (2013). These studies yielded varying results, with discrepancies likely due to differences in the geographical regions sampled along with differing temporal scales and periods of the various studies.

The current study follows on from field work performed during the 2015/2016 summer season. A 16 m firn core was drilled at a site 80.7° S 174.5° E, referred to as HWD2, at which a hot water drilling project occurred in the 2017-2018 Austral summer. Oxygen and Deuterium isotope analysis was performed on the core, allowing a 30-year record of snow accumulation to be produced. The derived snow accumulation record differs significantly from that hindcast by reanalysis (Arnold 2016).

We utilise Lagrangian back trajectory analysis to analyse the origins of precipitation at HWD2. Lagrangian back trajectories are frequently used to approximate the origins and path for parcels of air (Scarchilli et al. 2011; Sinclair et al. 2010). Understanding the origins of an air mass can allow for improved understanding of how distant climatological influences effect changing local climate. Trajectory studies are often used to aid the interpretation of isotopic data obtained from ice cores. Moisture of differing origin locations often display differences in the relative abundances of various isotopes dependant on complex regional and local factors. By comparing isotope records and trajectory frequencies, certain pathways can be associated with distinct isotope abundances (Markle et al. 2012; Neff and Bertler 2015).

Many authors apply a k-means clustering algorithm to the output of Lagrangian back trajectories with the goal of identifying representative pathways (Dittmann et al. 2016; Genthon et al. 2016; Hafner et al. 2007; Schlosser et al. 2008; Sinclair

et al. 2013). Clustering results in several characteristic pathways, each representing an individual cluster of similar trajectories. The dimensionality and therefore complexity of the data set is drastically reduced. However, clustering can sometimes hide information by grouping two or more physically different pathways. Due to this we investigate alternate methods of back trajectory analysis using origin point distributions to understand the large number of trajectories that we analyse.

Sodemann and Stohl (2009) utilise a Lagrangian moisture source diagnostic to analyse the seasonality of moisture sources for Antarctica. Trajectories are propagated backwards from precipitation events over Antarctica identified within the European Centre for Medium-Range Weather Forecasts analyses. Instead of using a fixed propagation time trajectories were propagated until a evaporation event is observed. Evaporation and precipitation events were identified using thresholds for change in the specific humidity field. Sodemann and Stohl (2009) find that for the majority of sites over Antarctica that moisture originated at a mean longitude west of the precipitation site, with a notable exception of the Ross Sea, which was found to have a mean origin longitude of 120° - 180° W. The mean moisture source latitude was also found to vary seasonally with sources originating from further north during the winter months. Stohl and Sodemann (2010) use similar methodology to analyse general transport properties of Antarctic air. Stohl and Sodemann (2010) find that the lower 100 m of the troposphere over the Ross Ice Shelf is the region of Antarctica most isolated from the ocean, with air spending a mean time of 16 consecutive days south of 70° S in the summer and 9 days in the winter. This isolation diminishes at higher altitudes, where katabatic flows are less dominant.

The RIS has an area of 487000 km^2 and is largely devoid of topographical features larger than about 10 m. To the west lies the Trans-Antarctic mountains, rising from sea level to the East Antarctic ice sheet at an altitude of 2500 m, with several peaks exceeding 4000 m, forming a significant barrier to airflow. The eastern edge of the RIS borders West Antarctica. This boundary has a less steep gradient, smoothly rising to the West Antarctic Ice Sheet. The northern edge of the RIS meets the Ross Sea, an area of water that is covered in a layer of sea ice between the months of April and November.

Cool, dense air near the surface on both the East and West Antarctic Ice Sheets contributes to katabatic winds, which flow onto the RIS. This along with synoptic scale pressure gradients, cause a drainage flow across the flat RIS near the

surface, resulting in a prevailing southerly flow. These drainage flows are often enhanced by geostrophic flows caused by cyclones over and adjacent to the Ross Sea. In particular, this promotes the prevailing drainage flows to follow the barrier of the Trans-Antarctic Mountains, leading to strong southerly flows throughout the western half of the RIS (Coggins et al. 2014; Parish et al. 2006). It is also noteworthy that the Antarctic coastal region is one of the most active areas of synoptic-scale cyclonic storms in the Southern Hemisphere (Coggins and McDonald 2015; Hoskins and Hodges 2005).

6.2 Data and Methods

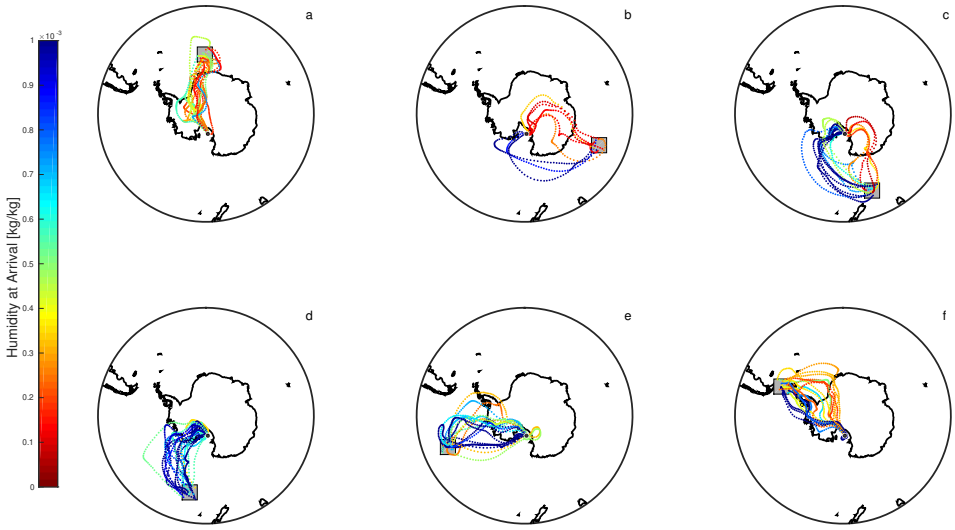

FIGURE 6.1: Sample back trajectories whose origin points fell within the grey box indicated within each panel. The colour of each individual trajectory indicates the humidity at arrival at HWD2 for that trajectory.

Lagrangian back trajectories used in this study were calculated from ERA-Interim (ERA) re-analysis wind data (Dee et al. 2011). ERA provides a range of atmospheric variables at a 6-hourly temporal resolution, over a global $0.75^\circ \times 0.75^\circ$ grid at 37 different pressure levels.

A starting position and time was defined for each back trajectory, this was propagated backward through time from the HWD2 site. For each time step, meridional, zonal, and vertical wind components were interpolated using cubic splines to the current location and time of each trajectory. The location of each trajectory at the preceding time step was then calculated using a fourth order Runge-Kutta

method. The trajectories are calculated in a local 3D Cartesian coordinate system and then converted back to a latitude, longitude, and pressure coordinate, with the scheme used being very similar to that detailed in Smith and McDonald (2014) and Friedrich et al. (2017).

A time step of 1 hour was used for trajectory propagation; a smaller time step would provide limited improvements in accuracy due to the larger ERA time step of 6 hours. Trajectories were calculated with a length of 10 days. Beyond this length, the cumulative errors due to the inaccuracies of the ERA-Interim reanalysis and the numerical methods used become large (Friedrich et al. 2017; Smith and McDonald 2014). Trajectories were launched every 6 hours at the latitude and longitude of HWD2 (80.7° S 174.5° E), at both the 850 hPa and 500 hPa pressure levels. They were calculated for each six hourly time step from 1979 until 2016, providing over 50,000 trajectories at each arrival level.

Figure 6.1 shows a sample of the trajectories calculated, with those whose origins lie within the grey boxes shown in each panel. The colour of each trajectory indicates the humidity upon arrival at HWD2, and will be interpreted in further detail in Section 6.3.

In order to understand the moisture and accumulation associated with each trajectory, we utilise ERA-Interim specific humidity and precipitation fields (Dee et al. 2011). The humidities were interpolated to the position of each trajectory at each time-step, allowing the moisture carried by each trajectory to be identified. The precipitation was interpolated to the geographic location of HWD2 using cubic splines, allowing a time series of precipitation over HWD2 to be calculated. Cohen and Dean (2013) compare snow accumulation measured using acoustic depth gauges at 8 automatic weather stations on the Ross Ice Shelf with ERA-Interim and other re-analyses. ERA-Interim was found to compare favourably in comparison to the other reanalysis investigated.

6.3 Results

6.3.1 Origin distributions

The distribution of origins for 5 day back trajectories are shown in figure 6.2a for trajectories launched at the 850 hPa arrival pressure level above the HWD2 site (indicated by the black dot). The 5 day back trajectories most frequently originate from the boundary between East and West Antarctica, with the highest density occurring in a small region covering the Trans-Antarctic Mountains

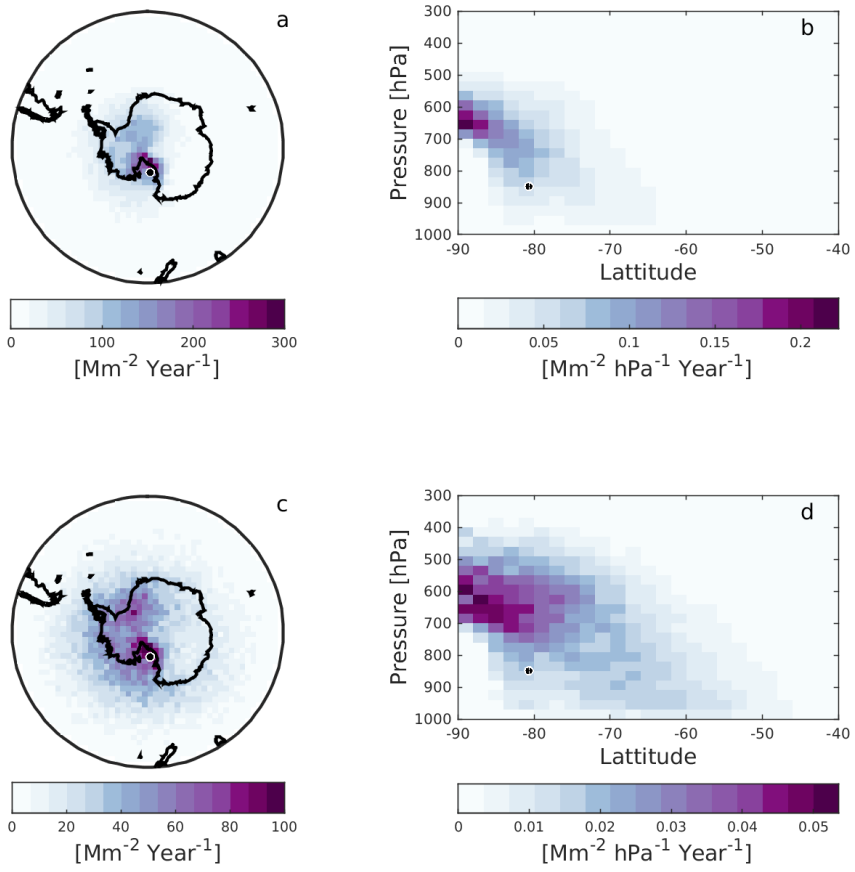

FIGURE 6.2: (a) Density of 5 day back trajectory end point distribution for trajectories launched from HWD2, indicated by a black dot. (b) Density of 5 day endpoints plotted in the latitude pressure plane. (c-d) As for (a-b) however using 10 day trajectory endpoints.

south of HWD2. The majority of the origins reside over continental Antarctica, with only a few occurring over the Ross, Amundsen, Bellinghausen, and Weddell Seas. Trajectories that originate over the continent are unlikely to carry the necessary moisture required to cause precipitation, as air over the continent is normally cool and dry.

Figure 6.2b shows the zonal mean of origin density. The majority of origin points fell south of the HWD2 arrival site (indicated by the black dot). Furthermore air masses predominately originated from a pressure level lower than the 850 hPa arrival level.

Origin points that fell near the pole generally fell at a low pressure level because much of the southern latitudes are occupied by the high Antarctic Plateau,

constraining trajectories to higher altitudes. Air parcels that pass over the high plateau will cool as they rise over this high topographical barrier, causing the condensation of water droplets or the formation of ice and precipitation this will limit the amount of moisture that can be delivered to HWD2.

Figures 6.2c-d show results using back trajectories with 10 day lengths. Generally these distributions are spread over a greater area than those of the 5 day back trajectories as the increased period of travel has allowed the air parcels to disperse further. In figure 6.2c, trajectories often reach latitudes as far north as 45° S. As with the five day back trajectories (Figure 6.2a), the majority of the 10 day origin points occur over an area between East and West Antarctica. However, the 10 day back trajectories also show an increased origin point density in the Weddell Sea sector and areas surrounding the coasts of West Antarctica.

The zonal distribution for 10 day trajectory lengths (Figure 6.2d) is also broadened, but otherwise remains similar to that of the 5 day trajectory lengths (Figure 6.2b). Due to the increased travel time, 10 day trajectories are able to reach considerably further north than their 5 day counterparts. The trajectories which travel from furthest north lie over open ocean and are therefore not constrained by topography; this allows these trajectories to reach the highest pressure levels (lowest altitude) and be in contact with open water more frequently.

6.3.2 Precipitation composites

We now consider the anomaly in the back trajectory end point density for periods associated with precipitation, thereby identifying the most important trajectories in terms of accumulation at the HWD2 site. Each day was classified based on the ERA precipitation rate at HWD2, using a threshold of 0.1 $mm\ day^{-1}$. Composite trajectory origin point distributions were then produced, using all trajectories arriving at HWD2 on days where precipitation exceeded the 0.1 $mm\ day^{-1}$ threshold. The differences between these normalised composite distributions and the total distributions (Figure 6.2) were calculated, producing anomalies in the origin point distributions (Figure 6.3).

Figure 6.3a shows the anomalous origin point distribution, calculated with a trajectory length of 5 days; positive values indicate higher origin point density during periods of precipitation. This reveals an increase in the density of origin points over the RIS, as well as over the Ross and Amundsen sectors of the Southern Ocean. A decrease in the density is observed over Dronning Maud land, as well as over the Weddell and King Hakon VII Seas. This demonstrates that

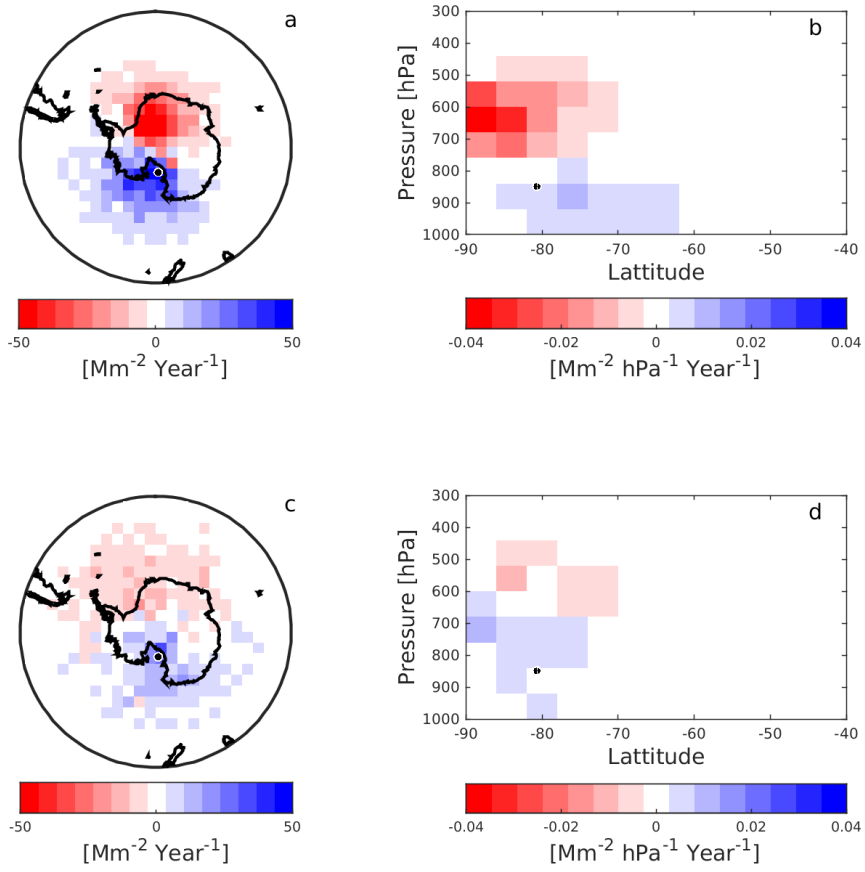

FIGURE 6.3: (a) Anomaly from mean in 5 day back trajectory origin distribution for trajectories propagated backwards from HWD2 on days where precipitation was greater than 0.1 mm. Positive values indicate greater origin point density during periods of precipitation. (b) Anomaly of 5 day origin locations plotted in the latitude pressure plane. (c-d) As for (a-b) however using 10 day trajectories.

for periods of precipitation at HWD2, trajectories are more likely to come from the adjacent seas and less likely to come from the dry continent or distant seas. Trajectories with these distant origins likely followed pathways that would have crossed over high terrain to reach HWD2.

Figure 6.3b shows zonal mean anomalies in the latitude-pressure plane. Negative anomalies exist above 750 hPa and south of 70° S, with the maximum negative anomalies occurring near the pole at 650 hPa. Weak positive anomalies are found beneath 800 hPa and south of 60° S. This indicates the dependence of precipitation on the vertical position of the origin point. Trajectories coming from higher

altitudes represent cooler air masses carrying lower amounts of precipitable water.

The composites made using 10 day length back trajectories, figure 6.3c-d, display results similar to that using 5 day periods, figure 6.3a-b, however the magnitude of these anomalies are much less pronounced. These lower magnitudes indicate that 10 day origins have a weaker influence on the probability of a precipitation event at HWD2 compared to that of a 5 day trajectory length. The observed anomalies are also distributed more widely than those of 5 day trajectories, which is consistent with the wider spread of the origin point density expected from these longer trajectories. While the 5 day trajectory anomalies in the latitude-pressure plane (Figure 6.3b) had only shown positive values below the 750 hPa level and predominately north of 80° S, the 10 day anomalies show positive values near the pole and above the 850 hPa level (Figure 6.3d). However, the positive anomalies still remain at a greater pressure level than the negative anomaly, although both cover similar latitudes.

6.3.3 Origin and arrival humidities

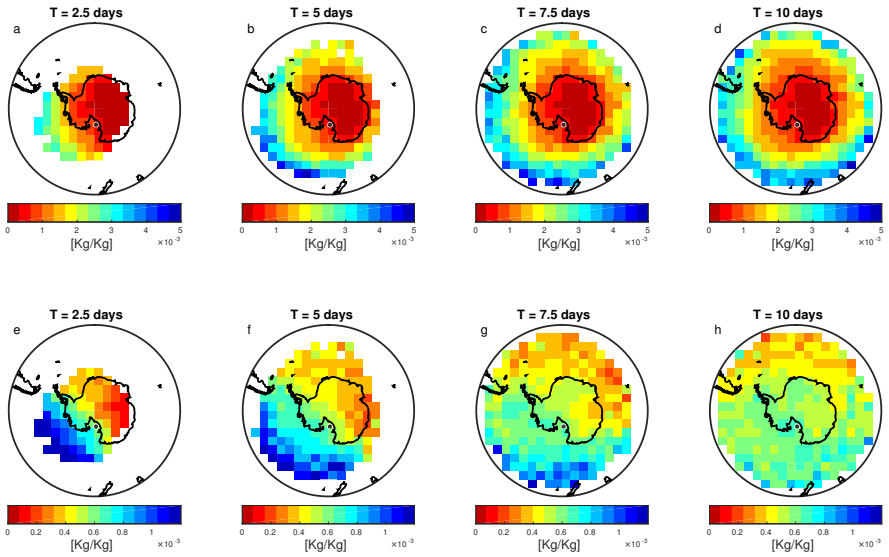

FIGURE 6.4: (a-d) Humidity at origin location for Lagrangian back trajectories of varying lengths. (e-h) Arrival humidity for trajectories propagated backwards from HWD2, plotted as a function of trajectory origin location at varying trajectory lengths.

Using ERA-Interim specific humidity data, the humidity along each trajectory path was interpolated form the 4D ERA-Interim grid to the trajectory position for

each time-step. We define the humidity at arrival as the humidity each trajectory represents at the time that it arrived at the back trajectory launch point. Similarly, the origin humidity was defined as the humidity at the trajectory origin location. A Cartesian grid was defined, overlaying the polar stereographic projection of Antarctica. The mean origin and arrival humidity of every trajectory whose origin fell within each individual grid box was calculated. Grid boxes containing less than 10 trajectory endpoints were discarded. This allowed a plot of mean origin and arrival humidity as a function of origin location to be produced (Figure 6.4).

The origin humidities (Figures 6.4a-d) are largely zonally symmetric with the origin of highest moisture content occurring at the most northern regions. The driest trajectories depart from the centre of the Antarctic Continent as expected, given the direct relationship between saturation vapor pressure and temperature. The area covered increases with the period of the trajectory, which is consistent with the broadening of the distribution observed in figures 6.2a and 6.2c. However, co-located pixels contain similar origin humidities regardless of trajectory length. This suggests that origin humidity is a proxy for mean humidity at the origin location, and the synoptic flows that lead to air masses reaching the arrival location do not significantly effect humidity at each location.

The mean arrival humidity for trajectories of varying periods is shown in figures 6.4e-h. The patterns formed for trajectory length of 2.5-7.5 days show clear dipole patterns, with more humid trajectories departing from the Pacific sector of the Southern Ocean, and the drier trajectories departing from the Atlantic and Indian Sectors, as well as continental East Antarctica. This pattern is very strong for trajectories with periods between 2.5 and 5 days, but is somewhat weaker for trajectories of longer time periods.

For a 10 day trajectory length (Figure 6.4h), there is still evidence of trajectories departing from the Pacific Sector of the Southern Ocean being more humid than those from the Atlantic Sector. However, this signal is rather noisy and the humidity gradient across the continent is much weaker compared to that associated with shorter trajectories.

The mean arrival humidity displayed in figures 6.4e-h for most origin locations is an order of magnitude lower than the origin humidity (a-d), showing that moist air masses generally lose a significant amount of moisture as they travel to the HWD2 site. These factors suggest that the modification of the air parcel along its trajectory is important.

The sensitivity to the path taken is further highlighted in figure 6.1, which shows a sample of 5 day back trajectories. Each panel displays trajectories whose origin falls within the marked grey box. The colour of each individual back trajectory indicates the arrival humidity of that trajectory at the HWD2 site. Figures 6.1d and 6.1e show trajectories arriving from the Pacific sector of the Southern Ocean. The majority of these trajectories have a high humidity, indicating that moisture is often transported to HWD2 from the Pacific Sector. This is in agreement with figure 6.4f. Figures 6.1a and 6.1f show trajectories departing from the Atlantic Sector. These display a wider range of humidities, with the more western trajectories (Figure 6.1f) having higher humidity.

Figures 6.1b and 6.1c show trajectories arriving from the Western Pacific and Indian Sectors. These both show two distinct populations of trajectories. Trajectories that follow a clockwise (cyclonic) route passing over the ocean and RIS have high humidity, while those that follow an anti-clockwise (anti-cyclonic) path passing over East Antarctica and the Trans-Antarctic Mountains arrive with a much lower humidity. This illustrates air that passes over a high barrier, such as the TAM, will cool and cause water vapour in the air to condense and lose its moisture via precipitation before arriving at the HWD2 site. However, it also clearly demonstrates the sensitivity of the source of precipitation to the pathway taken. This has significant consequences as it means that changes in circulation will likely have a large impact in precipitation so accumulation rates can be strongly influenced by changes in circulation

6.4 Discussion

For a parcel of air to obtain significant quantities of moisture, a ready source of water is important. The Antarctic continent and the surrounding region of sea ice, which can reach as far north as 60° S (Kwok et al. 2016), reduces the probability of evaporation from occurring. Therefore only trajectories that originate at latitudes north of 60° S are likely to contain significant quantities of moisture at certain times of the year.

The majority of the 5 day trajectory origin points fall over the Antarctic continent (Figure 6.2a) and very few come in contact with regions of open water (Figure 6.2b). This suggests that trajectories of this length will be unsuitable for discerning the origins of moisture in air parcels. However, figure 6.3a indicates a strong relationship between the origin of 5 day trajectories and the occurrence of precipitation at HWD2. The reason for this is revealed in figure 6.4, which shows

that the mean humidity at arrival is very high for 5 day trajectories originating from the Pacific Sector of the Southern Ocean. This indicates that although 5 day trajectories often fail to extend far enough north to occur over regions of open water, and therefore sites of evaporation, they can identify pathways by which moisture is delivered to the site.

Figures 6.4a-d indicate that origin humidity is dependant on the local latitude. This is expected as the amount of moisture that can be held by a certain volume of air is dictated by temperature, a variable that is also strongly linked to latitude. The difference between origin and arrival humidities is large for the vast majority of trajectories. In particular, the humidity of most trajectories with origins north of 65° S drops by approximately an order of magnitude as they travel to HWD2. As trajectories travel south towards HWD2 they will cool and many will reach saturation, causing the formation of water and ice within the parcel, which will potentially be precipitated out before reaching HWD2. The magnitude of this effect will be amplified for trajectories that travel over high altitudes due to the effect of adiabatic cooling. This explains why the arrival humidity for trajectories is lower in the Pacific Sector of the Southern Ocean compared to those originating from the Atlantic Sector or over East Antarctica. The trajectories passing over the Atlantic Sector or East Antarctica must travel over the Antarctic continent. This presents a large topographic barrier, causing trajectories to move vertically and orographic precipitation to occur before arrival at HWD2.

While a strong gradient was present in the mean arrival humidities for 2.5-5 day trajectories, a similar gradient was not clear for 10 day trajectories. This represents a weaker relationship between the origin location and the precipitation at HWD2. However, figure 6.3c shows a clear relationship between the origin location for a trajectory and the precipitation at HWD2. This represents that the atmosphere over Southern Ocean becomes well mixed over timescales greater than 10 days and suggests that moisture was collected by the air parcels via evaporation within a 10 day time span.

The 10 day trajectories are also more diffuse than those of shorter trajectories, thus resulting in less trajectories originating from each pixel, and thus higher variance in arrival humidity. This can be observed in figure 6.4h, which is considerably nosier than panels (e-g) that represent shorter trajectory lengths. Another issue with 10 day trajectories is that longer trajectories are more susceptible to cumulative error. However, most of the features observed are large scale, so this is unlikely to fundamentally change our results.

The prevailing surface winds at HWD2 is a south-westerly katabatic drainage flow off the Trans-Antarctic Mountains. These winds will deliver cool, dry air from the inner continent and are generally associated with periods of decreased probability of precipitation occurring (Figure 6.3b). Occasionally, cyclonic low pressure systems reside in the Eastern Ross Sea; these may deliver moist air from the Ross Sea to HWD2 as air flows south in the eastern RIS before turning northwards, following the barrier presented by the Trans-Antarctic Mountains toward HWD2 (Nicolas and Bromwich 2011b). These synoptically driven flows over HWD2 will generally be associated with periods of increased probability of precipitation occurring.

Coggins and McDonald (2015) suggest that a deepening Amundsen Sea low will increase the rate that Ross air stream events will occur. This will increase the rate that dry continental air is driven over the ice shelf. Causing a negative effect the rate of snow accumulation on the Ross Ice Shelf. The reduced accumulation will also influence the sea ice cover in the Ross Sea. Snow cover acts as a insulating layer preventing sea ice from melting (Sturm and Massom 2009). In cases of large amounts of snow loading the increased weight can cause the ice to become submerged. Depending on the surrounding temperatures this can either enhance the break-up of sea ice or the snow-water mixture can freeze adding to sea ice production (Maksym and Markus 2008).

Our analysis has shown that 5 day trajectories are most suitable for this type of analysis, however this value may differ at other locations, and will be the subject of future work. Furthermore, HWD2 is relatively near the coast. For other sites closer to the interior of the continent, longer trajectory periods may be necessary as an air parcel will often take longer to travel the increased distance towards the ocean.

6.5 Conclusions

From our analysis based on trajectory origin locations, we hypothesise that the 5 day trajectory lengths are most suitable for surface mass balance analysis at HWD2. Trajectories longer than 5 days show a reduced relationship between the origin and the arrival humidity, and also the rate of precipitation. Although this trend continues to improve at even shorter trajectory lengths. We present two possible explanations for this: Trajectories of this length are longer than the residence time of moisture in the atmosphere, and therefore show little relationship between the moisture delivered and origin location. Alternatively, errors in the

trajectory pathway prevent any link between origin and arrival humidity to be observed.

Air originating from the Pacific Sector of the Southern Ocean was found to carry more moisture to the HWD2 site than air originating from the Atlantic Sector of the Southern Ocean. These regions coincide with the areas where origin frequency increases during periods of higher and lower probability of precipitation respectively.

Parcels arriving from the same point of origin are shown to have vastly different arrival humidities based on the pathway of the trajectory. This indicates that simply looking at origin locations does not always reveal how much moisture arrives from a particular site. To fully understand how moisture is delivered from the origin to the arrival point synoptic patterns, and how they influence the potential pathways, must be considered. Moreover, this suggests that changes to the frequency of occurrence of circulation patterns would also have a significant impact on the amount of accumulation, and potentially the isotopic record, collected at the HWD2 site. This is likely similar for other records collected on the Ross Ice Shelf (RIS).

Chapter 7

Discussion and Conclusions

The primary goal of this thesis was to identify how the changing climate over the Ross Sea affects the interactions between the atmosphere and the cryosphere in this region. To achieve this goal three studies were conducted, each represented by an individual chapter of this thesis:

- The relationship between wind speeds observed at the northern edge of the RIS and SIC within the RSP was investigated, with particular focus on the persistence of the open polynya following severe weather events (Chapter 4).
- CMET balloon observations were made over the Ross Sea. These were compared to predictions made by the AMPS model, providing some validation of the AMPS model. The heat and moisture fluxes from the RSP were also studied using Lagrangian and Eulerian derivatives calculated from AMPS fields (Chapter 5).
- Precipitation over the RIS was investigated. A large ensemble of Lagrangian back trajectories was used to identify key sources of moisture for a specific site over the RIS (Chapter 6).

Each of these has either been submitted, or is to be submitted, as a journal article. Chapter 4 (published as a paper in *The Cryosphere* (Dale et al. 2017)) investigated the influence of strong wind events during the austral winter on the Ross Sea Polynya (RSP). Cross Correlation Functions (CCFs) were calculated between observations made at the Laurie II Automatic Weather Station (AWS) and sea ice concentration (SIC) observed within the RSP. Strong, negative correlations were found between the wind speed over the Ross Ice Shelf (RIS) and the SIC within the polynya, with the strongest correlation occurring at 12 h lag. This indicates that the polynya is often opened during strong wind events, and reaches minimum SIC after a strong wind event has persisted for 12 h. The CCF was found

to have strong asymmetry, with a rapid decrease at the onset of a strong wind event (48 h *e*-folding time), and a more gradual increase (100 h *e*-folding time). This highlights that the polynya opens rapidly as strong winds cause northward advection of sea ice. Following a strong wind event, the polynya closes at a more gradual rate though thermodynamic freezing of seawater.

Each day was categorised into low ($< 3.5\,\mathrm{ms}^{-1}$), medium, and high ($> 7.5\,\mathrm{ms}^{-1}$) wind states based on speeds observed at the Laurie II AWS. When CCFs were made using only days within each of these categories, stronger correlations were found within the high wind speed state. This indicates that strong wind events have the largest influence on SIC within the RSP. Composites were made using SIC fields from days of each specific wind speed state. Positive SIC anomalies were observed during periods of low wind speed, and negative anomalies were observed during periods of high wind speed. These anomalies persisted for up to five days, which is much longer than the average wind event.

Composites were also made for sea ice motion vectors based on the low, medium, and high wind states. Cyclonic drift anomalies were found throughout the entire Ross Sea during periods where strong winds were observed at the Laurie II AWS. These drift anomalies were found to persist for 48 hours following a strong wind event. This is less than the persistence of the SIC anomalies for the same conditions, indicating that the sea ice recovery within the RSP likely occurs through thermodynamic rather than advective processes, thus demonstrating the link between the strong wind events and sea ice production within the RSP.

Wind speeds observed at several AWS on the RIS were compared to co-located ERA-Interim model winds. While the two data sets were found to correlate strongly, ERA-Interim was found to underestimate the wind speed. This underestimation was found to be stronger near topography, as the Laurie II AWS wind speeds were 1.7 times faster than that of ERA-Interim. This highlights that the relatively low resolution of ERA-Interim limits the model's ability to accurately model wind speed in areas of complex topography.

Chapter 5 (in review for publication in *Journal of Geophysical Review - Atmospheres* at the time of writing) presents observations from the first long-duration Controlled Meteorological (CMET) balloon flights within the atmospheric boundary layer over the Ross Sea performed in November 2017. A single flight was analysed. This balloon flew for 70 hours and performed 31 vertical soundings of the atmospheric boundary layer in the vicinity of the RSP.

Balloon observations of temperature, specific humidity, and wind velocity were

compared to predictions made by the Antarctic Mesoscale Prediction System (AMPS) forecast model. AMPS forecasts generally agreed with the co-located observations made by the CMET balloon. Wind direction was found to be more accurately predicted by AMPS during periods of strong wind speed, and larger errors in the wind direction were found when wind speeds were low. A large amount of variability was found between co-located AMPS predictions from consecutive forecast initialisations. This variability was found to bound the CMET balloon observations.

The upward heat and moisture fluxes from the RSP during the flight period of the CMET balloon were investigated. Using AMPS model output, SIC and surface heat flux fields indicated that the polynya was open, and providing a source of heat and moisture to the atmosphere during the study period. Lagrangian and Eulerian derivatives of both potential temperature and total water mixing ratio were calculated over a surface covering the southwestern Ross Sea. From these, an advection term for both heat and moisture could be calculated. A large source of heat covering a 100 km by 200 km area was observable in this advection term at 500m above the surface in the vicinity of the RSP. Similar diabatic heating was also observed at 250 m and 1000 m above the surface during this period in potential temperature fields. Puzzlingly, the calculated total water mixing ratio field did not show any evidence of a moisture source existing over the RSP. This indicates that AMPS did not predict upward moisture flux from the polynya despite latent heat fluxes being observed within the polynya. The relatively good agreement between the AMPS predictions and the CMET balloon observations suggest that the derivative methodology used here might be more widely useful in understanding the influence of polynya on the local atmospheric environment, and as a way to quantify the scale of this influence.

Chapter 6 presents an analysis of moisture origins for precipitation events over the RIS. 50 000 Lagrangian back trajectories were propagated backwards from the HWD2 field site, these were calculated using ERA-Interim reanalysis wind fields. During periods of precipitation over HWD2, trajectories originated more frequently from the Pacific sector of the Southern Ocean, and less frequently from the Atlantic Sector of the Southern Ocean.

The relationship between humidity at origin and humidity at arrival was found to weaken for trajectories with temporal lengths greater than 5 days. This suggests that the mean residence time for moisture within the air parcel represented by these trajectories is approximately 5 days. This diminishing relationship may

also be a result of errors in the trajectory pathway preventing any link between origin and arrival humidity to be observed.

Air parcels with similar origin locations and humidities were often found to arrive at HWD2 with vastly different arrival humidities. This difference was shown to be strongly dependant on the trajectory pathway. Air parcels that passed over large topographical barriers often lost their moisture through precipitation as they cooled adiabatically. This indicates that both the origin location and trajectory pathway are important to moisture transport. This also highlights the potential influence changes in the frequency of various atmospheric circulation patterns would have on accumulation rates, and potentially isotopic records over Antarctica.

Chapters 4 and 5 investigated interactions between the atmosphere and sea ice within the RSP. The SIC within the polynya was found to be strongly correlated to surface wind speed, mirroring results by Holland and Kwok (2012). A source of heat was observed over the RSP during the period of observation, indicating the influence of warm, open water on the atmosphere above. During this period the open polynya was not identified as a source of moisture within the AMPS model. During winter, moisture flux within coastal polynyas has a large effect on local climate as the increased winter sea ice cover otherwise isolates coastal regions from an oceanic moisture source (Bracegirdle et al. 2015). Chapter 6 identified that air parcels with high arrival humidities most frequently originated north of the marginal ice zone. Unfortunately the analysis of chapter 6 was at too low a resolution to identify if moisture from polynyas had any impact on precipitation over the RIS.

Over recent decades, the central pressure of the Amundsen Sea Low (ASL) has deepened (Hosking et al. 2013). This has been driven, in part, by the strengthening of the Southern Annular Mode (SAM) (Clem and Fogt 2013), which is in turn driven by increased meridional transport of heat in a warming climate. The increased onshore flow over the Bellingshausen sea provides conditions that increase the rate of formation of Ross Air Stream (RAS) events over the Ross Sea (Coggins and McDonald 2015). Chapter 4 highlighted the influence of strong winds over the RSP, such as those that occur during RAS events, on sea ice production within the RSP. This suggests that if strong RAS events are to occur more frequently in the future, the RSP will be driven open by the strong winds that occur during these events (Coggins and McDonald 2015). In addition to the increased rate of sea ice production this will cause, the polynya will also be open

more frequently. This will allow for increased thermal and moisture transport upwards into the atmosphere.

The influence that increases the frequency of RAS events will have on the snow accumulation rates on the Ross Ice Shelf is uncertain. The largest precipitation events occurred during periods of northerly flow over the Ross Ice Shelf. The deepening ASL is likely to reduce the rate of occurrence of these events, reducing the average accumulation rate. However, the increased rate of onshore flow from the Amundsen and Bellingshausen seas may provide an increased source of moisture to the Ross Ice Shelf. As figure 6.1e shows air parcels are able to pass over Western Antarctica without losing too much moisture. Increasing global temperatures will also positively influence the rate of snow accumulation on the RIS, as warmer air is able to transport larger quantities of moisture.

Throughout this thesis, the accuracy of numerical weather models in the vicinity of complex topography is a key issue. Chapter 4 identified that ERA-Interim wind speeds were significantly underestimated in the vicinity of Ross Island, this effect was not as large at a site further from Ross Island. Chapter 5 identified that the largest errors in AMPS wind direction occurred in the vicinity of the Trans-Antarctic Mountains. In Chapter 6 ERA-Interim was used for trajectory calculations. The accuracy of this model in the vicinity of complex topography was, therefore, a large source of error in the calculated trajectories. Although increasing model resolution has been shown to reduce these errors (Bromwich et al. 2005), the resolution required within current models to completely eliminate these errors is unfeasible for models of global and decadal scales. This suggests that dramatic improvements in the accuracy of numerical weather models will likely come in the form of improved parameterisation of sub-grid-scale processes. These potential improvements will likely require the guidance of high-density observations, thus highlighting the importance of observational platforms such as CMET balloons and ground-based AWSs that were used in this thesis.

Lagrangian trajectories were used in both chapters 5 and 6. This proved to be a valuable technique for analysing atmospheric circulation patterns. The methodology used in chapter 5 used Lagrangian trajectories to calculate Lagrangian derivatives of various AMPS fields. This allowed the identification of sources and sinks of both heat and moisture. This proved widely useful in understanding the influence of polynya on the local atmospheric environment.

7.1 Future Work

The geographical footprint of the RSP is controlled by complex surface wind flows and ocean currents. The analysis in Chapter 4 only compared wind speed at a single point and sea ice area (SIA) in a sub-region of the Polynya. This reduced the dimensionality of the data dramatically simplifying analysis. Another potential method of reducing the dimensionality of the SIC data is to apply a clustering method such as self organising maps. This would produce a small number of characteristic polynya configurations, providing a polynya climatology. This climatology would reflect polynya variability dependant on both atmospheric and oceanic forcing. Comparison of the polynya configurations with overlying wind and temperature patterns, such as those produced by Coggins et al. (2014), would allow insight into how winds driven by varying synoptic and mesoscale forcings affect the SIC and rate of sea ice production within the polynya.

The Lagrangian derivative methodology used in chapter 5 proved useful for understanding how the AMPS model represented the influence of the RSP on the atmosphere. However, derivatives were only calculated for a single 24 hour period. If this was instead calculated for a large number of 24 hour periods, a climatological mean of these derivatives could be found. This could be used to quantify the heat and moisture fluxes for a given polynya. The seasonality of these fluxes would also be of interest as the heat source provided during the winter would be much more significant in the absence of insolation. Comparing these derivatives to the polynya climatology described above would also be of interest.

In Chapter 5, CMET balloons were deployed over the Ross Sea for the first time. CMET balloons were found to be able to withstand the harsh Antarctic environment, the dry air, and constant sunlight during summer months, which was found to be desirable for balloon flights. The success of this campaign has raised interest in a second CMET deployment in the Ross Sea region, with focus of probing the influence of RAS events on the RSP. This would likely see balloons launched from a location on the Ross Ice Shelf, directly upstream of the RSP during the prominent RAS events. During the 2017 deployment, the radiosonde balloons launched from Mario Zucchelli station proved useful for identifying suitable launch windows as well as calibration and validation of the CMET observation. In a future campaign, radiosonde balloons would likely be used extensively as they are inexpensive relative to CMET balloons, and greatly improves the probability of a successful CMET balloon flight. RAS events occur more frequently, and with greater intensity, during the austral winter. The polynya is also

of greater interest during this period. The increased temperature differential between the ocean and the atmosphere leads to greater upward heat flux from the polynya. The cooler, drier air, as well as larger sea ice extent causing greater isolation from open water, make the polynya a more important moisture and heat source during winter months. Unfortunately CMET balloons, which rely on solar power, are incapable of operating during winter. Field access is also incredibly difficult during winter. A potential second CMET campaign would most likely be constrained to occurring during the summer season.

The Lagrangian back trajectory analysis presented in chapter 6 used a fixed trajectory length. An event-based trajectory length method such as that used by Sodemann and Stohl (2009), would allow identification of evaporation events, and therefore more accurately identify the source of moisture. This methodology identified evaporation events based on the temporal derivative of specific humidity and proximity to open water.

The trajectory analysis in chapter 6 was unable to identify if Antarctic polynyas had any influence on precipitation over the RIS. This was due to the relatively small footprint of polynyas, resulting in a small number of trajectories originating from over polynyas. The impact of a polynya on precipitation could instead be investigated using forward trajectories propagated from over the polynya. This would allow regions that often receive air parcels that have interacted with the polynya to be identified. The influence of the polynya on precipitation within these regions could then be quantified by comparing periods when air parcels arrived from the polynya to the overall mean precipitation.

Bibliography

Agosta, C., X. Fettweis, and R. Datta (Dec. 2015). "Evaluation of the CMIP5 models in the aim of regional modelling of the Antarctic surface mass balance". In: *Cryosphere* 9.6, pp. 2311–2321. DOI: 10.5194/tc-9-2311-2015.

Alexander, S. P., A. R. Klekociuk, A. J. McDonald, and M. C. Pitts (Oct. 2013). "Quantifying the role of orographic gravity waves on polar stratospheric cloud occurrence in the Antarctic and the Arctic". In: *J. Geophys. Res. Atmos.* 118.20, pp. 11, 493–11, 507. DOI: 10.1002/2013JD020122.

Armour, Kyle C. and C. M. Bitz (2015). "Observed and projected trends in Antarctic sea ice." In: *US CLIVAR Var.* 13.4, pp. 12–19.

Armstrong, R., K. Knowles, M. J. Brodzik, and M. A. Hardman. (1994). *DMSP SSM/I-SSMIS Pathfinder Daily EASE-Grid Brightness Temperatures, Version 2.* DOI: doi:https://doi.org/10.5067/3EX2U1DV3434..

Arnold, Marcus (2016). "Surface mass balance of the Ross Ice Shelf from stable water isotopes, ground penetrating radar, and back trajectory analyses". Masters Thesis. University of Canterbury.

Arrhenius, Svante (Apr. 1896). "XXXI. On the influence of carbonic acid in the air upon the temperature of the ground". In: *London, Edinburgh, Dublin Philos. Mag. J. Sci.* 41.251, pp. 237–276. DOI: 10.1080/14786449608620846.

Baines, Peter G. and Klaus Fraedrich (Nov. 1989). "Topographic Effects on the Mean Tropospheric Flow Patterns around Antarctica". In: *J. Atmos. Sci.* 46.22, pp. 3401–3415. DOI: 10.1175/1520-0469(1989)046<3401:TEOTMT>2.0.CO;2.

Ball, FK (1956). "The Theory of Strong Katabatic Winds". In: *Aust. J. Phys.* 9.3, p. 373. DOI: 10.1071/PH560373.

Batrak, Yurii and Malte Müller (July 2018). "Atmospheric Response to Kilometer-Scale Changes in Sea Ice Concentration Within the Marginal Ice Zone". In: *Geophys. Res. Lett.* 45.13, pp. 6702–6709. DOI: 10.1029/2018GL078295.

Bentley, Charles R. (Mar. 1990). "The Ross Ice Shelf Geophysical and Glaciological Survey (RIGGS): Introduction and summary of measurements performed". In: ed. by Charles R. Bentley and Dennis E. Hayes, pp. 1–20. DOI: 10.1029/AR042p0001.

Bintanja, R., G.J. van Oldenborgh, and C.A. Katsman (July 2015). "The effect of increased fresh water from Antarctic ice shelves on future trends in Antarctic sea ice". In: *Ann. Glaciol.* 56.69, pp. 120–126. DOI: 10.3189/2015AoG69A001.

Bintanja, R., G. J. Van Oldenborgh, S. S. Drijfhout, B. Wouters, and C. A. Katsman (2013). "Important role for ocean warming and increased ice-shelf melt in Antarctic sea-ice expansion". In: *Nat. Geosci.* 6.5, pp. 376–379. DOI: 10.1038/ngeo1767.

Bourassa, Mark A., Sarah T. Gille, Cecilia Bitz, David Carlson, Ivana Cerovecki, Carol Anne Clayson, Meghan F. Cronin, Will M. Drennan, Chris W. Fairall, Ross N. Hoffman, Gudrun Magnusdottir, Rachel T. Pinker, Ian A. Renfrew, Mark Serreze, Kevin Speer, Lynne D. Talley, and Gary A. Wick (Mar. 2013). "High-Latitude Ocean and Sea Ice Surface Fluxes: Challenges for Climate Research". In: *Bull. Am. Meteorol. Soc.* 94.3, pp. 403–423. DOI: 10.1175/BAMS-D-11-00244.1.

Bracegirdle, Thomas J. (Mar. 2013). "Climatology and recent increase of westerly winds over the Amundsen Sea derived from six reanalyses". In: *Int. J. Climatol.* 33.4, pp. 843–851. DOI: 10.1002/joc.3473.

Bracegirdle, Thomas J. and Erik W. Kolstad (Jan. 2010). "Climatology and variability of Southern Hemisphere marine cold-air outbreaks". In: *Tellus A Dyn. Meteorol. Oceanogr.* 62.2, pp. 202–208. DOI: 10.1111/j.1600-0870.2009.00431.x.

Bracegirdle, Thomas J. and Gareth J. Marshall (Oct. 2012). "The Reliability of Antarctic Tropospheric Pressure and Temperature in the Latest Global Reanalyses". In: *J. Clim.* 25.20, pp. 7138–7146. DOI: 10.1175/JCLI-D-11-00685.1.

Bracegirdle, Thomas J., David B. Stephenson, John Turner, and Tony Phillips (Dec. 2015). "The importance of sea ice area biases in 21st century multimodel projections of Antarctic temperature and precipitation". In: *Geophys. Res. Lett.* 42.24, pp. 10, 832–10, 839. DOI: 10.1002/2015GL067055.

Brodzik, M. J. and J. S. Stewart (2016). *Near-Real-Time SSM/I-SSMIS EASE-Grid Daily Global Ice Concentration and Snow Extent, Version 5.* DOI: 10.5067/3KB2JPLFPK3R.

Bromwich, David H. (July 1989). "Satellite Analyses of Antarctic Katabatic Wind Behavior". In: *Bull. Am. Meteorol. Soc.* 70.7, pp. 738–749. DOI: 10.1175/1520-0477(1989)070<0738:SAOAKW>2.0.CO;2.

– (July 1991). "Mesoscale Cyclogenesis over the Southwestern Ross Sea Linked to Strong Katabatic Winds". In: *Mon. Weather Rev.* 119.7, pp. 1736–1753. DOI: 10.1175/1520-0493(1991)119<1736:MCOTSR>2.0.CO;2.

Bromwich, David H., Jorge F. Carrasco, Zhong Liu, and Ren-Yow Tzeng (1993). "Hemispheric atmospheric variations and oceanographic impacts associated

with katabatic surges across the Ross ice shelf, Antarctica". In: *J. Geophys. Res.* 98.D7, p. 13045. DOI: 10.1029/93JD00562.

Bromwich, David H., Jorge F. Carrasco, and Charles R. Stearns (Sept. 1992). "Satellite Observations of Katabatic-Wind Propagation for Great Distances across the Ross Ice Shelf". In: *Mon. Weather Rev.* 120.9, pp. 1940–1949. DOI: 10.1175/1520-0493(1992)120<1940:SOOKWP>2.0.CO;2.

Bromwich, David H., Yang Du, and Thomas R. Parish (July 1994). "Numerical Simulation of Winter Katabatic Winds from West Antarctica Crossing Siple Coast and the Ross Ice Shelf". In: *Mon. Weather Rev.* 122.7, pp. 1417–1435. DOI: 10.1175/1520-0493(1994)122<1417:NSOWKW>2.0.CO;2.

Bromwich, David H., Zhong Liu, Aric N Rogers, and Michael L Van Woert (1998). "Winter atmospheric forcing of the Ross Sea Polynya". In: *Ocean. ICE, Atmos. Interact. Antarct. Cont. MARGIN*. Vol. 75. American Geophysical Union, pp. 101–133. DOI: 10.1029/AR075p0101.

Bromwich, David H., Andrew J. Monaghan, Kevin W. Manning, and Jordan G. Powers (Mar. 2005). "Real-Time Forecasting for the Antarctic: An Evaluation of the Antarctic Mesoscale Prediction System (AMPS)*". In: *Mon. Weather Rev.* 133.3, pp. 579–603. DOI: 10.1175/MWR-2881.1.

Bromwich, David H., Andrew J. Monaghan, Jordan G. Powers, John J. Cassano, He-Lin Wei, Ying-Hwa Kuo, and Andrea Pellegrini (Feb. 2003). "Antarctic Mesoscale Prediction System (AMPS): A Case Study from the 2000–01 Field Season*". In: *Mon. Weather Rev.* 131.2, pp. 412–434. DOI: 10.1175/1520-0493(2003)131<0412:AMPSAA>2.0.CO;2.

Bromwich, David H., Julien P. Nicolas, and Andrew J. Monaghan (Aug. 2011). "An Assessment of Precipitation Changes over Antarctica and the Southern Ocean since 1989 in Contemporary Global Reanalyses *". In: *J. Clim.* 24.16, pp. 4189–4209. DOI: 10.1175/2011JCLI4074.1.

Bromwich, David H., Francis O. Otieno, Keith M. Hines, Kevin W. Manning, and Elad Shilo (Jan. 2013). "Comprehensive evaluation of polar weather research and forecasting model performance in the Antarctic". In: *J. Geophys. Res. Atmos.* 118.2, pp. 274–292. DOI: 10.1029/2012JD018139.

Brümmer, Burghard and Heinrich Hoeber (1999). "A mesoscale cyclone over the Fram Strait and its effects on sea ice". In: *J. Geophys. Res. Atmos.* 104.D16, pp. 19085–19098. DOI: 10.1029/1999JD900259.

Brümmer, Burghard, David Schröder, Gerd Müller, Gunnar Spreen, Annika Jahnke-Bornemann, and Jouko Launiainen (2008). "Impact of a Fram Strait cyclone on ice edge, drift, divergence, and concentration: Possibilities and limits

of an observational analysis". In: *J. Geophys. Res. Ocean.* 113.12, pp. 1–15. DOI: 10.1029/2007JC004149.

Budillon, Giorgio, Pasquale Castagno, Stefano Aliani, Giancarlo Spezie, and Laurie Padman (Oct. 2011). "Thermohaline variability and Antarctic bottom water formation at the Ross Sea shelf break". In: *Deep Sea Res. Part I Oceanogr. Res. Pap.* 58.10, pp. 1002–1018. DOI: 10.1016/j.dsr.2011.07.002.

Buzzi, A., R. Cadelli, and P. Malguzzi (Mar. 1997). "Low-level jet simulation over the Southern Ocean in Antarctica". In: *Tellus A* 49.2, pp. 263–276. DOI: 10.1034/j.1600-0870.1997.t01-1-00007.x.

Carrasco, Jorge F. and David H. Bromwich (1993). "Mesoscale cyclogenesis dynamics over the southwestern Ross Sea, Antarctica". In: *J. Geophys. Res.* 98.D7, p. 12973. DOI: 10.1029/92JD02821.

Cassano, John J., Melissa A. Nigro, and Matthew A. Lazzara (Apr. 2016). "Characteristics of the near-surface atmosphere over the Ross Ice Shelf, Antarctica". In: *J. Geophys. Res. Atmos.* 121.7, pp. 3339–3362. DOI: 10.1002/2015JD024383.

Cavalieri, Donald J. (1994). "A microwave technique for mapping thin sea ice". In: *J. Geophys. Res.* 99.C6, p. 12561. DOI: 10.1029/94JC00707.

Cavalieri, Donald J., P. Gloersen, and W. J. Campbell (1984). "Determination of sea ice parameters with the NIMBUS 7 SMMR". In: *J. Geophys. Res. Atmos.* 89.D4, pp. 5355–5369. DOI: 10.1029/JD089iD04p05355.

Cavalieri, Donald J., C. L. Parkinson, P. Gloersen, and H. J. Zwally (1996). *Sea Ice Concentrations from Nimbus-7 SMMR and DMSP SSM/I-SSMIS Passive Microwave Data, Version 1*. DOI: doi.org/10.5067/8GQ8LZQVL0VL.

Cavalieri, Donald J. and Claire L. Parkinson (2012). "Arctic sea ice variability and trends, 1979-2010". In: *Cryosphere* 6.4, pp. 881–889. DOI: 10.5194/tc-6-881-2012.

Cavalieri, Donald J., Claire L. Parkinson, P. Gloersen, Josefino C. Comiso, and H. J. Zwally (1999). "Deriving long-term time series of sea ice cover from satellite passive-microwave multisensor data sets". In: *J. Geophys. Res.* 104.C7, PP.–15, 803–15, 814. DOI: 199910.1029/1999JC900081.

Chenoli, Sheeba Nettukandy, John Turner, and Azizan Abu Samah (2015). "A Strong Wind Event on the Ross Ice Shelf, Antarctica: A Case Study of Scale Interactions". In: *Mon. Weather Rev.* 143.10, pp. 4163–4180. DOI: 10.1175/mwr-d-15-0002.1.

Church, JA, PU Clark, A Cazenave, JM Gregory, S Jevrejeva, A Levermann, MA Merrifield, GA Milne, RS Nerem, PD Nunn, et al. (2013). "Climate change 2013:

the physical science basis. Contribution of Working Group I to the Fifth Assessment Report of the Intergovernmental Panel on Climate Change". In: *Sea level change*, pp. 1137–1216.

Clausen, H B and W Dansgaard (1977). "Less surface accumulation on the Ross Ice Shelf than hitherto assumed". In: *Iash* 118, pp. 172–176.

Clem, Kyle R. and Ryan L. Fogt (Oct. 2013). "Varying roles of ENSO and SAM on the Antarctic Peninsula climate in austral spring". In: *J. Geophys. Res. Atmos.* 118.20, pp. 11, 481–11, 492. DOI: 10.1002/jgrd.50860.

Coggins, Jack H. J. and Adrian J. McDonald (Mar. 2015). "The influence of the Amundsen Sea Low on the winds in the Ross Sea and surroundings: Insights from a synoptic climatology". In: *J. Geophys. Res. Atmos.* 120.6, pp. 2167–2189. DOI: 10.1002/2014JD022830.

Coggins, Jack H. J., Adrian J. McDonald, and Ben Jolly (June 2014). "Synoptic climatology of the Ross Ice Shelf and Ross Sea region of Antarctica: k -means clustering and validation". In: *Int. J. Climatol.* 34.7, pp. 2330–2348. DOI: 10.1002/joc.3842.

Coggins, Jack H. J., Adrian J. McDonald, G Plank, M Pannell, B Jolly, S Parsons, and T Delany (Aug. 2013). "SNOW-WEB: a new technology for Antarctic meteorological monitoring". In: *Antarct. Sci.* 25.04, pp. 583–599. DOI: 10.1017/S0954102013000011.

Cohen, L. and S. Dean (Sept. 2013). "Snow on the Ross Ice Shelf: comparison of reanalyses and observations from automatic weather stations". In: *Cryosphere* 7.5, pp. 1399–1410. DOI: 10.5194/tc-7-1399-2013.

Cohen, Lana, Sam Dean, and James Renwick (2013). "Synoptic weather types for the ross sea region, Antarctica". In: *J. Clim.* 26.2, pp. 636–649. DOI: 10.1175/JCLI-D-11-00690.1.

Comiso, Josefino C. (1986). "Characteristics of Arctic winter sea ice from satellite multispectral microwave observations". In: *J. Geophys. Res.* 91.C1, p. 975. DOI: 10.1029/JC091iC01p00975.

– (2000). "Bootstrap Sea Ice Concentrations from Nimbus-7 SMMR and DMSP SSM/I-SSMIS, Version 2." In: *Boulder, Color. USA. NASA Natl. Snow Ice Data Cent. Distrib. Act. Arch. Center.* DOI: http://dx.doi.org/10.5067/J6JQLS9EJ5HU.

– (2017). *Bootstrap Sea Ice Concentrations from Nimbus-7 SMMR and DMSP SSM/I-SSMIS, Version 3*. DOI: 10.5067/7Q8HCCWS4I0R.

Comiso, Josefino C., Robert A. Gersten, Larry V. Stock, John Turner, Gay J. Perez, and Kohei Cho (2017). "Positive Trend in the Antarctic Sea Ice Cover and Associated Changes in Surface Temperature". In: *J. Clim.* 30.6, pp. 2251–2267. DOI: 10.1175/JCLI-D-16-0408.1.

Comiso, Josefino C., Ronald Kwok, Seelye Martin, and Arnold L. Gordon (Apr. 2011). "Variability and trends in sea ice extent and ice production in the Ross Sea". In: *J. Geophys. Res.* 116.C4, p. C04021. DOI: 10.1029/2010JC006391.

Comiso, Josefino C. and Fumihiko Nishio (2008). "Trends in the sea ice cover using enhanced and compatible AMSR-E, SSM/I, and SMMR data". In: *J. Geophys. Res. Ocean.* 113.2, pp. 1–22. DOI: 10.1029/2007JC004257.

Costanza, Carol A., Matthew A. Lazzara, Linda M. Keller, and John J. Cassano (Dec. 2016). "The surface climatology of the Ross Ice Shelf Antarctica". In: *Int. J. Climatol.* 36.15, pp. 4929–4941. DOI: 10.1002/joc.4681.

Cotté, Cédric and Christophe Guinet (2007). "Historical whaling records reveal major regional retreat of Antarctic sea ice". In: *Deep. Res. Part I Oceanogr. Res. Pap.* 54.2, pp. 243–252. DOI: 10.1016/j.dsr.2006.11.001.

Crary, A. P., Edwin S. Robinson, Hugh F. Bennett, and Walter W. Boyd (July 1962). "Glaciological regime of the Ross Ice Shelf". In: *J. Geophys. Res.* 67.7, pp. 2791–2807. DOI: 10.1029/JZ067i007p02791.

Curry, Judith a., J L Schramm, and E E Ebert (1995). *Sea-Ice Albedo Climate Feedback Mechanism*. DOI: Doi10.1175/1520-0442(1995)008<0240:Siacfm>2.0.Co;2.

Dale, Ethan R., Adrian J. McDonald, Jack H. J. Coggins, and Wolfgang Rack (Jan. 2017). "Atmospheric forcing of sea ice anomalies in the Ross Sea polynya region". In: *Cryosphere* 11.1, pp. 267–280. DOI: 10.5194/tc-11-267-2017.

De La Mare, William K. (2009). *Changes in Antarctic sea-ice extent from direct historical observations and whaling records*. Vol. 92. 3-4, pp. 461–493. DOI: 10.1007/s10584-008-9473-2.

Dee, D. P., S. M. Uppala, A. J. Simmons, P. Berrisford, P. Poli, S. Kobayashi, U. Andrae, M. A. Balmaseda, G. Balsamo, P. Bauer, P. Bechtold, A. C M Beljaars, L. van de Berg, J. Bidlot, N. Bormann, C. Delsol, R. Dragani, M. Fuentes, A. J. Geer, L. Haimberger, S. B. Healy, H. Hersbach, E. V. Hólm, L. Isaksen, P. Kållberg, M. Köhler, M. Matricardi, A. P. McNally, B. M. Monge-Sanz, J.-J. Morcrette, B.-K. Park, C. Peubey, P. de Rosnay, C. Tavolato, J.-N. Thépaut, and F. Vitart (Apr. 2011). "The ERA-Interim reanalysis: configuration and performance of the data assimilation system". In: *Q. J. R. Meteorol. Soc.* 137.656, pp. 553–597. DOI: 10.1002/qj.828.

Dinniman, Michael S., John M. Klinck, Eileen E. Hofmann, and Walker O. Smith (2018). "Effects of projected changes in wind, atmospheric temperature, and

freshwater inflow on the Ross Sea". In: *J. Clim.* 31.4, pp. 1619–1635. DOI: 10.1175/JCLI-D-17-0351.1.

Dittmann, Anna, Elisabeth Schlosser, Valérie Masson-Delmotte, Jordan G. Powers, Kevin W. Manning, Martin Werner, and Koji Fujita (June 2016). "Precipitation regime and stable isotopes at Dome Fuji, East Antarctica". In: *Atmos. Chem. Phys.* 16.11, pp. 6883–6900. DOI: 10.5194/acp-16-6883-2016.

Doddridge, Edward W. and John Marshall (2017). "Modulation of the Seasonal Cycle of Antarctic Sea Ice Extent Related to the Southern Annular Mode". In: *Geophys. Res. Lett.* 44.19, pp. 9761–9768. DOI: 10.1002/2017GL074319.

Drucker, Robert, Seelye Martin, and Ronald Kwok (2011). "Sea ice production and export from coastal polynyas in the Weddell and Ross Seas". In: *Geophys. Res. Lett.* 38.17, pp. 4–7. DOI: 10.1029/2011GL048668.

Eicken, Hajo, Holger Fischer, and Peter Lemke (Jan. 1995). "Effects of the snow cover on Antarctic sea ice and potential modulation of its response to climate change". In: *Annals of Glaciology* 21, pp. 369–376. DOI: 10.3189/S0260305500016086.

Eisenman, I., Walter N. Meier, and J. R. Norris (July 2014). "A spurious jump in the satellite record: has Antarctic sea ice expansion been overestimated?" In: *Cryosphere* 8.4, pp. 1289–1296. DOI: 10.5194/tc-8-1289-2014.

Elvidge, Andrew D, Ian A Renfrew, John C King, Andrew Orr, Tom A. Lachlan-Cope, Mark Weeks, and Sue L Gray (Apr. 2015). "Foehn jets over the Larsen C Ice Shelf, Antarctica". In: *Q. J. R. Meteorol. Soc.* 141.688, pp. 698–713. DOI: 10.1002/qj.2382.

Emery, W J, C W Fowler, and J A Maslanik (1997). "Satellite-derived maps of Arctic and Antarctic sea ice motion: 1988 to 1994". In: *Geophys. Res. Lett.* 24.8, pp. 897–900.

Favier, V., C. Agosta, S. Parouty, G. Durand, G. Delaygue, H. Gallée, A.-S. Drouet, A. Trouvilliez, and G. Krinner (Apr. 2013). "An updated and quality controlled surface mass balance dataset for Antarctica". In: *Cryosphere* 7.2, pp. 583–597. DOI: 10.5194/tc-7-583-2013.

Ferreira, David, John Marshall, Cecilia M. Bitz, Susan Solomon, and Alan Plumb (2015). "Antarctic ocean and sea ice response to ozone depletion: A two-time-scale problem". In: *J. Clim.* 28.3, pp. 1206–1226. DOI: 10.1175/JCLI-D-14-00313.1.

Fetterer, F., K. Knowles, Walter N. Meier, and M. Savoie (2002). "Sea ice index". In: *National Snow and Ice Data Center, Boulder, CO, digital media.[Available online at http://nsidc. org/data/g02135. html.]*

Fogt, Ryan L., Alex J. Wovrosh, Ryan A. Langen, and Ian Simmonds (Apr. 2012). "The characteristic variability and connection to the underlying synoptic activity of the Amundsen-Bellingshausen Seas Low". In: *J. Geophys. Res. Atmos.* 117.D7, n/a–n/a. DOI: 10.1029/2011JD017337.

Fons, Steven W. and Nathan T. Kurtz (Sept. 2018). "Retrieval of snow freeboard of Antarctic sea ice using waveform fitting of CryoSat-2 returns". In: *Cryosph. Discuss.* Pp. 1–21. DOI: 10.5194/tc-2018-164.

Friedrich, Leon S., Adrian J. McDonald, Gregory E. Bodeker, Kathy E. Cooper, Jared Lewis, and Alexander J. Paterson (Jan. 2017). "A comparison of Loon balloon observations and stratospheric reanalysis products". In: *Atmos. Chem. Phys.* 17.2, pp. 855–866. DOI: 10.5194/acp-17-855-2017.

Frieler, Katja, Peter U. Clark, Feng He, Christo Buizert, Ronja Reese, Stefan R. M. Ligtenberg, Michiel R. van den Broeke, Ricarda Winkelmann, and Anders Levermann (Apr. 2015). "Consistent evidence of increasing Antarctic accumulation with warming". In: *Nat. Clim. Chang.* 5.4, pp. 348–352. DOI: 10.1038/nclimate2574.

Gallaher, David W., G. Garrett Campbell, and Walter N. Meier (2014). "Anomalous variability in Antarctic sea ice extents during the 1960s with the use of Nimbus data". In: *IEEE J. Sel. Top. Appl. Earth Obs. Remote Sens.* 7.3, pp. 1116–1122. DOI: 10.1109/JSTARS.2013.2264391.

Genthon, C., D. Six, C. Scarchilli, V. Ciardini, and M. Frezzotti (Jan. 2016). "Meteorological and snow accumulation gradients across Dome C, East Antarctic plateau". In: *Int. J. Climatol.* 36.1, pp. 455–466. DOI: 10.1002/joc.4362.

Giles, Katharine A., Seymour W. Laxon, and Anthony P. Worby (Feb. 2008). "Antarctic sea ice elevation from satellite radar altimetry". In: *Geophys. Res. Lett.* 35.3, p. L03503. DOI: 10.1029/2007GL031572.

Gong, Daoyi and Shaowu Wang (Feb. 1999). "Definition of Antarctic Oscillation index". In: *Geophys. Res. Lett.* 26.4, pp. 459–462. DOI: 10.1029/1999GL900003.

Goosse, Hugues, Wouter Lefebvre, Anne de Montety, Elisabeth Crespin, and Alejandro H. Orsi (Dec. 2009). "Consistent past half-century trends in the atmosphere, the sea ice and the ocean at high southern latitudes". In: *Clim. Dyn.* 33.7-8, pp. 999–1016. DOI: 10.1007/s00382-008-0500-9.

Goosse, Hugues and V. Zunz (Mar. 2014). "Decadal trends in the Antarctic sea ice extent ultimately controlled by ice–ocean feedback". In: *Cryosphere* 8.2, pp. 453–470. DOI: 10.5194/tc-8-453-2014.

Gorodetskaya, I. V., N. P. M. Van Lipzig, M. R. Van den Broeke, A. Mangold, W. Boot, and C. H. Reijmer (Feb. 2013). "Meteorological regimes and accumulation patterns at Utsteinen, Dronning Maud Land, East Antarctica: Analysis of two

contrasting years". In: *J. Geophys. Res. Atmos.* 118.4, pp. 1700–1715. DOI: 10.1002/jgrd.50177.

Guo, Zhichang, David H. Bromwich, and John J. Cassano (Feb. 2003). "Evaluation of Polar MM5 Simulations of Antarctic Atmospheric Circulation*". In: *Mon. Weather Rev.* 131.2, pp. 384–411. DOI: 10.1175/1520-0493(2003)131<0384:EOPMSO>2.0.CO;2.

Haas, Christian, Marcel Nicolaus, Sascha Willmes, Anthony Worby, and David Flinspach (2008). "Sea ice and snow thickness and physical properties of an ice floe in the western Weddell Sea and their changes during spring warming". In: *Deep. Res. Part II Top. Stud. Oceanogr.* 55.8-9, pp. 963–974. DOI: 10.1016/j.dsr2.2007.12.020.

Hafner, W.D., N.N. Solorzano, and D.A. Jaffe (May 2007). "Analysis of rainfall and fine aerosol data using clustered trajectory analysis for National Park sites in the Western US". In: *Atmos. Environ.* 41.14, pp. 3071–3081. DOI: 10.1016/j.atmosenv.2006.11.049.

Haumann, F. Alexander, Dirk Notz, and Hauke Schmidt (Dec. 2014). "Anthropogenic influence on recent circulation-driven Antarctic sea ice changes". In: *Geophys. Res. Lett.* 41.23, pp. 8429–8437. DOI: 10.1002/2014GL061659.

Heap, John A. and Arthur S. Rundle (Mar. 1971). "Snow Accumulation on the Ross Ice Shelf, Antarctica". In: ed. by Malcolm Mellor, pp. 119–125. DOI: 10.1029/AR002p0119.

Heil, P, C.W. Fowler, and S.E. Lake (Nov. 2006). "Antarctic sea-ice velocity as derived from SSM/I imagery". In: *Ann. Glaciol.* 44.1, pp. 361–366. DOI: 10.3189/172756406781811682.

Heinemann, Günther (Mar. 1990). "Mesoscale Vortices in the Weddell Sea Region (Antarctica)". In: *Mon. Weather Rev.* 118.3, pp. 779–793. DOI: 10.1175/1520-0493(1990)118<0779:MVITWS>2.0.CO;2.

Hobbs, William R., Robert A. Massom, Sharon E. Stammerjohn, Phillip Reid, Guy Williams, and Walter N. Meier (2016). "A review of recent changes in Southern Ocean sea ice, their drivers and forcings". In: *Glob. Planet. Change* 143, pp. 228–250. DOI: 10.1016/j.gloplacha.2016.06.008.

Hobbs, William R. and Marilyn N. Raphael (Oct. 2010). "The Pacific zonal asymmetry and its influence on Southern Hemisphere sea ice variability". In: *Antarct. Sci.* 22.05, pp. 559–571. DOI: 10.1017/S0954102010000283.

Hole, Lars R., Alexis Pérez Bello, Tjarda J. Roberts, Paul B. Voss, and Timo Vihma (Oct. 2016). "Measurements by controlled meteorological balloons in coastal areas of Antarctica". In: *Antarct. Sci.* 28.05, pp. 387–394. DOI: 10.1017/S0954102016000213.

Holland, Paul R. (2014). "Geophysical Research Letters". In: *Geophys. Res. Lett.* May, pp. 1–8. DOI: 10.1002/2014GL060172.Received.

Holland, Paul R. and Ronald Kwok (2012). "Wind-driven trends in Antarctic sea-ice drift". In: *Nat. Geosci.* 5.12, pp. 1–8. DOI: 10.1038/ngeo1627.

Holmes, C.R., P.R. Holland, and T.J. Bracegirdle (Apr. 2019). "Compensating Biases and a Noteworthy Success in the CMIP5 Representation of Antarctic Sea Ice Processes". In: *Geophys. Res. Lett.* 2018GL081796. DOI: 10.1029/2018GL081796.

Hosking, J. Scott, Andrew Orr, Gareth J. Marshall, John Turner, and Tony Phillips (Sept. 2013). "The Influence of the Amundsen–Bellingshausen Seas Low on the Climate of West Antarctica and Its Representation in Coupled Climate Model Simulations". In: *J. Clim.* 26.17, pp. 6633–6648. DOI: 10.1175/JCLI-D-12-00813.1.

Hoskins, Brian John and Kevin Ivan Hodges (2005). "A New Perspective on Southern Hemisphere Storm Tracks". In: *J. Clim.* 18.20, pp. 4108–4129. DOI: 10.1175/JCLI3570.1.

Ionita, Monica, Patrick Scholz, Klaus Grosfeld, and Renate Treffeisen (July 2018). "Moisture transport and Antarctic sea ice: austral spring 2016 event". In: *Earth Syst. Dyn.* 9.3, pp. 939–954. DOI: 10.5194/esd-9-939-2018.

Ivanova, Natalia, Ola M. Johannessen, Leif Toudal Pedersen, and Rasmus T. Tonboe (Nov. 2014). "Retrieval of Arctic Sea Ice Parameters by Satellite Passive Microwave Sensors: A Comparison of Eleven Sea Ice Concentration Algorithms". In: *IEEE Trans. Geosci. Remote Sens.* 52.11, pp. 7233–7246. DOI: 10.1109/TGRS.2014.2310136.

Ivanova, Natalia, L. T. Pedersen, R. T. Tonboe, S. Kern, G. Heygster, T. Lavergne, A. Sørensen, R. Saldo, G. Dybkjær, L. Brucker, and M. Shokr (Sept. 2015). "Inter-comparison and evaluation of sea ice algorithms: towards further identification of challenges and optimal approach using passive microwave observations". In: *Cryosphere* 9.5, pp. 1797–1817. DOI: 10.5194/tc-9-1797-2015.

James, Ian N. (Sept. 1989). "The Antarctic drainage flow: implications for hemispheric flow on the Southern Hemisphere". In: *Antarct. Sci.* 1.3, pp. 279–290. DOI: 10.1017/S0954102089000404.

Jolly, Ben, Adrian J McDonald, Jack H. J. Coggins, John J. Cassano, Matthew A. Lazzara, Peyman Zawar-Reza, Geoffrey Graham, Graeme Plank, Orlon Peterson, and Ethan Dale (2016). "A validation of the Antarctic Mesoscale Prediction System using Self-Organizing Maps and high density observations from SNOWWEB". In: *Mon. Weather Rev.* DOI: 10.1175/MWR-D-15-0447.1.

Jolly, Ben, Andreas Willig, Adrian McDonald, Matthew Pannell, and Graeme Plank (Oct. 2013). "SNOWWEB - Wirelessly connected weather stations in Antarctica". In: *38th Annu. IEEE Conf. Local Comput. Networks - Work.* IEEE, pp. 194–202. DOI: 10.1109/LCNW.2013.6758519.

Jones, Julie M, Sarah T Gille, Hugues Goosse, Nerilie J Abram, Pablo O Canziani, Dan J Charman, Kyle R Clem, Xavier Crosta, Casimir de Lavergne, Ian Eisenman, Matthew H England, Ryan L Fogt, Leela M Frankcombe, Gareth J Marshall, Valérie Masson-Delmotte, Adele K Morrison, Anaïs J Orsi, Marilyn N. Raphael, James A Renwick, David P Schneider, Graham R Simpkins, Eric J Steig, Barbara Stenni, Didier Swingedouw, and Tessa R Vance (Oct. 2016). "Assessing recent trends in high-latitude Southern Hemisphere surface climate". In: *Nat. Clim. Chang.* 6.10, pp. 917–926. DOI: 10.1038/nclimate3103.

Jouzel, J. (2003). "Magnitude of isotope/temperature scaling for interpretation of central Antarctic ice cores". In: *J. Geophys. Res.* 108.D12, p. 4361. DOI: 10.1029/2002JD002677.

Kidson, John W. (Sept. 1999). "Principal Modes of Southern Hemisphere Low-Frequency Variability Obtained from NCEP–NCAR Reanalyses". In: *J. Clim.* 12.9, pp. 2808–2830. DOI: 10.1175/1520-0442(1999)012<2808:PMOSHL>2.0.CO;2.

Kohout, A. L., M. J. M. Williams, S. M. Dean, and M. H. Meylan (May 2014). "Storm-induced sea-ice breakup and the implications for ice extent". In: *Nature* 509.7502, pp. 604–607. DOI: 10.1038/nature13262.

Kostov, Yavor, John Marshall, Ute Hausmann, Kyle C. Armour, David Ferreira, and Marika M Holland (Mar. 2017). "Fast and slow responses of Southern Ocean sea surface temperature to SAM in coupled climate models". In: *Clim. Dyn.* 48.5-6, pp. 1595–1609. DOI: 10.1007/s00382-016-3162-z.

Kreutz, K. J., P. A. Mayewski, I. I. Pittalwala, L. D. Meeker, M. S. Twickler, and S. I. Whitlow (Feb. 2000). "Sea level pressure variability in the Amundsen Sea region inferred from a West Antarctic glaciochemical record". In: *J. Geophys. Res. Atmos.* 105.D3, pp. 4047–4059. DOI: 10.1029/1999JD901069.

Kuipers Munneke, Peter, Stefan R.M. Ligtenberg, Michiel R. Van Den Broeke, and David G. Vaughan (July 2014). "Firn air depletion as a precursor of Antarctic ice-shelf collapse". In: *J. Glaciol.* 60.220, pp. 205–214. DOI: 10.3189/2014JoG13J183.

Kurtz, Dennis D. and David H. Bromwich (Nov. 1983). "Satellite observed behavior of the Terra Nova Bay Polynya". In: *J. Geophys. Res. Ocean.* 88.C14, pp. 9717–9722. DOI: 10.1029/JC088iC14p09717.

Kurtz, Nathan T. and Thorsten Markus (Aug. 2012). "Satellite observations of Antarctic sea ice thickness and volume". In: *J. Geophys. Res. Ocean.* 117.C8, n/a–n/a. DOI: 10.1029/2012JC008141.

Kusahara, Kazuya, Phillip Reid, Guy D Williams, Robert Massom, and Hiroyasu Hasumi (Aug. 2018). "An ocean-sea ice model study of the unprecedented Antarctic sea ice minimum in 2016". In: *Environ. Res. Lett.* 13.8, p. 084020. DOI: 10.1088/1748-9326/aad624.

Kwok, Ronald (2002). "Sea ice concentration estimates from satellite passive microwave radiometry and openings from SAR ice motion". In: *Geophys. Res. Lett.* 29.9, pp. 8–11. DOI: 10.1029/2002GL014787.

– (2010). "Satellite remote sensing of sea-ice thickness and kinematics: A review". In: *J. Glaciol.* 56.200, pp. 1129–1140. DOI: 10.3189/002214311796406167.

Kwok, Ronald, Josefino C. Comiso, Tong Lee, and Paul R. Holland (2016). "Linked trends in the South Pacific sea ice edge and Southern Oscillation Index". In: *Geophys. Res. Lett.* 43.19, pp. 10, 295–10, 302. DOI: 10.1002/2016GL070655.

Kwok, Ronald, Josefino C. Comiso, S. Martin, and R. Drucker (Dec. 2007). "Ross Sea polynyas: Response of ice concentration retrievals to large areas of thin ice". In: *J. Geophys. Res.* 112.C12, p. C12012. DOI: 10.1029/2006JC003967.

Lazzara, Matthew A., George a. Weidner, Linda M. Keller, Jonathan E. Thom, and John J. Cassano (Oct. 2012). "Antarctic Automatic Weather Station Program: 30 Years of Polar Observation". In: *Bull. Am. Meteorol. Soc.* 93.10, pp. 1519–1537. DOI: 10.1175/BAMS-D-11-00015.1.

Lee, Sukyoung (Jan. 2014). "A theory for polar amplification from a general circulation perspective". In: *Asia-Pacific J. Atmos. Sci.* 50.1, pp. 31–43. DOI: 10.1007/s13143-014-0024-7.

Liggett, Daniela, Bryan Storey, and Yvonne Cook (2015). "Exploring the Last Continent". In: *Explor. Last Cont.* Cham: Springer International Publishing. Chap. 15, pp. 1–6. DOI: 10.1007/978-3-319-18947-5_1.

Liu, H., K. Jezek, B. Li, and Z. Zhao. (2001). "Radarsat Antarctic Mapping Project Digital Elevation Model, Version 2." In: *Boulder, Color. USA. NASA Natl. Snow Ice Data Cent. Distrib. Act. Arch. Center.*

Lynch, Amanda H and John J. Cassano (2006). *Applied atmospheric dynamics*. John Wiley & Sons.

Maksym, Ted and Thorsten Markus (Feb. 2008). "Antarctic sea ice thickness and snow-to-ice conversion from atmospheric reanalysis and passive microwave snow depth". In: *J. Geophys. Res.* 113.C2, C02S12. DOI: 10.1029/2006JC004085.

Maksym, Ted, Sharon E. Stammerjohn, Stephen Ackley, and Robert A. Massom (2012). *Antarctic Sea Ice—A Polar Opposite?* DOI: 10.5670/oceanog.2012.88.

Markle, B. R., N. A N Bertler, Kate E. Sinclair, and S. B. Sneed (Jan. 2012). "Synoptic variability in the Ross Sea region, Antarctica, as seen from back-trajectory modeling and ice core analysis". In: *J. Geophys. Res. Atmos.* 117.D2, n/a–n/a. DOI: 10.1029/2011JD016437.

Marshall, Gareth J. (Dec. 2003). "Trends in the Southern Annular Mode from Observations and Reanalyses". In: *J. Clim.* 16.24, pp. 4134–4143. DOI: 10.1175/1520-0442(2003)016<4134:TITSAM>2.0.CO;2.

Marshall, Gareth J and John C King (July 1998). "Southern hemisphere circulation anomalies associated with extreme Antarctic peninsula winter temperatures". In: *Geophys. Res. Lett.* 25.13, pp. 2437–2440. DOI: 10.1029/98GL01651.

Marshall, J and A Plumb (2007). *Atmosphere, Ocean and Climate Dynamics, Volume 93: An Introductory Text (International Geophysics)*. Elsevier Academic Press, pp. 1–345.

Marshall, John and Kevin Speer (Mar. 2012). "Closure of the meridional overturning circulation through Southern Ocean upwelling". In: *Nat. Geosci.* 5.3, pp. 171–180. DOI: 10.1038/ngeo1391.

Mårtensson, S., H. E M Meier, P. Pemberton, and J. Haapala (Aug. 2012). "Ridged sea ice characteristics in the Arctic from a coupled multicategory sea ice model". In: *J. Geophys. Res. Ocean.* 117.C8, n/a–n/a. DOI: 10.1029/2010JC006936.

Martín-Español, Alba, Andrew Zammit-Mangion, Peter J. Clarke, Thomas Flament, Veit Helm, Matt A. King, Scott B. Luthcke, Elizabeth Petrie, Frederique Rémy, Nana Schön, Bert Wouters, and Jonathan L. Bamber (Feb. 2016). "Spatial and temporal Antarctic Ice Sheet mass trends, glacio-isostatic adjustment, and surface processes from a joint inversion of satellite altimeter, gravity, and GPS data". In: *J. Geophys. Res. Earth Surf.* 121.2, pp. 182–200. DOI: 10.1002/2015JF003550.

Martinson, Douglas G. (1990). "Evolution of the southern ocean winter mixed layer and sea ice: Open ocean deepwater formation and ventilation". In: *J. Geophys. Res.* 95.C7, p. 11641. DOI: 10.1029/JC095iC07p11641.

Maslanik, J and Julienne Stroeve (2004). *DMSP SSM/I-SSMIS Daily Polar Gridded Brightness Temperatures, Version 4.* Boulder, Colorado USA. NASA National Snow and Ice Data Center Distributed Active Archive Center. Boulder, Colorado USA. DOI: http://dx.doi.org/10.5067/AN9AI8EO7PX0.

Massom, Robert A. and Sharon E. Stammerjohn (2010). "Antarctic sea ice change and variability - Physical and ecological implications". In: *Polar Sci.* 4.2, pp. 149–186. DOI: 10.1016/j.polar.2010.05.001.

Maykut, Gary A. and Norbert Untersteiner (Feb. 1971). "Some results from a time-dependent thermodynamic model of sea ice". In: *J. Geophys. Res.* 76.6, pp. 1550–1575. DOI: 10.1029/JC076i006p01550.

McDonald, A. J. and M. Smith (Nov. 2013). "A technique to identify vortex air using carbon monoxide observations". In: *J. Geophys. Res. Atmos.* 118.22, pp. 12, 719–12, 733. DOI: 10.1002/2012JD019257.

Medley, B. and E. R. Thomas (Jan. 2019). "Increased snowfall over the Antarctic Ice Sheet mitigated twentieth-century sea-level rise". In: *Nat. Clim. Chang.* 9.1, pp. 34–39. DOI: 10.1038/s41558-018-0356-x.

Meehl, Gerald A., Julie M. Arblaster, Christine T. Y. Chung, Marika M. Holland, Alice DuVivier, LuAnne Thompson, Dongxia Yang, and Cecilia M. Bitz (Dec. 2019). "Sustained ocean changes contributed to sudden Antarctic sea ice retreat in late 2016". In: *Nat. Commun.* 10.1, p. 14. DOI: 10.1038/s41467-018-07865-9.

Meier, Walter N. (2005). "Comparison of passive microwave ice concentration algorithm retrievals with AVHRR imagery in arctic peripheral seas". In: *IEEE Trans. Geosci. Remote Sens.* 43.6, pp. 1324–1337. DOI: 10.1109/TGRS.2005.846151.

Meier, Walter N., F. Fetterer, M. Savoie, S. Mallory, R. Duerr, and J. Stroeve. (2017). *NOAA/NSIDC Climate Data Record of Passive Microwave Sea Ice Concentration, Version 3*. DOI: 10.7265/N59P2ZTG.

Meier, Walter N., F Fetterer, M Savoie, S Mallory, R Duerr, and Julienne Stroeve (2013a). "NOAA/NSIDC climate data record of passive microwave sea ice concentration, version 2". In: *National Snow and Ice Data Center, Boulder, CO.[Available online at http://nsidc. org/data/docs/noaa/g02202_ice_conc_cdr/.]*

Meier, Walter N., D. Gallaher, and G. G. Campbell (Apr. 2013b). "New estimates of Arctic and Antarctic sea ice extent during September 1964 from recovered Nimbus I satellite imagery". In: *Cryosphere* 7.2, pp. 699–705. DOI: 10.5194/tc-7-699-2013.

Meier, Walter N., Siri Jodha, Singh Khalsa, Senior Member, and Matthew H Savoie (2011). "Intersensor Calibration Between F-13 SSM/I and F-17 SSMIS Near-Real-Time Sea Ice Estimates". In: *IEEE Trans. Geosci. Remote Sens.* 49.9, pp. 1–7. DOI: 10.1109/TGRS.2011.2117433.

Meier, Walter N., Ge Peng, Donna J. Scott, and Matt H. Savoie (2014). "Verification of a new NOAA/NSIDC passive microwave sea-ice concentration climate record". In: *Polar Res.* 33.2014. DOI: 10.3402/polar.v33.21004.

Nakata, Kazuki, Kay I. Ohshima, Sohey Nihashi, Noriaki Kimura, and Takeshi Tamura (Sept. 2015). "Variability and ice production budget in the Ross Ice Shelf Polynya based on a simplified polynya model and satellite observations". In: *J. Geophys. Res. Ocean.* 120.9, pp. 6234–6252. DOI: 10.1002/2015JC010894.

Neff, Peter D and Nancy A N Bertler (Sept. 2015). "Trajectory modeling of modern dust transport to the Southern Ocean and Antarctica". In: *J. Geophys. Res. Atmos.* 120.18, pp. 9303–9322. DOI: 10.1002/2015JD023304.

Nicolas, Julien P. and David H. Bromwich (Jan. 2011a). "Climate of West Antarctica and Influence of Marine Air Intrusions*". In: *J. Clim.* 24.1, pp. 49–67. DOI: 10.1175/2010JCLI3522.1.

– (2011b). "Precipitation Changes in High Southern Latitudes from Global Reanalyses: A Cautionary Tale". In: *Surv. Geophys.* 32.4-5, pp. 475–494. DOI: 10.1007/s10712-011-9114-6.

– (2014). "New Reconstruction of Antarctic Near-Surface Temperatures: Multidecadal Trends and Reliability of Global Reanalyses". In: *Journal of Climate* 27.21, pp. 8070–8093. DOI: 10.1175/JCLI-D-13-00733.1. eprint: https://doi.org/10.1175/JCLI-D-13-00733.1.

Nigro, Melissa A. and John J. Cassano (2014a). "Analysis of the Ross Ice Shelf Airstream Forcing Mechanisms Using Self-Organizing Maps". In: *Mon. Weather Rev.* 142.12, pp. 4719–4734. DOI: 10.1175/mwr-d-14-00077.1.

– (July 2014b). "Identification of Surface Wind Patterns over the Ross Ice Shelf, Antarctica, Using Self-Organizing Maps". In: *Mon. Weather Rev.* 142.7, pp. 2361–2378. DOI: 10.1175/MWR-D-13-00382.1.

Nigro, Melissa A., John J. Cassano, and Shelley L. Knuth (Apr. 2012a). "Evaluation of Antarctic Mesoscale Prediction System (AMPS) cyclone forecasts using infrared satellite imagery". In: *Antarct. Sci.* 24.02, pp. 183–192. DOI: 10.1017/S0954102011000745.

Nigro, Melissa A., John J. Cassano, Matthew A. Lazzara, and Linda M. Keller (July 2012b). "Case Study of a Barrier Wind Corner Jet off the Coast of the Prince Olav Mountains, Antarctica". In: *Mon. Weather Rev.* 140.7, pp. 2044–2063. DOI: 10.1175/MWR-D-11-00261.1.

Nigro, Melissa A., John J. Cassano, and Mark W. Seefeldt (Apr. 2011). "A Weather-Pattern-Based Approach to Evaluate the Antarctic Mesoscale Prediction System (AMPS) Forecasts: Comparison to Automatic Weather Station Observations". In: *Weather Forecast.* 26.2, pp. 184–198. DOI: 10.1175/2010WAF2222444.1.

Ohshima, Kay I., Yasushi Fukamachi, Guy D. Williams, Sohey Nihashi, Fabien Roquet, Yujiro Kitade, Takeshi Tamura, Daisuke Hirano, Laura Herraiz-Borreguero, Iain Field, Mark Hindell, Shigeru Aoki, and Masaaki Wakatsuchi

(2013). "Antarctic Bottom Water production by intense sea-ice formation in the Cape Darnley polynya". In: *Nat. Geosci.* 6.3, pp. 235–240. DOI: 10.1038/ngeo1738.

Papritz, Lukas and Stephan Pfahl (Jan. 2016). "Importance of Latent Heating in Mesocyclones for the Decay of Cold Air Outbreaks: A Numerical Process Study from the Pacific Sector of the Southern Ocean". In: *Mon. Weather Rev.* 144.1, pp. 315–336. DOI: 10.1175/MWR-D-15-0268.1.

Papritz, Lukas, Stephan Pfahl, Harald Sodemann, and Heini Wernli (Jan. 2015). "A Climatology of Cold Air Outbreaks and Their Impact on Air–Sea Heat Fluxes in the High-Latitude South Pacific". In: *J. Clim.* 28.1, pp. 342–364. DOI: 10.1175/JCLI-D-14-00482.1.

Parish, Thomas R. (Feb. 1982). "Surface Airflow Over East Antarctica". In: *Mon. Weather Rev.* 110.2, pp. 84–90. DOI: 10.1175/1520-0493(1982)110<0084:SAOEA>2.0.CO;2.

– (Aug. 1992). "On the Role of Antarctic Katabatic Winds in Forcing Large-Scale Tropospheric Motions". In: *J. Atmos. Sci.* 49.15, pp. 1374–1385. DOI: 10.1175/1520-0469(1992)049<1374:OTROAK>2.0.CO;2.

Parish, Thomas R. and David H. Bromwich (July 1987). "The surface windfield over the Antarctic ice sheets". In: *Nature* 328.6125, pp. 51–54. DOI: 10.1038/328051a0.

– (Feb. 1991). "Continental-Scale Simulation of the Antarctic Katabatic Wind Regime". In: *J. Clim.* 4.2, pp. 135–146. DOI: 10.1175/1520-0442(1991)004<0135:CSSOTA>2.0.CO;2.

– (June 1997). "On the forcing of seasonal changes in surface pressure over Antarctica". In: *J. Geophys. Res. Atmos.* 102.D12, pp. 13785–13792. DOI: 10.1029/96JD02959.

– (Jan. 1998). "A Case Study of Antarctic Katabatic Wind Interaction with Large-Scale Forcing*". In: *Mon. Weather Rev.* 126.1, pp. 199–209. DOI: 10.1175/1520-0493(1998)126<0199:ACSOAK>2.0.CO;2.

– (2007). "Reexamination of the Near-Surface Airflow over the Antarctic Continent and Implications on Atmospheric Circulations at High Southern Latitudes*". In: *Mon. Weather Rev.* 135.5, pp. 1961–1973. DOI: 10.1175/MWR3374.1.

Parish, Thomas R., David H. Bromwich, and Ren-Yow Tzeng (Dec. 1994). "On the Role of the Antarctic Continent in Forcing Large-Scale Circulations in the High Southern Latitudes". In: *J. Atmos. Sci.* 51.24, pp. 3566–3579. DOI: 10.1175/1520-0469(1994)051<3566:OTROTA>2.0.CO;2.

Parish, Thomas R. and John J. Cassano (Feb. 2003). "The Role of Katabatic Winds on the Antarctic Surface Wind Regime". In: *Mon. Weather Rev.* 131.2, pp. 317–333. DOI: 10.1175/1520-0493(2003)131<0317:TROKWO>2.0.CO;2.

Parish, Thomas R., John J. Cassano, and Mark W. Seefeldt (2006). "Characteristics of the Ross Ice Shelf air stream as depicted in Antarctic Mesoscale Prediction System simulations". In: *J. Geophys. Res.* 111.D12, p. D12109. DOI: 10.1029/2005JD006185.

Parish, Thomas R. and Kenneth T. Waight (Oct. 1987). "The Forcing of Antarctic Katabatic Winds". In: *Mon. Weather Rev.* 115.10, pp. 2214–2226. DOI: 10.1175/1520-0493(1987)115<2214:TFOAKW>2.0.CO;2.

Parkinson, Claire L. and Donald J. Cavalieri (2012). "Antarctic sea ice variability and trends, 1979-2010". In: *Cryosphere* 6.4, pp. 871–880. DOI: 10.5194/tc-6-871-2012.

Parkinson, Claire L. and Josefino C. Comiso (2013). "On the 2012 record low Arctic sea ice cover: Combined impact of preconditioning and an August storm". In: *Geophys. Res. Lett.* 40.7, pp. 1356–1361. DOI: 10.1002/grl.50349.

Parkinson, Claire L. and Nicolo E. DiGirolamo (2016). "New visualizations highlight new information on the contrasting Arctic and Antarctic sea-ice trends since the late 1970s". In: *Remote Sens. Environ.* 183, pp. 198–204. DOI: 10.1016/j.rse.2016.05.020.

Pauling, Andrew G., Cecilia M. Bitz, Inga J. Smith, and Patricia J. Langhorne (Mar. 2016). "The Response of the Southern Ocean and Antarctic Sea Ice to Freshwater from Ice Shelves in an Earth System Model". In: *J. Clim.* 29.5, pp. 1655–1672. DOI: 10.1175/JCLI-D-15-0501.1.

Pauling, Andrew G., Inga J. Smith, Patricia J. Langhorne, and Cecilia M. Bitz (Oct. 2017). "Time-Dependent Freshwater Input From Ice Shelves: Impacts on Antarctic Sea Ice and the Southern Ocean in an Earth System Model". In: *Geophys. Res. Lett.* 44.20, pp. 10, 454–10, 461. DOI: 10.1002/2017GL075017.

Peng, G., Walter N. Meier, D. J. Scott, and M. H. Savoie (2013). "A long-term and reproducible passive microwave sea ice concentration data record for climate studies and monitoring". In: *Earth Syst. Sci. Data* 5.2, pp. 311–318. DOI: 10.5194/essd-5-311-2013.

Pezzi, Luciano Ponzi, Ronald Buss de Souza, and Mário F.L. Quadro (Sept. 2016). "Uma Revisão dos Processos de Interação Oceano-Atmosfera em Regiões de Intenso Gradiente Termal do Oceano Atlântico Sul Baseada em Dados Observacionais". In: *Rev. Bras. Meteorol.* 31.4, pp. 428–453. DOI: 10.1590/0102-778631231420150032.

Polvani, Lorenzo M., Darryn W. Waugh, Gustavo J. P. Correa, and Seok-Woo Son (Feb. 2011). "Stratospheric Ozone Depletion: The Main Driver of Twentieth-Century Atmospheric Circulation Changes in the Southern Hemisphere". In: *J. Clim.* 24.3, pp. 795–812. DOI: 10.1175/2010JCLI3772.1.

Pope, A., P. Wagner, R. Johnson, J.D. Shutler, J. Baeseman, and L. Newman (Apr. 2017). "Community review of Southern Ocean satellite data needs". In: *Antarct. Sci.* 29.02, pp. 97–138. DOI: 10.1017/S0954102016000390.

Powers, Jordan G. (Sept. 2007). "Numerical Prediction of an Antarctic Severe Wind Event with the Weather Research and Forecasting (WRF) Model". In: *Mon. Weather Rev.* 135.9, pp. 3134–3157. DOI: 10.1175/MWR3459.1.

Powers, Jordan G, Kevin W Manning, David H. Bromwich, John J. Cassano, and Arthur M Cayette (Nov. 2012). "A Decade of Antarctic Science Support Through Amps". In: *Bull. Am. Meteorol. Soc.* 93.11, pp. 1699–1712. DOI: 10.1175/BAMS-D-11-00186.1.

Price, Daniel, Iman Soltanzadeh, Wolfgang Rack, and Ethan R. Dale (May 2019). "Snow driven uncertainty ranges in CryoSat-2 Antarctic sea ice thickness; insights from McMurdo Sound". In: *The Cryosphere* May, pp. 1–22. DOI: 10.5194/tc-2018-92.

Purich, Ariaan, Wenju Cai, Matthew H England, and Tim Cowan (Dec. 2016). "Evidence for link between modelled trends in Antarctic sea ice and underestimated westerly wind changes". In: *Nat. Commun.* 7.1, p. 10409. DOI: 10.1038/ncomms10409.

Raphael, Marilyn N. (June 2007). "The influence of atmospheric zonal wave three on Antarctic sea ice variability". In: *J. Geophys. Res.* 112.D12, p. D12112. DOI: 10.1029/2006JD007852.

Raphael, Marilyn N., G. J. Marshall, J. Turner, R. L. Fogt, D. Schneider, D. A. Dixon, J. S. Hosking, J. M. Jones, and William R. Hobbs (Jan. 2016). "The Amundsen Sea Low: Variability, Change, and Impact on Antarctic Climate". In: *Bull. Am. Meteorol. Soc.* 97.1, pp. 111–121. DOI: 10.1175/BAMS-D-14-00018.1.

Reddy, Tasha E., Kevin R. Arrigo, and David M. Holland (July 2007). "The role of thermal and mechanical processes in the formation of the Ross Sea summer polynya". In: *J. Geophys. Res.* 112.C7, p. C07027. DOI: 10.1029/2006JC003874.

Reid, Phil, Sharon E. Stammerjohn, Robert A. Massom, Ted Scambos, and Jan Lieser (2015). "The record 2013 Southern Hemisphere sea-ice extent maximum". In: *Ann. Glaciol.* 56.69, pp. 99–106. DOI: 10.3189/2015AoG69A892.

Roach, Lettie A., Madison M. Smith, and Samuel M. Dean (Apr. 2018). "Quantifying Growth of Pancake Sea Ice Floes Using Images From Drifting Buoys". In: *J. Geophys. Res. Ocean.* 123.4, pp. 2851–2866. DOI: 10.1002/2017JC013693.

Roberts, Tjarda J., Marina Dütsch, Lars R. Hole, and Paul B. Voss (Sept. 2016). "Controlled meteorological (CMET) free balloon profiling of the Arctic atmospheric boundary layer around Spitsbergen compared to ERA-Interim and Arctic System Reanalyses". In: *Atmos. Chem. Phys.* 16.19, pp. 12383–12396. DOI: 10.5194/acp-16-12383-2016.

Rye, Craig D., Alberto C. Naveira Garabato, Paul R. Holland, Michael P. Meredith, A. J. George Nurser, Chris W. Hughes, Andrew C. Coward, and David J. Webb (Oct. 2014). "Rapid sea-level rise along the Antarctic margins in response to increased glacial discharge". In: *Nat. Geosci.* 7.10, pp. 732–735. DOI: 10.1038/ngeo2230.

Scarchilli, Claudio, Massimo Frezzotti, and Paolo Michele Ruti (Nov. 2011). "Snow precipitation at four ice core sites in East Antarctica: provenance, seasonality and blocking factors". In: *Clim. Dyn.* 37.9-10, pp. 2107–2125. DOI: 10.1007/s00382-010-0946-4.

Schlosser, Elisabeth, K. W. Manning, J. G. Powers, M. G. Duda, G. Birnbaum, and K. Fujita (July 2010a). "Characteristics of high-precipitation events in Dronning Maud Land, Antarctica". In: *J. Geophys. Res.* 115.D14, p. D14107. DOI: 10.1029/2009JD013410.

Schlosser, Elisabeth, Hans Oerter, Valerie Masson-Delmotte, and Carleen Reijmer (Sept. 2008). "Atmospheric influence on the deuterium excess signal in polar firn: implications for ice-core interpretation". In: *J. Glaciol.* 54.184, pp. 117–124. DOI: 10.3189/002214308784408991.

Schlosser, Elisabeth, Jordan G. Powers, Michael G. Duda, Kevin W. Manning, Carleen H. Reijmer, and Michiel R. Van Den Broeke (Dec. 2010b). "An extreme precipitation event in Dronning Maud Land, Antarctica: a case study with the Antarctic Mesoscale Prediction System". In: *Polar Res.* 29.3, pp. 330–344. DOI: 10.1111/j.1751-8369.2010.00164.x.

Schlosser, Elisabeth, Barbara Stenni, Mauro Valt, Anselmo Cagnati, G. Powers Jordan, W. Manning Kevin, Marilyn N. Raphael, and G. Duda Michael (2016). "Precipitation and synoptic regime in two extreme years 2009 and 2010 at Dome C, Antarctica-implications for ice core interpretation". In: *Atmos. Chem. Phys.* 16.8, pp. 4757–4770. DOI: 10.5194/acp-16-4757-2016.

Schwerdtfeger, W. (1984). *Weather and climate of the antarctic*. Elsevier, Amsterdam.

Seefeldt, Mark W. and John J. Cassano (May 2012). "A description of the Ross Ice Shelf air stream (RAS) through the use of self-organizing maps (SOMs)". In: *J. Geophys. Res. Atmos.* 117.D9, n/a–n/a. DOI: 10.1029/2011JD016857.

Seefeldt, Mark W., Gregory J. Tripoli, and Charles R. Stearns (Feb. 2003). "A High-Resolution Numerical Simulation of the Wind Flow in the Ross Island Region,

Antarctica". In: *Mon. Weather Rev.* 131.2, pp. 435–458. DOI: 10.1175/1520-0493(2003)131<0435:AHRNSO>2.0.CO;2.

Sen Gupta, Alexander and Matthew H. England (Sept. 2006). "Coupled Ocean–Atmosphere–Ice Response to Variations in the Southern Annular Mode". In: *J. Clim.* 19.18, pp. 4457–4486. DOI: 10.1175/JCLI3843.1.

Serreze, Mark C. and Julienne Stroeve (2015). "Arctic sea ice trends, variability and implications for seasonal ice forecasting". In: *Philos. Trans. R. Soc. A Math. Phys. Eng. Sci.* 373.2045, p. 20140159. DOI: 10.1098/rsta.2014.0159.

Shen, Hayley H. (2004). "Limiting diameter of pancake ice". In: *J. Geophys. Res.* 109.C12, p. C12035. DOI: 10.1029/2003JC002123.

Shen, Hayley H., Stephen F. Ackley, and Mark A. Hopkins (Sept. 2001). "A conceptual model for pancake-ice formation in a wave field". In: *Ann. Glaciol.* 33.3, pp. 361–367. DOI: 10.3189/172756401781818239.

Sigmond, M. and J. C. Fyfe (Sept. 2010). "Has the ozone hole contributed to increased Antarctic sea ice extent?" In: *Geophys. Res. Lett.* 37.18, n/a–n/a. DOI: 10.1029/2010GL044301.

Simmonds, Ian (2015). "Comparing and contrasting the behaviour of Arctic and Antarctic sea ice over the 35 year period 1979-2013". In: *Ann. Glaciol.* 56.69, pp. 18–28. DOI: 10.3189/2015AoG69A909.

Simmonds, Ian, Kevin Keay, and Eun-Pa Lim (Feb. 2003). "Synoptic Activity in the Seas around Antarctica". In: *Mon. Weather Rev.* 131.2, pp. 272–288. DOI: 10.1175/1520-0493(2003)131<0272:SAITSA>2.0.CO;2.

Sinclair, Kate E., N. A N Bertler, and W. J. Trompetter (Nov. 2010). "Synoptic controls on precipitation pathways and snow delivery to high-accumulation ice core sites in the Ross Sea region, Antarctica". In: *J. Geophys. Res.* 115.D22, p. D22112. DOI: 10.1029/2010JD014383.

Sinclair, Kate E., Nancy A N Bertler, W. J. Trompetter, and W. T. Baisden (Mar. 2013). "Seasonality of Airmass Pathways to Coastal Antarctica: Ramifications for Interpreting High-Resolution Ice Core Records". In: *J. Clim.* 26.6, pp. 2065–2076. DOI: 10.1175/JCLI-D-12-00167.1.

Smith, Madeleine L and Adrian J. McDonald (May 2014). "A quantitative measure of polar vortex strength using the function M". In: *J. Geophys. Res. Atmos.* 119.10, pp. 5966–5985. DOI: 10.1002/2013JD020572.

Sodemann, Harald and Andreas Stohl (Nov. 2009). "Asymmetries in the moisture origin of Antarctic precipitation". In: *Geophys. Res. Lett.* 36.22, p. L22803. DOI: 10.1029/2009GL040242.

Stammerjohn, Sharon E., D. G. Martinson, R. C. Smith, X. Yuan, and D. Rind (Mar. 2008). "Trends in Antarctic annual sea ice retreat and advance and their relation

to El Niño–Southern Oscillation and Southern Annular Mode variability". In: *J. Geophys. Res.* 113.C3, C03S90. DOI: 10.1029/2007JC004269.

Steinhoff, Daniel F., David H. Bromwich, Michelle Lambertson, Shelley L. Knuth, and Matthew A. Lazzara (Jan. 2008). "A Dynamical Investigation of the May 2004 McMurdo Antarctica Severe Wind Event Using AMPS*". In: *Mon. Weather Rev.* 136.1, pp. 7–26. DOI: 10.1175/2007MWR1999.1.

Steinhoff, Daniel F., Saptarshi Chaudhuri, and David H. Bromwich (Nov. 2009). "A Case Study of a Ross Ice Shelf Airstream Event: A New Perspective*". In: *Mon. Weather Rev.* 137.11, pp. 4030–4046. DOI: 10.1175/2009MWR2880.1.

Stenmark, Aurora, Lars Robert Hole, Paul B. Voss, Joachim Reuder, and Marius O. Jonassen (June 2014). "The influence of Nunataks on atmospheric boundary layer convection during summer in Dronning Maud Land, Antarctica". In: *J. Geophys. Res. Atmos.* 119.11, pp. 6537–6548. DOI: 10.1002/2013JD021287.

Stohl, Andreas and Harald Sodemann (Jan. 2010). "Characteristics of atmospheric transport into the Antarctic troposphere". In: *J. Geophys. Res.* 115.D2, p. D02305. DOI: 10.1029/2009JD012536.

Stuecker, Malte F., Cecilia M. Bitz, and Kyle C. Armour (Sept. 2017). "Conditions leading to the unprecedented low Antarctic sea ice extent during the 2016 austral spring season". In: *Geophys. Res. Lett.* 44.17, pp. 9008–9019. DOI: 10.1002/2017GL074691.

Sturm, Matthew and Robert A. Massom (2009). "Snow and sea ice". In: *Sea ice* 2, pp. 153–204.

Swart, N. C. and J. C. Fyfe (Aug. 2013). "The influence of recent Antarctic ice sheet retreat on simulated sea ice area trends". In: *Geophys. Res. Lett.* 40.16, pp. 4328–4332. DOI: 10.1002/grl.50820.

Tamura, Takeshi and Kay I. Ohshima (2008). "Mapping of sea ice production in the Arctic coastal polynyas". In: *J. Geophys. Res. Ocean.* 116.7, pp. 1–5. DOI: 10.1029/2010JC006586.

Thompson, David W. J., John M. Wallace, and Gabriele C. Hegerl (Mar. 2000). "Annular Modes in the Extratropical Circulation. Part II: Trends". In: *J. Clim.* 13.5, pp. 1018–1036. DOI: 10.1175/1520-0442(2000)013<1018:AMITEC>2.0.CO;2.

Turner, John, Thomas J. Bracegirdle, Tony Phillips, Gareth J. Marshall, and J. Scott Hosking (2013a). "An initial assessment of antarctic sea ice extent in the CMIP5 models". In: *J. Clim.* 26.5, pp. 1473–1484. DOI: 10.1175/JCLI-D-12-00068.1.

Turner, John, Steve R. Colwell, Gareth J. Marshall, Tom A. Lachlan-Cope, Andrew M. Carleton, Phil D. Jones, Victor Lagun, Phil A. Reid, and Svetlana Iagovkina (2005). "Antarctic climate change during the last 50 years". In: *International Journal of Climatology* 25.3, pp. 279–294. DOI: 10.1002/joc.1130.

Turner, John and Josefino C. Comiso (July 2017). "Solve Antarctica's sea-ice puzzle". In: *Nature* 547.7663, pp. 275–277. DOI: 10.1038/547275a.

Turner, John, Josefino C. Comiso, Gareth J. Marshall, Tom A. Lachlan Cope, Tom Bracegirdle, Ted Maksym, Michael P. Meredith, Zhaomin Wang, and Andrew Orr (Apr. 2009). "Non annular atmospheric circulation change induced by stratospheric ozone depletion and its role in the recent increase of Antarctic sea ice extent". In: *Geophys. Res. Lett.* 36.8. DOI: 10.1029/2009GL037524.

Turner, John, J Scott Hosking, Thomas J Bracegirdle, Gareth J Marshall, and Tony Phillips (July 2015). "Recent changes in Antarctic Sea Ice". In: *Philos. Trans. R. Soc. A Math. Phys. Eng. Sci.* 373.2045, p. 20140163. DOI: 10.1098/rsta.2014.0163.

Turner, John, J. Scott Hosking, Gareth J. Marshall, Tony Phillips, and Thomas J. Bracegirdle (Apr. 2016). "Antarctic sea ice increase consistent with intrinsic variability of the Amundsen Sea Low". In: *Clim. Dyn.* 46.7-8, pp. 2391–2402. DOI: 10.1007/s00382-015-2708-9.

Turner, John, J. Scott Hosking, Tony Phillips, and Gareth J. Marshall (2013b). "Temporal and spatial evolution of the Antarctic sea ice prior to the September 2012 record maximum extent". In: *Geophys. Res. Lett.* 40.22, pp. 5894–5898. DOI: 10.1002/2013GL058371.

Turner, John, James E. Overland, and John E. Walsh (Mar. 2007). "An Arctic and antarctic perspective on recent climate change". In: *Int. J. Climatol.* 27.3, pp. 277–293. DOI: 10.1002/joc.1406.

Turner, John, Tony Phillips, J Scott Hosking, Gareth J Marshall, and Andrew Orr (June 2013c). "The Amundsen Sea low". In: *Int. J. Climatol.* 33.7, pp. 1818–1829. DOI: 10.1002/joc.3558.

Turner, John, Tony Phillips, Gareth J. Marshall, J. Scott Hosking, James O. Pope, Thomas J. Bracegirdle, and Pranab Deb (2017). "Unprecedented springtime retreat of Antarctic sea ice in 2016". In: *Geophys. Res. Lett.* 44.13, pp. 6868–6875. DOI: 10.1002/2017GL073656.

Turner, John and Jeremy P. Thomas (Oct. 1994). "Summer-season mesoscale cyclones in the bellingshausen-weddell region of the antarctic and links with the synoptic-scale environment". In: *Int. J. Climatol.* 14.8, pp. 871–894. DOI: 10.1002/joc.3370140805.

Vaughan, D.G., Josefino C. Comiso, I. Allison, J. Carrasco, G. Kaser, Ronald Kwok, P. Mote, T. Murray, F. Paul, J. Ren, E. Rignot, O. Solomina, K. Steffen, and T. Zhang (2013). "Observations: Cryosphere". In: *Clim. Chang. 2013 Phys. Sci. Basis Work. Gr. I Contrib. to Fifth Assess. Rep. Intergov. Panel Clim. Chang.* 9781107057, pp. 317–382. DOI: 10.1017/CBO9781107415324.012.

Voss, Paul B., Lars R. Hole, Elizabeth F. Helbling, and Tjarda J. Roberts (Aug. 2012). "Continuous In-Situ Soundings in the Arctic Boundary Layer: A New Atmospheric Measurement Technique Using Controlled Meteorological Balloons". In: *J. Intell. Robot. Syst.* 70.1-4, pp. 609–617. DOI: 10.1007/s10846-012-9758-6.

Walsh, Kevin J.E., Ian Simmonds, and Mark Collier (Dec. 2000). "Sigma-coordinate calculation of topographically forced baroclinicity around Antarctica". In: *Dyn. Atmos. Ocean.* 33.1, pp. 1–29. DOI: 10.1016/S0377-0265(00)00054-3.

Wang, Guomin, Harry H. Hendon, Julie M. Arblaster, Eun-Pa Lim, S. Abhik, and Peter van Rensch (Dec. 2019). "Compounding tropical and stratospheric forcing of the record low Antarctic sea-ice in 2016". In: *Nat. Commun.* 10.1, p. 13. DOI: 10.1038/s41467-018-07689-7.

Wendler, G., B. Moore, B. Hartmann, M. Stuefer, and R. Flint (Mar. 2004). "Effects of multiple reflection and albedo on the net radiation in the pack ice zones of Antarctica". In: *J. Geophys. Res. Atmos.* 109.D6, n/a–n/a. DOI: 10.1029/2003JD003927.

Whitworth, III and A. H. Orsi (2006). "Antarctic Bottom Water production and export by tides in the Ross Sea". In: *Geophys. Res. Lett.* 33.12, pp. 1–4. DOI: 10.1029/2006GL026357.

Zhang, Jinlun (2007). "Increasing antarctic sea ice under warming atmospheric and oceanic conditions". In: *J. Clim.* 20.11, pp. 2515–2529. DOI: 10.1175/JCLI4136.1.

Zhang, Xiangdong and John E Walsh (2006). "Toward a Seasonally Ice-Covered Arctic Ocean: Scenarios from the IPCC AR4 Model Simulations". In: *J. Clim.* 19.9, pp. 1730–1747. DOI: 10.1175/JCLI3767.1.

Zhou, Mingyu, Zhanhai Zhang, Shiyuan Zhong, Donald Lenschow, Hsiao Ming Hsu, Bo Sun, Zhiqiu Gao, Shiming Li, Xindi Bian, and Lejiang Yu (Sept. 2009). "Observations of near-surface wind and temperature structures and their variations with topography and latitude in East Antarctica". In: *J. Geophys. Res. Atmos.* 114.17, p. D17115. DOI: 10.1029/2008JD011611.

Zunz, V., H. Goosse, and F. Massonnet (2013). "How does internal variability influence the ability of CMIP5 models to reproduce the recent trend in Southern

Ocean sea ice extent?" In: *Cryosphere* 7.2, pp. 451–468. DOI: 10.5194/tc-7-451-2013.

Zwally, H. Jay, Josefino C. Comiso, Claire L. Parkinson, William J. Campbell, and Frank D. Carsey (1983). "Antarctic Sea Ice, 1973-1976: Satellite Passive-Microwave Observations". In: 459, p. 212.